SMHYLES

SAFE, SUSTAINABLE AND MODULAR HYBRID SYSTEMS
FOR LONG-DURATION ENERGY STORAGE AND GRID SERVICES

SMHYLES #101138029

Digital twins for HESSs design

Report: D2.2 “Digital twins for HESSs design”

Date: 31.12.2024

Co-funded by the European Union

SMHYLES

DELIVERABLE NAME

Digital Twins for HESS Design

PROJECT GRANT N.

Grant: 101138029

DISSEMINATION LEVEL:

Public (PU)

MAIN AUTHORS:

Marcin Buchajczyk

Saman Korjani

Amir Naebi

Mattia Duranti

Edoardo Gino Macchi

DATE OF SUBMISSION:

30.01.2025

CONTENTS

1. Introduction 3
1.1. Scope of the Deliverable and Objectives 4
1.2. Interaction with Other Work Packages and Tasks 5
1.3. Structure of the Report 5
2. Overview of Hybrid Energy Storage and Digital Twin Technologies 6
2.1. Hybrid Energy Storage Systems Overview 6
2.2. Digital Twins in Energy Systems Overview 7
2.3. Introduction to the Components of HESS 10
2.3.1. Redox Flow Batteries 10
2.3.2. Salt-based Batteries 12
2.3.3. Supercapacitors 15
3. Development of the HESS Model 17
3.1. Overview of the Model Development Process 17
3.2. Model of the Redox Flow Battery 18
3.2.1. Mathematical Model of the Vanadium Redox Flow Battery 18
3.2.2. VRFB Model Results 28
3.3. Model of Salt-based Battery 34
3.3.1. Mathematical Model of the Salt-Based Battery 34
3.3.2. Salt-Based Battery Model Results 42
3.4. Model of Supercapacitor 50
3.4.1. Mathematical Model of the Supercapacitor 50
3.4.2. Supercapacitor Model Results 53
4. Interaction Modeling and Operational Strategy 58
4.1. Defining the Interaction models between RFB/Salt-based Batteries and SC 58
4.2. Implementation of multi-objective Optimization tools 60
4.3. Show case of HESS FOR Self-Consumption Enhancement 63
4.4. Optimization of HESS for Energy arbitrage 73
5. Conclusion and Future Work 82
References 84

1. INTRODUCTION

The global transition towards renewable energy has brought with it a pressing demand for more advanced and adaptable energy storage systems. As the share of renewables, such as wind and solar, increases in the energy mix, the intermittency of these sources introduces challenges in maintaining grid stability and ensuring a continuous supply of power. To address this, the SMHYLES project focuses on the development of Hybrid Energy Storage Systems (HESSs) that combine two distinct and complementary storage technologies: aqueous-based and salt-based systems. These technologies promise to overcome the limitations of conventional energy storage solutions, providing greater flexibility, faster response times, and improved scalability.

Hybrid systems, particularly those that integrate different energy storage technologies, are increasingly seen as key to supporting the dynamic requirements of modern grids [1]. Aqueous and salt-based battery energy storage systems offer long-duration energy storage capacity, which is ideal for balancing energy supply over extended periods, while supercapacitors provide high power density, which is essential for responding to rapid changes in demand [2]. By integrating these technologies, SMHYLES can meet both long-term energy needs and provide fast-acting ancillary services, such as frequency regulation and voltage support, which are critical in scenarios involving high penetration of renewable energy.

A key innovation in the SMHYLES project is to provide the hybrid models of Digital Twin technologies. Digital Twins are virtual replicas of physical systems that allow for real-time monitoring, simulation, and optimization. In the context of HESSs, Digital Twins provide a comprehensive toolset for optimizing the design, monitoring operational efficiency, and extending the lifespan of the storage systems. By simulating various operational scenarios, these digital models enable operators to predict system behaviour under different conditions, such as varying loads, grid disturbances, or equipment degradation. This capability not only improves the performance and reliability of the HESSs but also reduces operational risks and costs [3].

Through the development of these advanced HESS digital models, SMHYLES is poised to make a significant impact on the future of energy storage. The project will contribute to the decarbonization of the energy sector, improve grid reliability, and unlock new business opportunities for energy storage solutions across Europe. In doing so, it not only supports the European Union's climate goals but also addresses the broader challenge of ensuring a secure and sustainable energy future. In this deliverable (D2.2), the focus is the development of digital models that optimize HESS design and operations by simulating long-term system behaviour under varying operational and business conditions. These models can be used as digital replicas for Digital Twins' application. The targets are the creation of models for optimal HESS design, focusing on techno-economic assessments which are essential for evaluating

long-term operational strategies, incorporating components such as energy prices, contracts with grid operators (energy market), loads, and generation data. The models simulate long-term operation periods, accounting for specific use and business cases, and are built using simplified system-level representations of the HESS components (AHESS, SHESS). Such simulations will support the optimal sizing of HESSs and provide input for further sizing studies in Task 2.3.

In addition to optimizing the design process, the digital models will integrate data from components' operational behaviours, such as the flow, salt batteries and supercapacitor interactions, to ensure efficient system-level coordination. This modelling approach enables the project to provide robust solutions for energy storage in diverse environments, such as industrial microgrids and grid-connected systems. Furthermore, the models consider the operational behaviour under varying conditions considering energy tariffs, consumption and RES generations, thereby improving the provision of ancillary services to the grid.

1.1. SCOPE OF THE DELIVERABLE AND OBJECTIVES

The primary scope of D2.2 is to develop digital models at system and component level specifically for Hybrid Energy Storage Systems (HESSs), to optimize their design and operational strategies. These digital models will simulate long-term system behaviour and focus on technical and economic factors influencing system performance. The digital models will integrate key data such as energy prices, contracts with grid operators, load variations, and renewable energy generation to evaluate HESS performance under different scenarios.

The main objectives of this deliverable are:

- **Techno-economic assessment** – The digital models will allow for a detailed techno-economic analysis of the HESS, evaluating the technical aspects like energy storage capacity, efficiency, available power, and state of charge (SOC), as well as economic factors such as operational costs, energy market prices, and grid service revenues.
- **Optimization of HESS design** – The deliverable aims to provide optimal assessment of coordination of the HESS sizing, combining the strengths of aqueous and salt-based storage systems for long-term energy balancing and supercapacitors for rapid response.
- **Simulation of operational scenarios** – The digital models will be used to simulate various operational scenarios defined within Use and Business Cases outlined in D2.1 over long-term periods, providing insights for optimizing energy storage operations in industrial microgrids and grid-connected systems.

The results of D2.2 framework will help optimize both technical performance and economic viability of HESSs, making them suitable for a wide range of real-world applications. These innovations will help accelerate the deployment of flexible energy storage solutions that can

respond to fluctuating demand and support grid stability one of the core requirements for the future decarbonized energy landscape in the world.

1.2. INTERACTION WITH OTHER WORK PACKAGES AND TASKS

D2.2 is closely interconnected with task T2.3 "Techno-Economic Analysis for HESS Sizing" within the SMHYLES project. The tools developed in D2.2 will directly feed into the sizing studies conducted in Task 2.3. The models will be applied to determine the optimal sizing of HESSs for innovative business cases across different European and extra-European countries. By providing detailed simulations of long-term operations under various scenarios, the tools enable a thorough techno-economic analysis considering capital expenditures (CAPEX), operational expenditures (OPEX), energy market dynamics, and grid service contracts.

1.3. STRUCTURE OF THE REPORT

This report is organized as follows:

- Chapter 1 provides an overview of the report's purpose, scope, and objectives within the SMHYLES project. It also discusses the interactions with other work packages and tasks.
- Chapter 2 introduces the fundamental concepts of hybrid energy storage systems (HESS) and Digital Twins within energy systems. It also provides a description of the main components of HESS, including redox flow batteries (RFB), salt-based batteries ($NaNiCl_2$), and supercapacitors (SC), setting the stage for the detailed modelling discussed in later chapters.
- Chapter 3 details the process of developing models for each HESS component. It includes the specific modelling approaches for redox flow batteries, salt-based batteries, and supercapacitors, covering essential equations.
- Chapter 4 describes the interaction models between different HESS components, particularly between redox flow batteries, salt-based batteries, and supercapacitors. This chapter also outlines the operational strategies and optimization methods used to define multi-objective goals for the HESS systems.
- Chapter 5 summarizes the findings of the report, emphasizing the significance of the developed models and operational strategies. It also proposes potential areas for future research, such as enhancing the interaction modelling of HESS across various scenarios.
- Chapter 6 lists all the sources cited in the report, providing references for the literature, models, and data used.

2. OVERVIEW OF HYBRID ENERGY STORAGE AND DIGITAL TWIN TECHNOLOGIES

2.1. HYBRID ENERGY STORAGE SYSTEMS OVERVIEW

Energy storage systems (ESS) are becoming increasingly more common as a suitable solution to work in tandem with renewable energy plants and to address the challenges noted above. On the energy wholesale side, ESS can store renewable generated electricity when it is plentiful and cheap; and sell to the grid when it is scarce and when there is a high consumer demand, allowing for load shifting and peak shaving [4]. On the ancillary service side, ESS can provide reliable grid support, such as frequency regulation, where they can quickly respond to disruptive grid frequency perturbations and maintain grid frequency at an appropriate level[5].

Over the last decade there has been an increasing interest in ESSs for both electric mobility and stationary storage for power grid applications. ESS can store energy when electricity is cheap and abundant and provide it to consumers at a later time when there is a greater demand. This improves grid reliability and becomes more important as the world adopts smarter grids and has a greater penetration of renewable energy sources (RES). ESSs are beneficial to the grid as they have a range of applications and can provide multiple services. These applications include [6]:

- **Energy arbitrage** – ESS charges by buying off-peak, low-cost electricity from the grid, and selling back to the grid when electricity prices are high.
- **Peak shaving** – A consumer can use the energy stored in a dedicated on-site ESS during times of on-peak power consumption to alleviate some of the high demand on the grid and avoid the high cost of electricity over the period.
- **Frequency response** – ESS can be activated quickly in response to drops in grid frequency, in order maintain grid stability and prevent brownouts or blackouts.
- **Voltage control** – Maintain grid voltage by injecting or absorbing reactive power.
- **Deferral of network transmission and distribution upgrades** – Installing ESS in strategic locations along the grid, closer to areas can help reduce congestion in the transmission and distribution grid, and hence can avoid or defer costly upgrades to the network infrastructure.
- **Capacity Firming of RES** – Support intermittent and variable energy production from RES and balancing the load to output a more constant power supply. E.g.: The amount of power produced by a PV plant may suddenly drop due to cloud cover, hence a battery can step in and compensate for the loss to maintain a constant output.

To work effectively and optimally with a power application, the ESS must be able to fulfil high power and high energy requirements; however, due to the limitations of different storage technologies, a single ESS would typically be designed to meet one of these requirements but

have limited capability for the other. ESS technologies can be categorized into two different classifications based on their characteristics [7]:

- **Primary ESS** – Fulfils high peak power demand and fast transient fluctuations and is more suitable for applications that require fast responses time, high efficiency, high cycle life and dealing with high power peaks.
- **Secondary ESS** – Fulfils the requirements of long storage duration and is characterized by low self-discharge rate and high efficiency.

A HESS aims to overcome the limitations of a single ESS technology, by combining at least one primary ESS type with at least one secondary ESS in a complementary way such that the system can fulfil both high power and high energy requirements of an application. An example of a HESS would be a battery coupled with a supercapacitor due to the complementary nature of the two technologies. Batteries fall in the secondary ESS class as they have high specific energy, low cycle and low power density, and SC's fall in the primary class as have a high specific power, fast charge/discharge times, and a higher cycle [1]. The benefits of using a HESS can include lowering the capital cost of the system, as the secondary ESS only has to be equipped to deal with the average power demand, rather than being over designed to cope with both high power and high energy tasks; HESS can improve overall system efficiency; and HESS can improve cycle life of the system [8].

The SMHYLES project aims to design and demonstrate innovative and sustainable hybrid energy storage systems that combine advanced technologies like batteries and supercapacitors. These systems are designed to store energy for medium to long durations while delivering multiple grid services. The focus is on using materials that are sustainable and less reliant on critical raw materials (CRM), making the solutions more environmentally friendly and scalable.

Key HESS technologies will be implemented within SMHYLES project include:

- Aqueous HESS (AHESS) will be installed in an industrial park in Maia in Demo#01. This system pairs a Vanadium Redox Flow Battery (VRFB) with an aqueous supercapacitor.
- Salt-based HESS (SHESS) will be deployed on the off-grid island of Graciosa in the Azores in Demo#2. This system combines a smart ZEBRA battery and an aqueous supercapacitor.

2.2. DIGITAL TWINS IN ENERGY SYSTEMS OVERVIEW

A Digital Twin is a virtual replica of a physical asset, process, or system that spans its lifecycle, updated from real-time data and using simulation, machine learning, and reasoning to aid decision-making [9]. The concept originated in the manufacturing sector but has since expanded into various industries, including energy systems. Digital Twins enable organizations

to optimize operations, predict maintenance needs, and enhance system designs by providing a dynamic, real-time digital counterpart to physical assets.

In the energy sector, Digital Twins are revolutionizing how energy systems are designed, operated, and maintained. They offer a comprehensive platform for modelling complex interactions within power systems, integrating renewable energy sources, and managing energy storage solutions. Digital Twins model the performance of power generation assets, including conventional power plants and renewable energy sources like wind turbines and solar panels. For example, they can simulate wind farm operations to optimize turbine placement, maintenance schedules, and energy output [10]. By accurately predicting weather patterns and equipment performance, operators can maximize efficiency and reduce downtime. For transmission and distribution networks, Digital Twins enable real-time monitoring and predictive analysis of grid conditions [11]. They help in:

- **Load Forecasting** – Anticipating demand fluctuations to optimize energy distribution.
- **Fault Detection** – Identifying potential failures before they occur to prevent outages.
- **Grid Stability** – Managing voltage and frequency to maintain power quality

By creating Digital Twins of buildings or industrial facilities, energy consumption can be simulated and optimized. This supports demand response programs where consumers adjust their energy usage based on supply conditions, contributing to grid stability and cost savings. Benefits of Digital Twins in Energy Systems [12]:

- **Enhanced Operational Efficiency** – Real-time data and predictive analytics enable proactive management of assets, reducing operational costs.
- **Improved Reliability and Resilience** – Early detection of potential issues prevents outages and enhances system robustness.
- **Informed Decision-Making** – Scenario analysis helps stakeholders evaluate the impact of different strategies and investments.
- **Facilitation of Renewable Integration** – Managing the variability of renewable energy sources through accurate modelling and forecasting.

Digital Twins are particularly valuable for ESSs, such as batteries and supercapacitors [13]. They model the electrochemical processes, thermal behaviours, and degradation mechanisms within storage systems to:

- **Optimize Charging/Discharging Cycles** – Enhancing efficiency and extending battery life.
- **Predict Maintenance Needs** – Scheduling interventions before failures occur.
- **Integrate with Renewables** – Balancing intermittent renewable generation with demand.

Despite the benefits, implementing Digital Twins in energy systems presents challenges:

- **Data Requirements** – High-quality, real-time data is essential, requiring robust sensor networks and data management systems.
- **Complexity and Scalability** – Modelling large, interconnected systems demands significant computational resources and sophisticated algorithms.
- **Cybersecurity Risks** – Increased connectivity exposes systems to potential cyber threats, necessitating strong security measures.
- **Interoperability** – Integrating Digital Twins with existing infrastructure and diverse systems requires standardized protocols and interfaces.

Future Trends, the advancement of technologies like the Internet of Things (IoT), artificial intelligence (AI), and big data analytics is accelerating the development of Digital Twins, including [14]:

- **Integration with AI and Machine Learning** – Enhancing predictive capabilities and autonomous decision-making.
- **Edge Computing** – Processing data closer to the source to reduce latency and improve real-time responsiveness.
- **Standardization and Interoperability** – Developing industry standards to facilitate integration and collaboration across platforms.

In D2.2, the primary focus is the development of digital models to serve as the foundation for future virtual replicas of aqueous HESSs, salt-based HESSs, and supercapacitor systems. These models simulate the hybrid operation of multiple energy storage systems, capturing their interactions and combined capabilities to address dynamic grid demands. Specifically, D2.2 emphasizes creating component-level digital models and conducting long-term techno-economic analyses of HESS, providing input framework for component sizing in Subtask 2.3. This subtask will incorporate various use cases and business cases outlined in D2.1.

The digital models are designed with several critical features:

1. **Integrated Hybrid Modelling**: The tool models the interaction between the two ESSs (batteries and supercapacitors) working together in a hybrid manner. This approach ensures the systems can dynamically adapt to supply various grid requests, such as peak shaving, load levelling, and renewable energy integration.

2. **Techno-economic Optimization**: The digital models are not just technical simulations; they are linked with techno-economic inputs to form an optimization tool. This tool helps address business targets by analysing various scenarios and will be used for determining the optimal size and configuration of HESS for specific applications. The optimization accounts for operational efficiency, cost-effectiveness, and sustainability goals, making it invaluable for system planning and investment decisions.

3. **Microgrid-Level Simulation**: Beyond individual system performance, the digital models will be embedded into microgrid operation models. This integration allows for comprehensive studies of how HESSs can enhance energy reliability, stability, and flexibility at the grid level, providing insights into real-world deployment.

4. **Scalable Application**: Although the tools are specifically designed for the aqueous and salt-based HESSs in this project, their applicability extends beyond. These digital models can be updated and adapted to analyse and optimize other energy storage technologies, enabling a wider impact across the energy storage sector.

The development of this framework is pivotal to the SMHYLES project by providing a virtual environment to test, validate, and refine HESS designs before physical implementation, significantly reducing development risks and costs. Moreover, by simulating real-world operations, they allow for the identification of operational challenges and opportunities, ensuring that the final systems are robust, efficient, and tailored to specific use cases.

2.3. INTRODUCTION TO THE COMPONENTS OF HESS

2.3.1. Redox Flow Batteries

Redox flow batteries (RFB) are a rechargeable type of battery that converts stored chemical energy into electrical energy and vice versa. Like conventional batteries, they take advantage of an oxidation reduction reaction between two charged-storage chemical species, in the form of electrolytes, and convert the stored chemical energy into electrical energy and vice versa. However, the physical arrangement of RFBs vastly differs from a conventional battery: A conventional battery cell is typically comprised of a single compact unit that houses the individual cell components, stores the active species and electrolytes, and facilitates the electrochemical reaction. In contrast, an RFB stores each positive and negative electrolyte in separate external storage tanks and uses dedicated pumps to circulate them between the tanks and a separate reaction cell (or stack of cells). The reaction cell is the site of the redox reaction, where the positive and negative electrolytes are separated by an ion selective membrane. During the redox reaction, and depending on the charge or discharge phase, one electrolyte species will oxidize, and give up an electron(s), while the other will accept them. The transferred electrons migrate via the electrodes in each half of the reaction cell and move across an external circuit. To balance the charge between each electrolyte and maintain electroneutrality, ions will traverse from one electrolyte to the other across the ion selective membrane in the reaction cell [15]. Figure 2.1 illustrates an RFB, and specifically a vanadium redox flow battery (VRFB), which will be the subject of this project. The reaction for this specific RFB is explained later in this section.

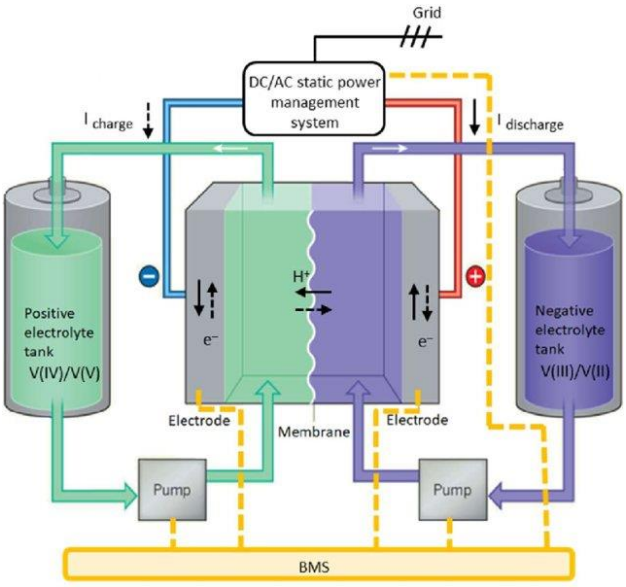

Figure 2.1. A schematic of vanadium redox flow battery [16]

Currently, most common ESSs are comprised of lithium-ion batteries, which are exposed to the following challenges:

- Security of supply of lithium and other critical minerals.
- Limited battery cycle life due to cell degradation over time.
- Safety risks such as thermal runaway resulting in battery fires.
- Lack of long-duration storage capability.

RFBs have unique advantages that can help address some the above challenges and be a suitable alternative to support the grid as an ESS. For example, the amount of energy that an RFB can store is dependent on the size of its storage tanks and concentration of the chemical species dissolved in its electrolytes. Therefore, the energy capacity of an RFB can be scaled by simply increasing the size of the electrolyte storage tanks whereas the power can be increased by increasing the number of cell stacks [17]. This ease of scalability is a particular benefit for long duration storage applications. Other advantages of RFBs include their high cycle life of up to 20,000 cycles, compared to lithium ion batteries, which are about 5,000 cycles (for LFP) [18]; there is little to no self-discharge as the two electrolytes are stored separately; short overloads do not damage the battery; and, they are safer as they do not contain flammable electrolytes [19], hence thermal runaway is not a risk like in lithium ion batteries [20]. The main drawbacks of RFBs are low power and energy densities compared to other batteries, which is due to their large size and due to the lower concentrations of redox species that can be achieved. Because of this limitation, RFBs are not appropriate for mobility applications and are better suited to stationary storage in grid applications. Additionally, the presence of parasitic shunt currents due to the conductive electrolytes, the ohmic losses and the pumping power affect their efficiency, which is typically around 75% [21].

2.3.2. Salt-based Batteries

Salt-based batteries, specifically sodium-nickel chloride ($NaNiCl_2$) batteries, are a type of high-temperature molten salt battery known for their robustness and suitability for large-scale energy storage applications.

Some advantages of $NaNiCl_2$ batteries are as follows:

- **High Energy Density:** $NaNiCl_2$ batteries offer energy densities up to 120 Wh/kg, making them suitable for applications requiring substantial energy storage within a compact footprint. So, these types of batteries can be used in stationary energy storage applications due to their high energy density and are suitable for balancing supply and demand, backup power systems, frequency regulation, and renewable energy integration [22].
- **Good Cycle Life:** They exhibit a life of ~4,500 cycles [23] due to the stable chemistry and minimal self-discharge when maintained at operating temperatures.
- **Wide Operating Temperature Range:** Their high temperature operation allows for consistent performance in various environmental conditions.
- **Abundance of Raw Materials:** Sodium and nickel are more abundant and less expensive compared to lithium, reducing material costs and supply chain risks.
- **Safety:** The all-solid construction eliminates risks associated with liquid electrolytes, such as leakage or flammability.

Despite the wide range of advantages of $NaNiCl_2$ batteries, the challenges, which mostly depend on the thermal control, can be mentioned as follows [24]:

- **High Operating Temperature**: The requirement to maintain elevated temperatures increases energy consumption for heating and poses insulation challenges.
- **Thermal Management:** Effective thermal management systems are essential to maintain temperature and ensure safety, adding complexity and cost.
- **Start-up Time:** Cold-starting the battery from ambient temperatures requires time and energy to reach operational temperatures.
- **Material Degradation:** Prolonged exposure to high temperatures can lead to material degradation, affecting long-term performance.

Features like low-cost, high-energy density, high safety, and high recyclability rate have made these batteries an interesting choice for various applications. The abundance of sodium, which is one of the key elements of $NaNiCl_2$ battery cells, facilitates the manufacturing and usage of these batteries [25]. The technology used has already been commercially produced and widely tested [26] for network storage and to integrate wind and solar power resources [27]. Commonly referred to as ZEBRA (Zero Emission Battery Research Activities) batteries, they

operate at elevated temperatures (270–350°C) where the electrolyte is molten, allowing for efficient ion transport and high-power density.

Figure 2.2 shows an overview of the cell structure of for these batteries. At the core of the cell is a molten sodium anode, with an outer nickel chloride cathode, separated by a solid ceramic electrolyte made of beta-alumina solid electrolyte (BASE). When the battery discharges, sodium ions migrate through the BASE to react with nickel chloride, forming nickel and sodium chloride, and during charging, this reaction is reversed [24]. During charging, this reaction is reversed [24].

As mentioned, the Sodium/Nickel chloride cell mechanism is based on the transport of sodium ions from the positive electrode to the negative one during charging and in the opposite direction while discharging. The battery is composed of several critical components that contribute to its efficient energy storage and conversion capabilities. At the core of the cell structure (see Figure 2.2) is the sodium anode, which interacts with the nickel chloride cathode through a solid electrolyte made of beta-alumina. Having the same function as a liquid electrolyte in a Li-ion battery, the ionic conductivity of the BASE increases significantly with the temperature: at 300 °C the conductivity is equal to about 0.25 S/cm and at 350 °C to 0.4 S/cm, facilitating the movement of sodium ions while preventing the direct contact between the anode and cathode, thus ensuring safety and stability. The tube also contains a secondary electrolyte consisting of molten salt, typically sodium tetra chloroaluminate ($NaAlCl_4$) saturated with sodium chloride (NaCl), filling the pores in the positive electrode compartment, which operates at high temperatures to maintain the ionic conductivity. Additionally, the cell is encased in a robust ceramic or metal housing that can withstand the operational temperatures (between 270 °C and 350 °C) and pressures. The overall battery assembly integrates these cells into a larger module, complete with thermal insulation and management systems to maintain optimal operating conditions (see Figure 2.3). The electrochemical reaction equations for the cell are summarised in equations (1) to (3) [23]and the points below describe some details of the cell and overall battery components:

- **Anode:** Molten sodium (Na), where during discharge, sodium atoms lose electrons and are converted into sodium ions, which migrate through the electrolyte to the cathode.
- **Cathode:** Nickel chloride ($NiCl_2$), with potential inclusion of iron chloride ($FeCl_2$) to enhance performance. Sodium ions combine with $NiCl_2$ during discharge, producing nickel (Ni) and sodium chloride (NaCl).
- **Electrolyte:** Primary electrolyte is solid beta-alumina ceramic electrolyte that facilitates the movement of sodium ions while acting as an electronic insulator. The secondary electrolyte is molten sodium tetra chloroaluminate (NaAlCl), located in the cathode chamber and enhances ionic conductivity. The crystalline structure of the

electrolyte allows the flow of sodium ions (fast ionic transport) while acting as a good electric insulator.

- **Separator:** The solid electrolyte also acts as a separator between the molten sodium anode and the cathode materials, preventing direct contact between the anode and cathode, thus avoiding short circuits and enhancing safety.
- **Housing and Thermal Management System:** The insulated enclosure is designed to maintain operational temperatures (270°C to 350°C). Thermal regulation incorporates heating elements to ensure optimal working conditions and energy efficiency. This is an important aspect, as the battery is unable to operate below the minimum temperature set-point of ~270°C. The battery assembly also includes integrated heaters which will keep the battery above this minimum temperature by either using external power (if available) or self-discharge (if battery has sufficient SOC).

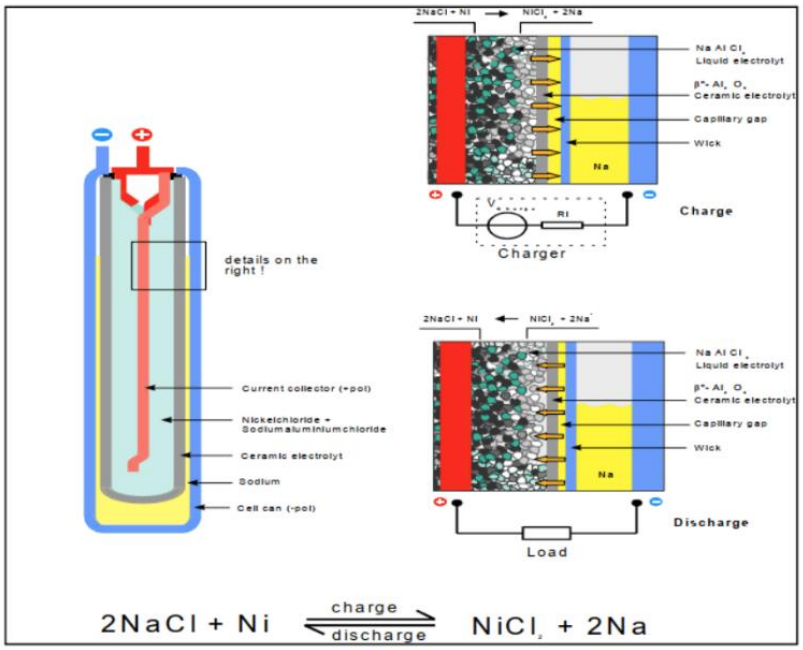

Figure 2.2. Cell details and internal chemical reactions [28]

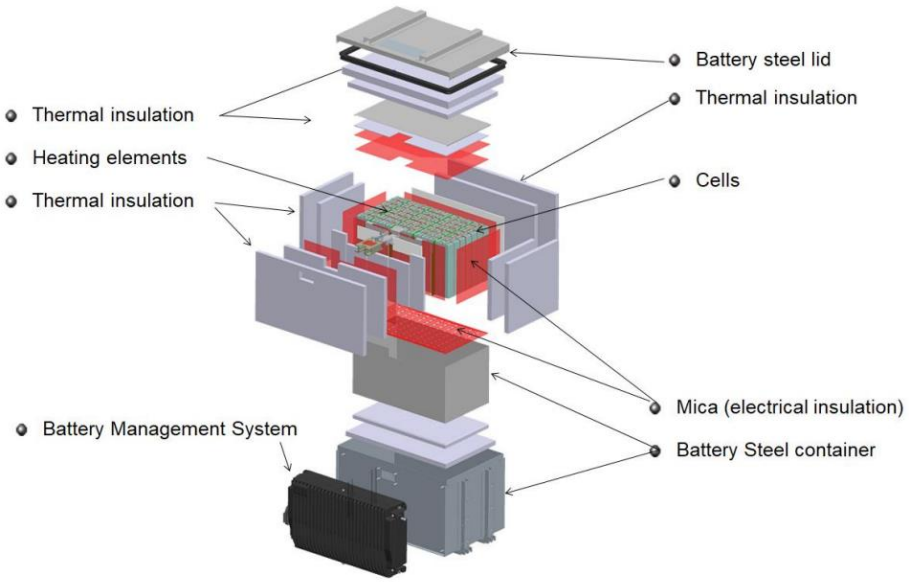

Figure 2.3. $NaNiCl_2$ Battery Components [29]

The overall reaction for the cell is summarized below, providing a voltage of ~2.58 V:

$$NiCl_2 + Na \rightleftharpoons 2NaCl + Ni \quad (1)$$

Reaction at the positive electrode:

$$NiCl_2 + 2Na^+ + 2e^- \rightleftharpoons 2NaCl + Ni \quad (2)$$

Reaction at the positive electrode:

$$2Na \rightleftharpoons 2Na^+ + 2e^- \quad (3)$$

At the end of the discharge cycle, some of the sodium metal may be left behind in the sodium compartment of the cell, and unable to take part in the electrochemical reaction. This would cause the cell to have a reduced cell capacity. To avoid this, aluminium powder is added into the sodium, as a secondary electrolyte. This reacts with the sodium producing sodium chloride and metallic aluminium through the following reaction, with a voltage of 1.58 V [30].

$$4NaCl + Al \rightleftharpoons NaAlCl_4 + 3Na$$

In the discharge process, oxidation occurs at the sodium electrode and reduction at the porous electrode, which means that the sodium ions pass through the beta-alumina ($\beta'' - Al_2O_3$), as the first solid electrolyte, and also through $NaAlCl_4$, as the secondary electrolyte, and finally to the reaction zone of $NiCl_2$, spread over the nickel spheres [23].

2.3.3. Supercapacitors

Significant technological advancement in capacitor technology has resulted in the development of supercapacitors, which have a capacitance of 10,000 times that of a conventional capacitor [31]. They can achieve high-power densities of 10–20 kW/kg, making them useful in applications with high charge /discharge requirements in extremely short periods (< 1 s to 10s). However, they are not a replacement for other ESSs, such as batteries, as they have relatively low energy densities corresponding to 3-5 Wh/kg [32]. Other advantages for SCs include a long lifetime (~1,000,000 cycles), operation over a wide temperature range, good safety & reliability, and require little maintenance [33].

Common applications for SCs include electric vehicles, which are widely used to recover the regenerative energy during braking. SCs can handle large surge currents, compared to batteries, and hence they can absorb any excess power during regenerative braking. Additionally, they can make up for any power deficit in surging demand, such as periods of high vehicle acceleration. The use and operation of SC within an EV can complement the operation of the battery: the battery can operate in a continuous and smooth manner, while the SC deals with the fluctuating loads or surges due to vehicle acceleration/deceleration, improving the overall lifetime of the battery.

Other applications include DC microgrids, where a dwelling or community is powered by a renewable energy source and partly supplemented by the utility grid. Voltage and power fluctuations can have negative impacts on the DC bus, where the ESSs cannot meet the high load dynamics. A SC can be employed to support the transient power due to the fluctuating loads present in the DC microgrid [34].

A typical SC has two porous electrodes submerged in an electrolyte (see Figure 2.4). The electric field produced between the electrodes and electrolyte is used to store the energy. An ion-conductive membrane separates the two electrodes and permits ion flow while avoiding short circuits between them.

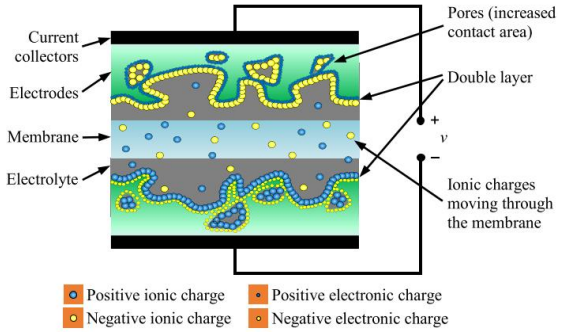

Figure 2.4. Operation principle of an SC cell [34]

3. DEVELOPMENT OF THE HESS MODEL

3.1. OVERVIEW OF THE MODEL DEVELOPMENT PROCESS

Subtask 2.2.1 of the SMHYLES project is dedicated to the development and enhancement of advanced simulation tools to model Aqueous and Salt-based Hybrid Energy Storage System (HESS) technologies at both the component and system levels. This task emphasizes creating detailed and accurate models that simulate the electrical, thermal, and chemical dynamics of HESS components under various operational scenarios. By building robust simulations, Subtask 2.2.1 aims to facilitate a comprehensive understanding of these technologies and their integration potential for hybrid storage solutions, laying the groundwork for effective deployment.

The simulation outputs generated from this subtask serve multiple purposes, with a primary goal of enabling the optimal design and implementation of digital models for HESS systems at the chosen demonstration sites. The digital models are expected to reflect real-time and predictive behaviours of the HESS systems, providing insights for monitoring, control, and decision-making in energy storage management for the future Digital Twins utilizations. These simulations also help refine system designs and enhance performance efficiency, ultimately contributing to a more reliable and responsive energy storage infrastructure.

Key objectives and methodologies include:

- **Detailed Component-Level Modelling**: This includes developing precise models for each component within the HESS, such as RFB, salt-based batteries, and SC. The modelling approach considers various parameters like charge/discharge rates, temperature dependencies, degradation and aging Effects, etc.
- **System-Level Integration**: System-level simulations are carried out to assess the performance of the HESS as an integrated system. This involves examining interactions between components, optimizing energy flows, managing power delivery, and ensuring stability under different load conditions and use cases.
- **Testing Under Multiple Scenarios**: To capture real-world performance, simulations are conducted across a range of operational scenarios, including varying load profiles, renewable generations, and other relevant conditions.
- **Integration with Control Algorithms**: The simulation tools are designed to be compatible with control algorithms that manage the HESS. By integrating these algorithms within the simulations, the project can explore optimal management and long-term planning for enhancing technical aspects like system responsiveness, efficiency, and lifetime, as well as economic factors like energy arbitrage, and so on.
- **Data Analytics and Validation**: To ensure accuracy, the simulation outputs are validated against experimental data where available. This step is crucial for refining the

models and ensuring that they accurately reflect physical behaviour and their limits. This step will be discussed in the next chapter.

3.2. MODEL OF THE REDOX FLOW BATTERY

3.2.1. Mathematical Model of the Vanadium Redox Flow Battery

A mathematical model for the VRFB was created in Python by developing a set of power flow equations that defined the dynamic behaviour of the battery, as per equations (30) and (31) in sub-section 3.2.1.6. The development of the model was based on the equivalent circuit method and the Nernst equation and considered the losses due to pump power usage and degradation of the electrode and electrolyte. This section outlines the theory behind the VRFB, along with the relevant equations that govern the battery's physics, which were combined to develop the power flow equations. Table 3-1 provides a summary of the parameters and variables that are used in the various equations to model the VRFB.

Table 3-1. Summary of variables and parameters used to model a VRFB

Symbol	Description	Value	Unit
$A_{membrane}$	Effective area of the cell membrane	1500- 2000	cm^2
Cap_{max}	Maximum capacity possible capacity after a rebalancing procedure	-	%
C_H	Hydrogen ion concentration	-	mol/L
$C_{v\,i}$	Vanadium ion concentration, where i corresponds to a particular species	-	mol/L
$C_{v\,total}$	Total vanadium ion concentration in each tank	1.6	mol/L
D_{total}	Overall fade from total electrolyte degradation	0.442 [36]	%/cycle
D_{ED}	Electrolyte decay rate (capacity loss per cycle)	0.055 [36]	%/cycle
E_{stored}	Total energy storage capacity of the VRFB	-	J
E^0	Standard cell potential	-	-
E^θ	Nominal cell potential at 50% SOC	1.41 V	V
f_{cap}	Fraction of original stored energy capacity	-	%
F	Faraday Constant	96,485	C/mol
I_{RFB}	Terminal current for the VRFB	-	A
$m_{electrode}$	Electrode mass	0.2	kg
N_{cells}	Number of cells in the cell stack	-	-

Symbol	Description	Value	Unit
n_{cyc}^{S}	Number of cycles since last electrolyte replacement (where $Cap_{max} = 100\%$)	-	Cycles
n_{cyc}^{R}	Number of cycles since rebalancing	-	Cycles
$\Delta p_{hydraulic}$	Pressure drop in the cell stack of the VRFB	100,000	Pa
r_m	Area specific cell membrane resistance	1.4 – 1.6	Ω cm^2
$R_{electrode}$	Internal resistance of the cell due to electrode degradation	-	Ω
$R_{membrane}$	Cell membrane resistance	-	Ω
$R_{RFB\ internal}$	Total internal resistance of VRFB	-	Ω
R	Ideal gas constant	8.314	J/K mol
$SOC_{RFB\ max}$	Maximum allowable SOC	80	%
$SOC_{RFB\ min}$	Minimum allowable SOC	10	%
T	Electrolyte Temperature	303	K
v_{cell}	Cell terminal voltage	-	V
$v_{terminal}$	Battery terminal voltage	-	V
v_i	Cell overpotential (activation, ohmic or concentration)	-	V
$V_{electrolyte}$	Volume of the electrolyte in one tank	-	L
$\dot{V}_{pump}$	Volumetric of the pumps	-	L/s
Z	Number of electrons transferred in the VRFB redox reaction	1	-
η_{pump}	Pump efficiency	75	%

3.2.1.1. Electrochemical Equations

A vanadium redox flow battery (VFRB) utilizes an oxidation reduction chemical reaction between different species of vanadium ions, to charge and discharge the battery. During discharge, the Vanadium (II) ion in the negative half-cell releases an electron and becomes Vanadium (III). In the positive half-cell, Vanadium (V) absorbs the released electron to become Vanadium (IV). The opposite reaction occurs during charging, and these reactions are summarized by the chemical equations (4) to (6) below [38]. The reaction also requires the transfer of 2 protons (H^+) across the ion selective membrane to balance the charge of the electrolytes. The potential difference between the electrodes is ~1.26 V. The vanadium ions

are dissolved in H_2SO_4 and water, and the total vanadium ion concentration is about 1 -2 M per tank [39].

$$VO^{2+} + H_2O + V^{3+}\,(discharge) \;\rightleftharpoons\; (charge)\; VO_2^{+} + V^{2+} + 2H^{+} \quad (4)$$

Where the reaction in the positive half-cell is:

$$V^{4+} - e^{-}\;\; (discharge) \;\rightleftharpoons\; (charge)\; V^{5+} \quad (5)$$

And the reaction in the negative half-cell is:

$$V^{3+} + e^{-}\;\; (discharge) \;\rightleftharpoons\; (charge)\; V^{2+} \quad (6)$$

3.2.1.2. Equivalent Circuit Model and the Nernst Equation

There are a wealth of studies in published literature that have used equivalent circuit models to simulate VRFBs, which is a typical method for simulating batteries [40]. These vary from simple R circuit models to more extensive, multi-order RC circuits to capture the various electrochemical components and aspects of a VRFB [41]. Figure 3.1 below shows a general example of how a VRFB cell can be modelled using a simple equivalent circuit, where E_{OCV} is the cell open circuit voltage, $R_{RFB\ internal}$ is the total internal resistance of all the cells, and I_{RFB} and v_{RFB} correspond to terminal current and voltage, respectively. The general equation (7) can also be used to describe a VRFB, where N_{cells} is the number of cells stacked in series.

$$v_{RFB} = N_{Cells}E_{OCV} + I_{RFB}R_{RFB\ internal} \quad (7)$$

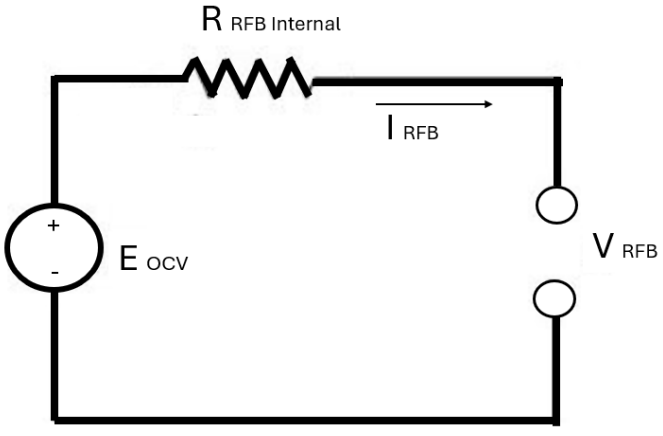

Figure 3.1. Example of a simple circuit model for a VFB.

At the heart of the VRFB equivalent circuit model is the Nernst equation which determines the VRFB cells' open circuit voltage (OCV), E_{OCV}. The Nernst equation is shown below in equation (8) and all relevant parameters are summarized in **Error! Reference source not found.**. Equation (8) can be reduced into equation (11) via several assumptions and simplifications

using equation (10) and intermediary equation (9)[37]. This process is summarized in the subsequent bullet points.

$$E_{OCV} = E^0 + \frac{2RT}{F}\ln\left[\left(\frac{C_{V\,2}C_{V\,5}{C_H}^2}{C_{V\,3}C_{V\,4}}\right)\left(\frac{\gamma_{V\,2}\gamma_{V\,5}{\gamma_H}^2}{\gamma_{V\,3}\gamma_{V\,4}}\right)\right] \quad (8)$$

$$E_{OCV} = E^\theta + \frac{2RT}{F}\ln\left[\frac{C_{V\,2}C_{V\,5}}{C_{V\,3}C_{V\,4}}\right] \quad (9)$$

$$SOC = \frac{C_{V\,2}}{C_{V\,2}C_{V\,3}} = \frac{C_{V\,5}}{C_{V\,4}C_{V\,5}} \quad (10)$$

$$E_{OCV} = E^\theta + \frac{2RT}{F}\ln\left[\frac{SOC_{RFB}}{1 - SOC_{RFB}}\right] \quad (11)$$

- The standard potential E^0, can be replaced by the cell nominal potential E^θ which is measured experimentally at a battery SOC of 50%. This corresponds to ~1.35 to 1.4V for VRFBs.
- The activity coefficients for the different vanadium ion species, denoted by $\gamma_{V\,i}$ can be assumed as constant. Their effects are considered by the nominal potential, E^θ, and hence they can be removed from the Nernst equation.
- The concentration of hydrogen ions, denoted by C_H, can also be assumed as constant and is accounted for by the nominal cell potential E^θ. Hydrogen concentration can be removed from the Nernst equation.
- Equation (10) shows how the VRFB's SOC can be determined by the concentrations of the various vanadium ion species, $C_{V\,i}$. This can be incorporated into equation (9) to finally arrive at equation (11).

The total energy stored in the VRFB is summarised by equation (12) below [37], where $V_{electrolyte}$ is the electrolyte volume and $C_{v\,total}$ is the electrolyte concentration.

$$E_{stored} = E^\theta V_{electrolyte} F C_{v\,total} \quad (12)$$

Internal losses in a battery cell are due to the various ohmic losses, activation overpotential and concentration overpotential [42]. This is summarized below by the cell terminal voltage equation (13) with the various voltage drops (v_i) due to these losses.

$$v_{Cell} = E_{OCV} - v_{activation} - v_{Concentration} - v_{ohmic} \quad (13)$$

These voltage drops are attributed to the corresponding resistances of various components and effects in the cell. For example, the ohmic losses are due to resistances of the membrane, electrodes, bipolar plates, electrolytes, and contact. Many of these resistance values, particularly those for activation and concentration overpotential, can be complex and extremely difficult to determine; hence one study recommended only determining the total membrane resistance and increasing its value by 80 – 100% to consider the total internal

resistance of the battery cell [43]. The membrane ohmic resistance is relatively simple to calculate via equation (14), where r_m corresponds to the area specific resistance of the proton exchange membrane, and typically corresponds to 1.5 – 2.5 Ω cm^2 for the types of membranes used in vanadium redox flow batteries [44]. The effective area of the membrane, $A_{membrane}$, corresponds to the total area of interface between the electrolyte and the membrane and is dependent on the specific flow path scheme of the cell.

$$R_{membrane} = r_m A_{membrane} \quad (14)$$

3.2.1.3. Pump Usage Losses

Not shown in the equivalent circuit diagram (Figure 3.1) and the VRFB terminal voltage equation (7) are the effects of the pump power usage. As explained earlier, VRFBs use two dedicated pumps to transfer the electrolytes between their storage tanks and the reaction cells during charging and discharging. This requires power to do so and hence affects the VRFBs performance and overall efficiency. Because pump power usage is parasitic it can be described as an external loss and must be considered in the model [45]. The pumping power consumption can be calculated via equation (15), which determines the pump flowrate based on the redox reaction rate; and equation (16), which determines the pump power based on the calculated flowrate, the hydraulic pressure drop of the cell stack, $\Delta p_{hydraulic}$, and the pump efficiency, η_{pump} [46].

$$\dot{V}_{pump} = \frac{2 * N_{cells} * I_{RFB}}{Z * F * C_{v\,total} * SOC_{RFB\,min}} \quad (15)$$

$$P_{pump} = \frac{2 * \Delta p_{hydraulic} * \dot{V}_{pump}}{\eta_{pump} * 1000} \quad (16)$$

3.2.1.4. Electrode Degradation

Compared to lithium-ion batteries, VRFBs have a high cycle life of 12,000 – 20,000 cycles [47], however that is not to say that they do not undergo degradation. Degradation of VRFBs and RFBs in general is not entirely understood, as most of the research has focused on improving VRFB materials to improve performance and reduce costs [48]. It is important to understand degradation and the effects of aging, as this can decrease efficiency, capacity and overall performance of the system. Based on the limited publications so far, the main causes for degradation of VRFBs are due to aging of the electrolytes, membranes, bipolar plates, and electrodes [49].

Electrode degradation has been found to account for a major portion of the overall performance loss. The authors of [50] carried out a study on VRFBs and had estimated that 10 – 55% of the performance loss was due to the electrode degradation, and the remaining was due to ohmic losses. The electrodes in VRFBs are mostly comprised of carbon and graphite felt due to their large specific surface area, good chemical stability and high electrical conductivity

[51]. The degradation of these is due to wear down over time due to mechanical wear, thermal degradation and exposure to high humidity [52]; however, the dominant factor will depend on the specific operating conditions of the VRFB. This wear and tear compromises the electrodes' ability to hold electrons during charging and discharging and therefore increases the battery's internal resistance and diminishes its efficiency and performance. A study investigated the effects of aging using CTR methods, based on 8 days of simulation data [53]. From their results, two linear models were obtained for the increase in internal resistance due to degradation of the electrodes: Aging effects between 1-4 days, and aging effects 4-8 days. Equations (17) and (18) below summarise the aging effects of the electrode, where $m_{electrode}$ denotes the mass of the electrode.

$$R_{electrode} = \frac{[4.5 * days + 12.1] * 10^{-6}}{m_{electrode}} \qquad 0 < days \leq 4 \tag{17}$$

$$R_{electrode} = \frac{[0.7 * days + 31] * 10^{-6}}{m_{electrode}} \qquad 5 \leq days \tag{18}$$

Electrolyte degradation occurs due to different mechanisms, which includes H_2 gas evolution at the negative electrode, O_2 gas evolution at the positive electrode, oxidation of the V^{2+} ions and vanadium crossover between the half-cells. Additionally, fluctuations in electrolyte concentrations and temperature will affect the ion solubility causing precipitation which can lead to blockages in the hydraulic circuit and affect performance. Overall, the degradation of electrolytes affects the rate of the electrochemical reaction in the cell stack, causing an efficiency loss of the system [48].

The cell membrane acts as the separator between the catholyte and the anolyte, while facilitating ion transfer. The membrane is required to have high proton conductivity while blocking the transfer of vanadium ions to prevent crossover and imbalance between the half-cells. Degradation of the membrane reduces its ability to conduct protons and/or prevent crossover of Vanadium ions, reducing the VRFB's capacity and increasing its internal resistance. Degradation of the membrane can be due to a decrease in its chemical stability. Because the electrolytes contain H_2SO_4 as a solvent, it creates a harsh environment that can cause possible corrosion of the polymer material [54].

3.2.1.5. Electrolyte Degradation

Electrolyte degradation was also considered in the model and was based on the number complete charge/discharge cycles carried out by the RFB. Although there are many modes in which this can occur, not all of them are well understood. For this project, two degradation mechanisms were considered [36]:

- Reversible vanadium cross-over – Due to undesirable transport of active species across the cell membrane. Can be addressed via electrolyte rebalancing.
- Irreversible electrolyte decay – Due to a shift in oxidation states in the vanadium species which results in degradation of electrolyte and causes a permanent loss of energy capacity. Can only be reversed by replacing the electrolyte.

The overall capacity fade is demonstrated in the example Figure 3.2.Looking at the capacity fade profile in the diagram, the following can be observed:

- At the beginning of the RFB's life, it has an energy storage capacity of 100%.
- Energy storage capacity reduces with overtime as a function of number of charge/discharge cycles.
- Once the capacity reduces to a certain set-point (80% in the example), a rebalancing procedure is carried out to reverse the capacity fade due to the cross-over mechanism. The energy capacity cannot be restored to 100% from this process, due to the contributions of the irreversible electrolyte decay mechanism.
- After each subsequent rebalancing process, the restored maximum energy capacity continues to decrease, until it also reaches a certain threshold (~81% in the example). At this point, a service can take place where the entire electrolyte is replaced. This annuls the capacity fade due to cross-over and material decay, and it restores the RFB's maximum energy capacity to 100%.

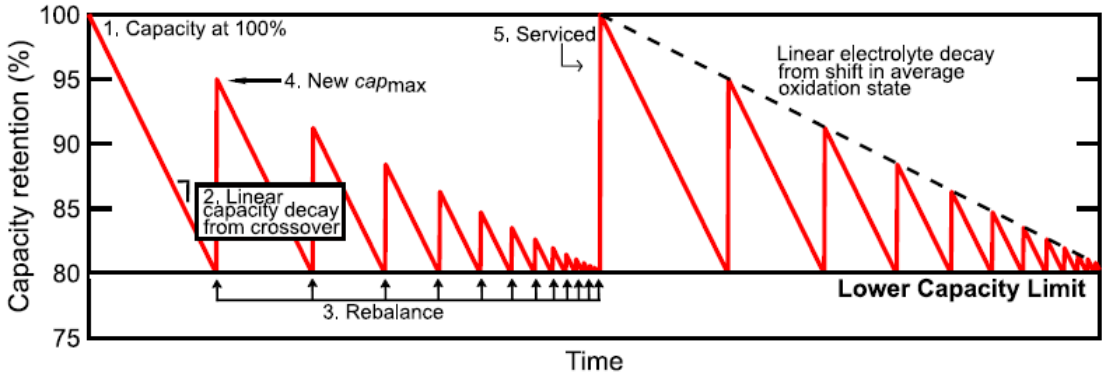

Figure 3.2 Example of RFB capacity fade due to electrolyte degradation [36]

Linear electrolyte degradation was implemented into our RFB model, based on previous studies conducted for VRFBs [36]. This electrolyte degradation model determined the reduced maximum energy storage capacity of the RFB due to the cross-over and electrolyte decay mechanisms, and is based on equations (19) to (21) and the parameters summarized in Table 3-1.

The maximum storage capacity of the RFB considers the effects of the irreversible decay as described in equation below (19). This is the RFB's storage capacity immediately after a rebalancing procedure.

$$Cap_{max}\left(cyc = n_{cyc}^{S}\right) = 100\% \; - \; D_{ED} * n_{cyc}^{S} \tag{19}$$

The maximum storage capacity can be used to calculate the fraction of original storage capacity (f_{cap}). This is the percentage of maximum energy stored when considering the overall effects of the electrolyte degradation (effects due to cross-over + electrolyte decay). This is given by the following equation:

$$f_{cap} = \; Cap_{max}(cyc = n_{cyc}^{S}) - D_{total} * n_{cyc}^{R} \tag{20}$$

Finally, the reduced maximum energy storage capacity of the RFB at time = T is given by the equation below:

$$E_{stored}\left(cyc = n_{cyc}^{S}\right) = E_{stored}(cycles = 0) * f_{cap} \quad (21)$$

3.2.1.6. Power Model Equations

Python was used to develop a model that can simulate the performance of a VRFB using the equations described in sub-sections 3.2.1.2 to 3.2.1.5. A diagram illustrating the developed equivalent circuit model of the VRFB model is shown in Figure 3.3 and Figure 3.4, illustrating the charging and discharging cycles, respectively. Equations (22) and (23) represent the power flow in the VRFB during these respective cycles. Looking at the charging cycle, the term $P_{RFB\ input}$ corresponds to the total power supplied to the battery via some external supply. A portion of this power is used to power the VRFB's pumps, denoted by P_{pump}. The terminal power, $P_{RFB\ terminal}$, is the net input power of the pump power demand, which enters the VRFB cell stack and used to carry out the redox reaction. Due to the internal resistance, a portion of this power is lost, denoted as $P_{RFB\ loss}$, and the power net of this loss is the battery internal power, denoted as $P_{RFB\ Internal}$. The derivative of $P_{RFB\ Internal}$ is the net energy received and stored into the VRFB, as per equation (24). During the discharging phase, the reverse occurs where the VRFB will supply power, $P_{RFB\ output}$, as required by some external demand. The VRFB will discharge a total power of $P_{RFB\ internal}$, which is the derivative of the total energy used by VRFB. The power supplied by the VRFB, $P_{RFB\ output}$, is the battery internal power net of the internal losses and pump power demand.

$$P_{RFB\ Internal} = P_{RFB\ input} - P_{pump} - P_{RFB\ loss} \quad (22)$$

$$P_{RFB\ internal} = P_{RFB\ output} + P_{pump} + P_{RFB\ loss} \quad (23)$$

$$E_{RFB} = \int P_{RFB\ internal}\, dt \quad (24)$$

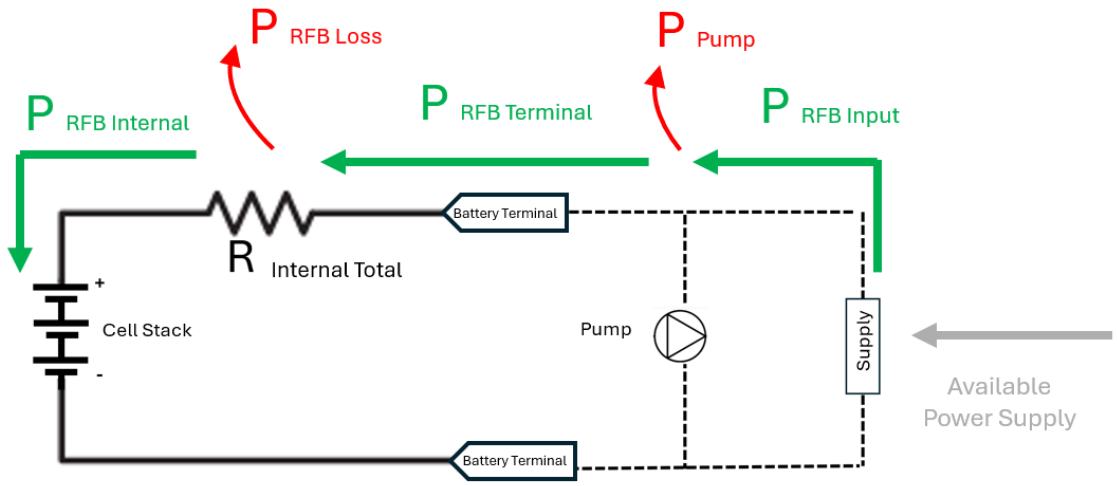

Figure 3.3. VRFB equivalent circuit model illustrating the charging cycle.

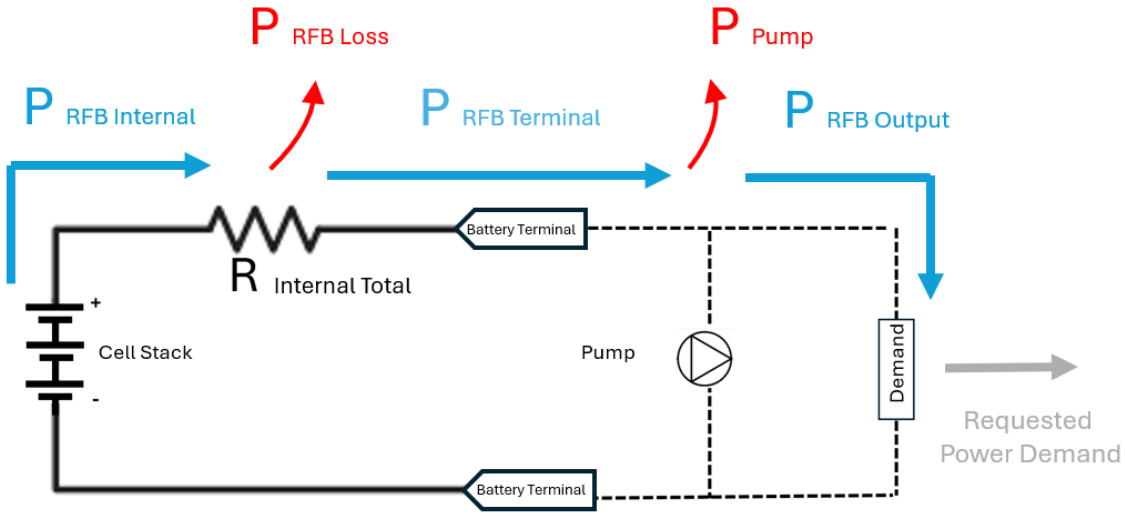

Figure 3.4. VRFB equivalent circuit model illustrating the discharging cycle.

In the application of the model, the known inputs are $P_{RFB\ input}$ and $P_{RFB\ output}$ and it is desired to determine $P_{RFB\ Internal}$ for different load profiles. Using equations (22) and (23), the VRFB's terminal current, I_{RFB} , can be derived via a set of quadratic equations for the charging and discharging phase. To proceed with developing the quadratic equations, the pump flowrate equation (15) is combined with the pump power equation (16) to yield (25). All components of these equations are constant, except for current and hydraulic pressure drop; however, to maintain simplicity it is assumed that the pressure drop in the flowrate equation is constant, such that all constant values can be lumped into a single parameter, C_{pump}, to arrive at equation (26). The assumption that pressure drop remains constant is not accurate because it will vary with the pump flowrate. Several studies have reported cell stack pressure drop values between 30 – 100 kPa [7] and hence the greater value of 100 KPa was

adopted as the constant value for this system, to be conservative. Adopting a more accurate pressure drop calculation should be considered for future work. Additionally, the pressure drops in other hydraulic components, such as the inlet and outlet piping connecting to the VRFB cell stacks have been ignored and should be considered in future work for better accuracy.

$$P_{pump} = \frac{2 * \Delta p_{hydraulic}}{\eta_{pump}} * \frac{2 * N_{cells}}{Z * F * C_{v\,total} * SOC_{RFB\,min}} * I_{RFB} \quad (25)$$

$$P_{pump} = C_{pump} * I_{RFB} \quad (26)$$

The power losses due to the internal resistance can be determined by Ohm's law. For the current model, the internal cell resistance was based on the membrane resistance only, for simplicity. It is also possible to consider the losses from the other resistances by increasing the membrane resistance by 80 -100% as mentioned by [43]. The resistance due to degradation effects of the electrodes has also been considered, which was the only degradation mechanism that had a relatively simple mathematical model that could easily be implemented into the project's VRFB model. Previous studies have indicated that this degradation mechanism can be a significant contributor to internal losses, which is why it was included in the model [50].

The total internal resistance can be given by the sum of the membrane resistance and degradation resistance, multiplied by the number of cells in the stack as per equation (27). The total internal resistance and the resultant internal power loss in the VRFB can be calculated by equation (28).

$$R_{RFB\,internal} = N_{cells}\,(1.8 * R_{Membrane} + R_{Electrode}) \quad (27)$$

$$P_{RFB\,Loss} = {I^2}_{RFB} * R_{RFB\ internal} \quad (28)$$

Lastly, the internal battery power, which is the derivative of the energy released or absorbed by the VRFB during discharge or charge, respectively, can be calculated using ohm's law. It is the product of the total open circuit voltage of the cell stack with the VRFB terminal current (equation (29)).

$$P_{RFB\,internal} = (N_{cells} * E_{OCV}) * I_{RFB} \quad (29)$$

Using the power balance equations and the equations derived above, two quadratic equations are developed that can be used to determine the VRFB terminal current, I_{RFB}. Equations (30) and (31) correspond to the charging and discharging phases, respectively.

$$-{I^2}_{RFB} R_{RFB\,internal} - I_{RFB}\left(N_{cells} * E_{OCV} + C_{pump}\right) + P_{RFB\,input} = 0 \quad (30)$$

$${I^2}_{RFB} R_{RFB\,internal} + I_{RFB}\left(C_{pump} - N_{cells} * E_{OCV}\right) + P_{RFB\,output} = 0 \quad (31)$$

The input parameters used for the VRFB model are summarized in Table 3-1, some of which were based on the supplier datasheet. As the supplier provided parameters were proprietary and commercially sensitive, some of these values have been presented as a range. The number of cells in series depended on the rated power of the simulated VRFB, where 1 cell corresponded to a rated power of 0.15 - 0.2 kW. The efficiency of the VRFB can vary based on the charging and discharging conditions of the battery such as the amount of input (or output) power, and the SOC of the battery. However, running preliminary simulations with the VRFB charging and discharging at its rated power, efficiencies of about 75% were achieved, which is within the range of what has been reported in literature and by suppliers [55].

3.2.2. VRFB Model Results

3.2.2.1. VRFB Model Demonstration

Figure 3.5 shows an example of a charging and discharging power profile and SOC for the VRFB model, and Figure 3.6 shows the corresponding cell voltage and terminal current. This simulation used a hypothetical 300 kW / 1200 kWh VRFB, with an initial minimum SOC of 10%, and carried out a complete charge/discharge cycle over a 12-hour period, in 1-minute time-steps. For the first 6 hours, the VRFB recharged itself with an externally available power supply of 300 kW. After 6 hours, there is no more externally available power supply, and instead there is a consumption load of 300 kW, where the VRFB discharges to try and meet this demand. During the charging phase the following is observed:

- At time t = 0 min to t = 83 min:
    - 300 kW (before losses) is delivered to the battery, corresponding to a total of 415 kWh of energy delivered from the external supply.
    - The net energy received by the battery is ~ 374kWh and corresponds to a net delivered power to the VRFB of 255 to 272 kW over the period. The discrepancy between the externally supplied energy of 415 kWh and the net received energy of 374 kWh is due to the battery efficiency corresponding to internal losses and the power used by the pumps.
- At time t = 84 min to t = 310 min:
    - The battery's terminal cell voltage has reached the upper limit of 1.5 V and the accepted charging power by the battery is derated to keep below this limit.
    - There is still 300 kW of external supply available to charge the battery, however the accepted charging power is throttled by the battery to as little as 26 kW.
    - As the charging power is throttled, the battery terminal current decreases accordingly, hence less pump power is required and there are lower internal losses. As a result, the battery efficiency increases as can be seen by the decreasing discrepancy between before and after charging power.

- The battery will stop charging when it reaches a SOC of 80% as this is the upper SOC limit.
- The total energy input received by the battery over this period was 500 kWh, whereas the net energy received and stored into battery was 420 kWh. This corresponds to a charging efficiency of 84%

- At time t = 310 min to t = 359 min:
  - There is still an available 300 kW of external supply available, however as the battery has reached its maximum SOC, it cannot charge any further. The battery remains on standby until there is a power demand requiring the battery to discharge.

During the discharge phase:

- At time t = 360 min to t = 505 min:
  - The battery is discharging a net power of 300 kW to meet the 300 kW demand; however, due to internal losses and the pump power demand, the total discharge power of the battery corresponds 335 to 377 kWh.
  - As the battery SOC decreases, so does the discharging efficiency of the battery. Hence why the difference between the before loss and after loss discharge power increases.
  - The battery delivers a net energy 725 kWh to the consumer; however, due to losses and pump power consumption, the total power used by the battery is 840 kWh. This corresponds to a discharge efficiency of 86%.

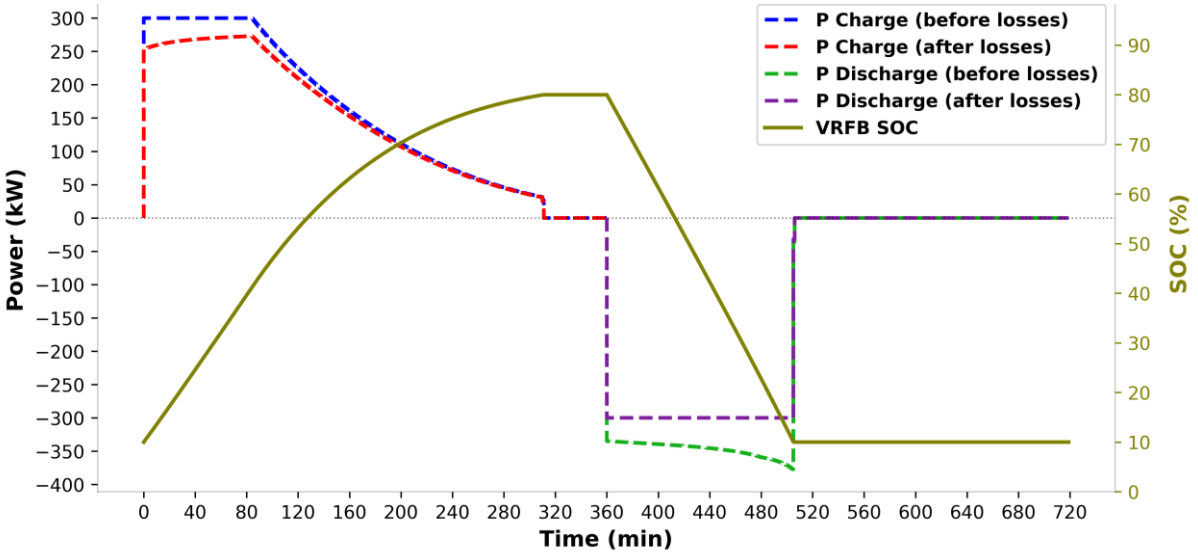

Figure 3.5. Example of a model simulation for a 300 kW / 1200 kWh VRFB showing battery power and SOC at 1 minute time-steps

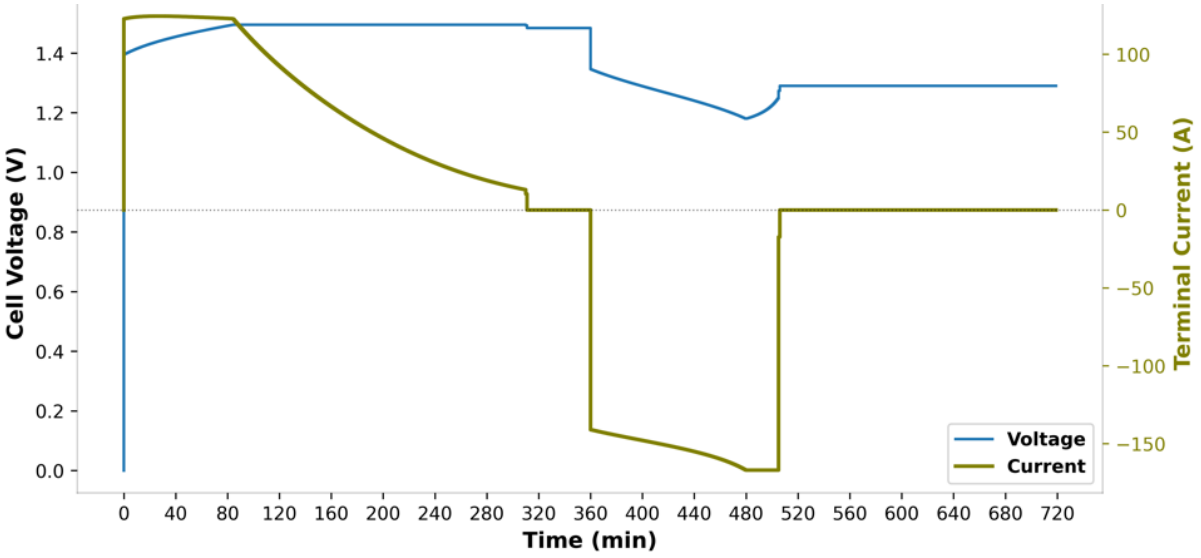

Figure 3.6 Example of a model simulation for a 300 kW / 1200 kWh VRFB showing battery cell voltage and terminal current at 1 minute time-steps

3.2.2.2. VRFB Model Validation

The supplier provided battery power measurements for a charge and discharge cycle of a 15 kW / 125 kWh VRFB system as shown in Figure 3.8, to validate the simulation model. The measurements were obtained by charging the system from 10 – 80% with an available AC charging supply of 18.6 kW, and then subsequently discharging back to 10% SOC at net output of 14.6 kW. The measurements also show the DC charging power which corresponds to the battery terminal power; this is the input power net of pump power consumption (during charging) or output discharging power plus pump consumption, as indicated by the diagram in Figure 3.7. The supplier indicated that the pump power & auxiliary consumption can be assumed as a constant 2 kW during the charge/discharge cycle, and therefore battery terminal power (or DC power) corresponds to 16.6 kW during charging and discharging.

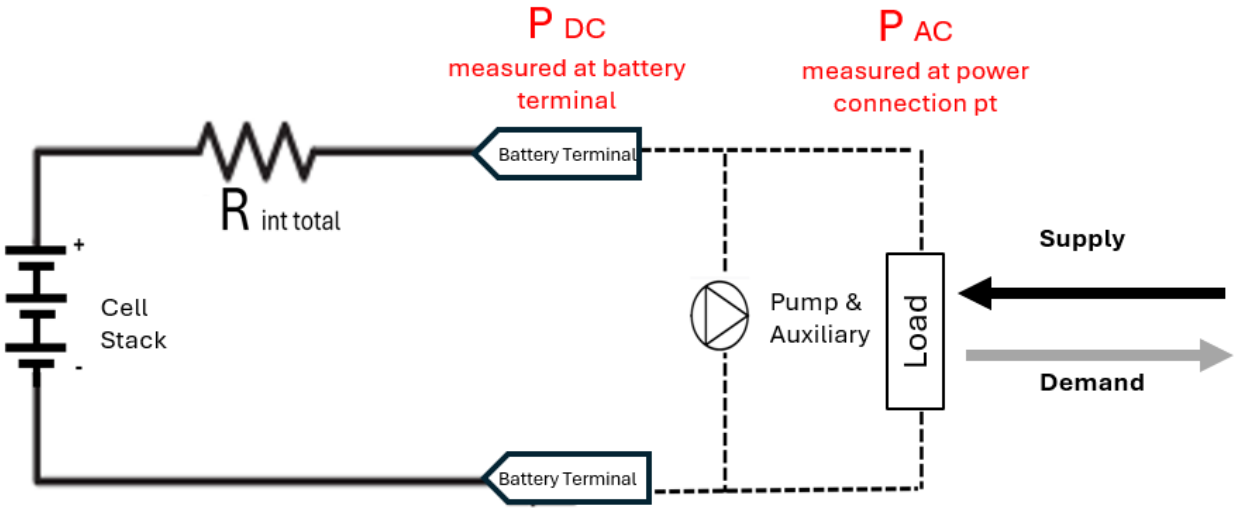

Figure 3.7 Equivalent circuit model of a VRFB indicating the location of the DC and AC power measurements.

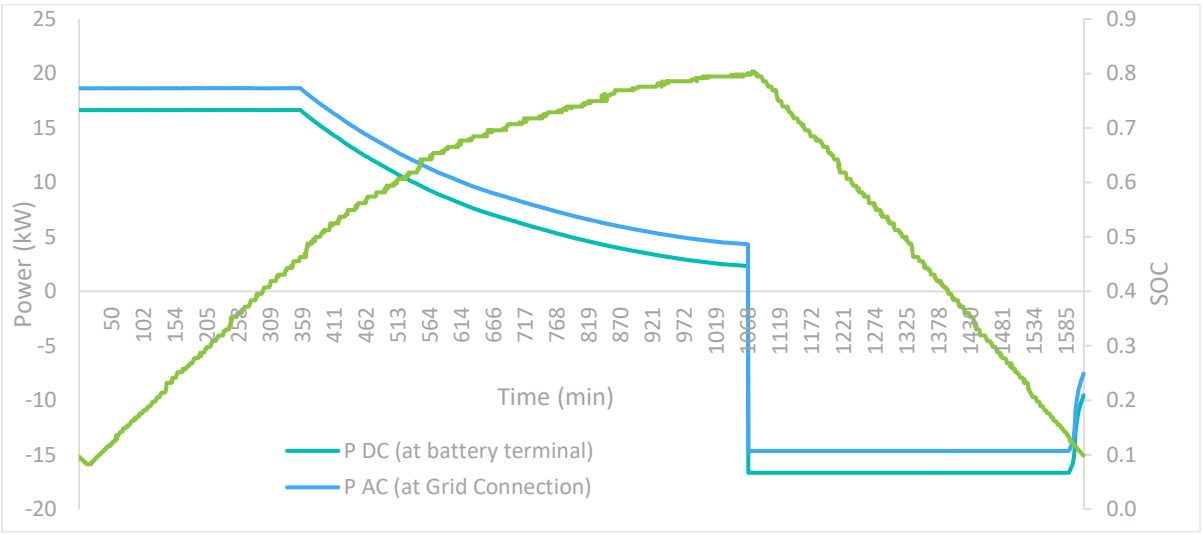

Figure 3.8 Supplier provided characteristic curve for battery power and SOC during a charge and discharge cycle for a 15 kW / 125 kWh VRFB.

Validation of the VRFB model was carried out by simulating a charge and discharge cycle for 15 kW / 125 kWh storage system and by comparing the results to the provided experimental measurements. The parameters used to model the VRFB are listed below in Table 3-2. Although the nameplate storage capacity states 125 kWh, this is based on the net discharging power a consumer can receive when discharging from 80% to 10% SOC. The total stored energy, based on the electrolyte volume and vanadium ion concentration, is approximately 237 kWh. The developed VRFB model considers the total energy storage capacity, and this is noted in Table 3-2.

For simplicity, the simulation omitted the power consumption of the pump and auxiliaries and the VRFB was charged and discharged at 16.6 kW. The simulation first modelled a battery charging operation from 10% to 80% SOC with a constant available charging power of 16.6 kW. Once charged to 80% SOC, the battery was discharged back to 10% SOC, with a requested discharging power of 16.6 kW. The simulation results were compared with the experimental results and are displayed in Figure 3.9 and Figure 3.10 below.

Table 3-2. Supplier provided data for the VRFB

Parameter	Symbol	Value
Net Energy Storage Capacity[1]	$E_{net\ stored}$	125 kWh
Total Energy Storage Capacity[2]	E_{Stored}	237 kWh
Total Electrolyte Volume	$V_{electrolyte}$	7,900 L
Vanadium concentration	$C_{v\ total}$	1.6 mol/L
Area specific internal resistance	r_m	1.4 Ω cm^2 (Charge) 1.6 Ω cm^2 (Discharge)
State of charge limits	$SOC_{RFB\ min} - SOC_{RFB\ max}$	10 – 80%
Upper cell voltage limit during charging	$v_{cell\ max}$	1.5 V

[1] Net energy that the consumer can realize, after considering battery efficiency and SOC limits

[2] Total energy stored in the tanks based on electrolyte volume and electrolyte concentration

In general, there is good agreement between the simulation and experimental results; however, several minor discrepancies are noted as described in the points below. Though errors are present, the level of error is not significant enough to affect our subsequent long-term analysis to be carried out in task D2.3 and therefore is deemed acceptable. The discrepancies are as follows:

- During discharge, the simulation results show a constant battery terminal power at -16.6 kW for the entire cycle (between t = 1070 minutes to t = 1610 minutes). The experimental results are similar, however at 1590 minutes, the battery terminal power starts to ramp down to -10 kW at t = 1610, before completing the discharge cycle. These effects are due to the current limit and lower voltage limit of the inverter used in the experimental test setup, which has not been accounted for in the simulation model.
- The SOC profile for the experimental results lags the simulation results; however, at a closer inspection the experimental SOC profile lags behind the experimental power results as well. Looking at the experimental battery power profile, the charging cycle ends at t = 1070 minutes and discharge occurs. The experimental continues to rise and reaches its maximum SOC of 80% at t = 1084 minutes. This is also evident at the beginning of the charge cycle at t = 0 minutes. At this time, the SOC is decreasing from a previous discharge cycle until it reaches 8.5% at t = 17 minutes. The reason for this lag between experimental SOC measurements and experimental battery power could be explained due to the delay associated with the transport and mixing of the different vanadium ion species from the reaction cell to the tank. Additionally, method of measuring the SOC could also contribute to this. For example, if the SOC is based on the measured concentration of different vanadium ion species via spectroscopy, a delay would be expected as the ions are transferred from the cell stack to the location of measurement.

Finally, the validation results were unable to confirm whether the VRFB degradation was accurately modelled. The simulation and experimental results only accounted for a single charge and discharge cycle, while observing meaningful degradation effects would require

hundreds to thousands of cycles. To incorporate degradation effects into the validation study, long-term experimental data over multiple battery cycles would be necessary, but such data was unavailable. In the upcoming tasks for deliverable D2.3, the VRFB will be simulated over a year-long period, and it is anticipated that degradation effects will play a significant role in the results. Therefore, the model validation is currently limited to short-term battery behaviour, and as such, long-term degradation effects are not fully represented.

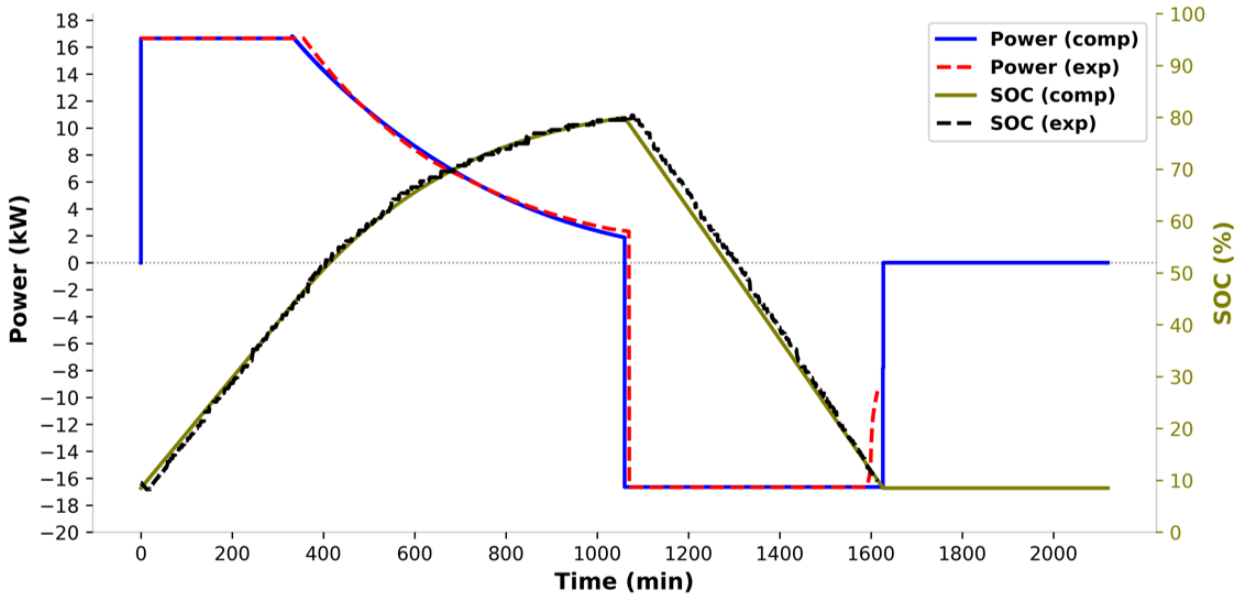

Figure 3.9 Measurement and simulated battery power and SOC results for a VRFB 15 kW /125 kWh charge cycle and discharge cycle.

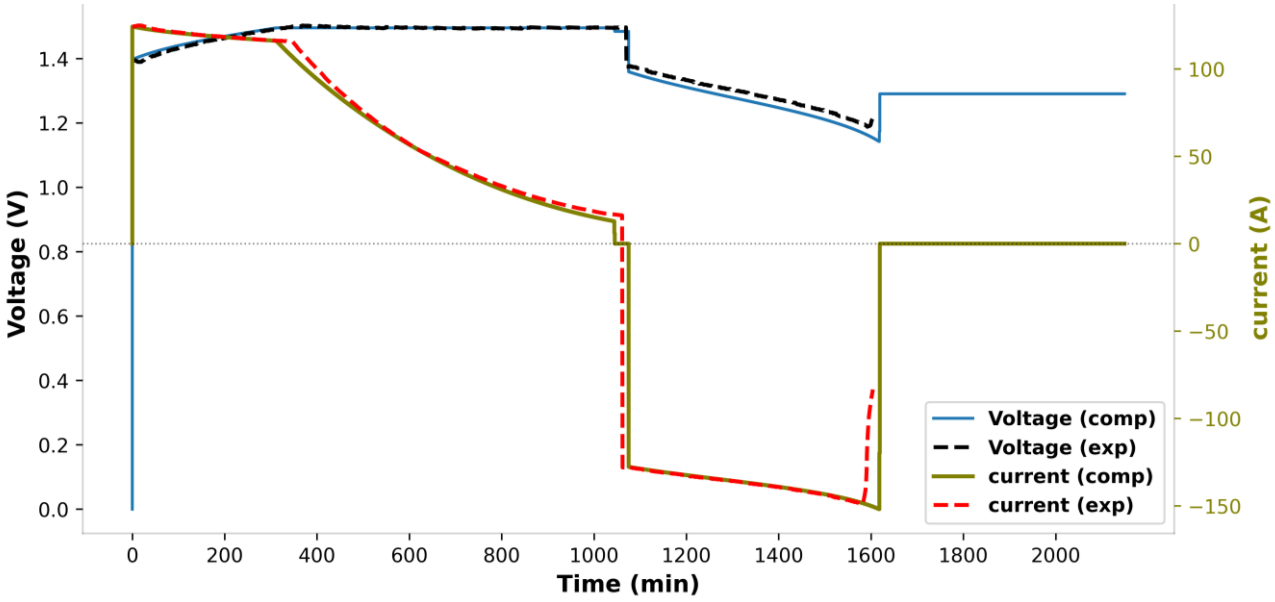

Figure 3.10 Measurement and simulated battery current and cell voltage results for a VRFB 15 kW /125 kWh charge cycle and discharge cycle.

3.3. MODEL OF SALT-BASED BATTERY

This section provides a comprehensive overview of the equations governing the power and thermal dynamics of a salt-based battery, specifically a sodium-nickel chloride ($NaNiCl_2$) battery. The model aims to capture the critical aspects of the battery's internal operation and external interactions to enable accurate performance predictions and thermal management.

3.3.1. Mathematical Model of the Salt-Based Battery

3.3.1.1. Power Model Equations

The power balance equations describe the flow of electrical power within the battery during charging and discharging operations.

During charging and discharging, the power balance can be expressed as (32) and (33), respectively:

$$P_{NaNiCl2\ Internal} = P_{NaNiCl2\ input} - P_{NaNiCl2\ loss} \quad (32)$$

$$P_{NaNiCl2\ Internal} = P_{NaNiCl2\ output} + P_{NaNiCl2\ loss} \quad (33)$$

The energy charged or discharged by the battery can be calculated by (34) integrating the internal power over time:

$$E_{NaNiCl2} = \int P_{NaNiCl2\ internal}\, dt \quad (34)$$

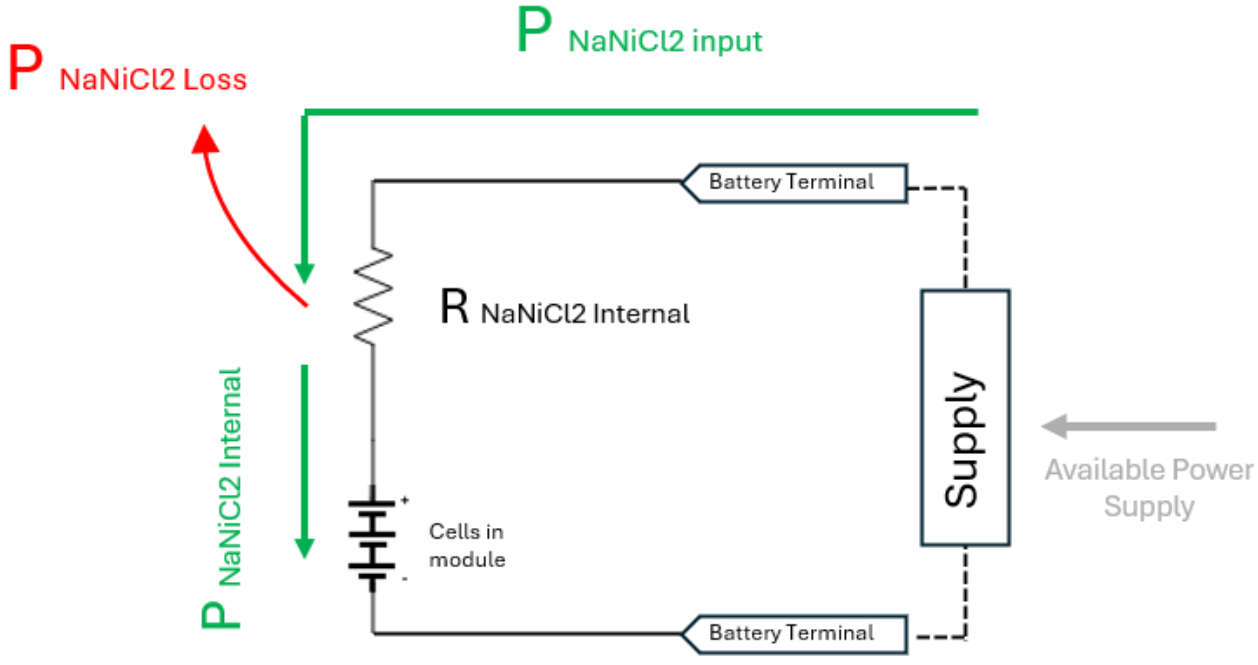

Figure 3.11. Salt-based battery equivalent circuit diagram illustrating the charging cycle

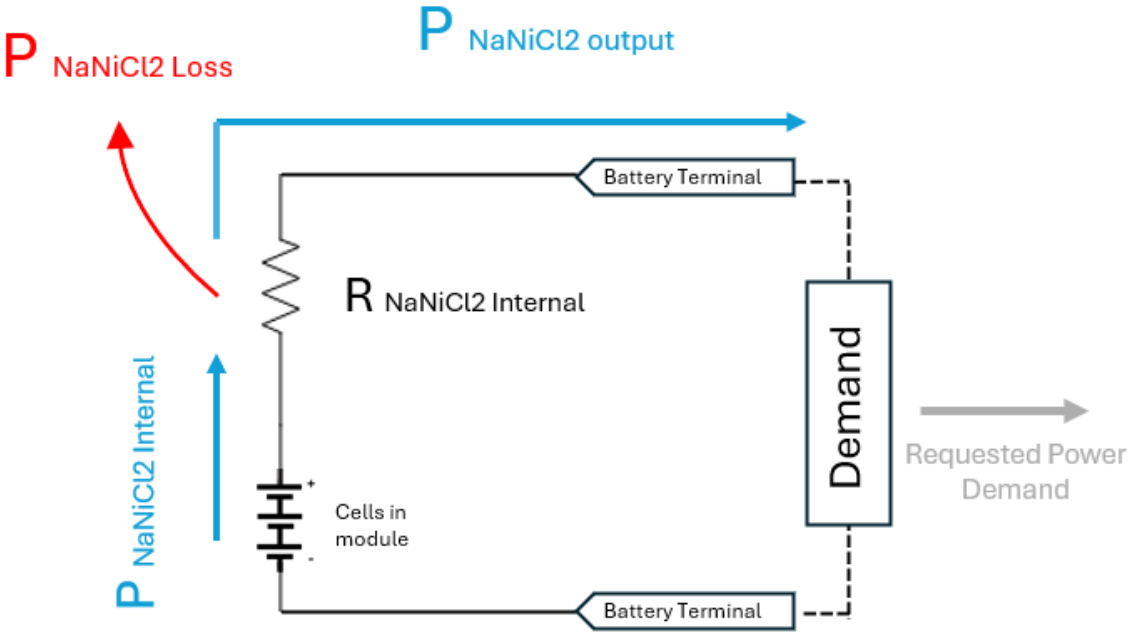

Figure 3.12. Salt-based battery equivalent circuit diagram illustrating the discharge cycle

Where:

Internal power received by the battery cells:

$$P_{NaNiCl2\ Internal} = I_{NaNiCl2}\, v_{OCV\ mod} \quad (35)$$

Ohmic losses due to battery internal resistance:

$$P_{NaNiCl2\ loss} = I_{NaNiCl2}\, R_{NaNiCl2\ mod} \quad (36)$$

Known or measured input charging power:

$$P_{NaNiCl2\ input} = Known \quad (37)$$

Known or measured output discharging power:

$$P_{NaNiCl2\ Output} = Known \quad (38)$$

Battery module open circuit voltage (see Table 3-3 for parameter description):

$$v_{OCV\ mod} = N_{NaNiCl2\ s}\, E_{OCV\ NaNiCl2} \quad (39)$$

Battery module internal resistance (see Table 3-3 for parameter description):

$$R_{NaNiCl2\ mod} = \frac{N_{NaNiCl2\ s}}{N_{NaNiCl2\ p}} R_{NaNiCl2\ Cell} \quad (40)$$

Solving the power balance equations for the battery terminal current, $I_{NaNiCl2}$, results in quadratic equations for both charging and discharging operations as shown in (41) and (42):

$$-I^2{}_{NaNiCl2}\, R_{NaNiCl2\ mod} - I_{NaNiCl2}\, v_{OCV\ mod} + P_{NaNiCl2\ input} = 0 \quad (41)$$

$$I^2{}_{NaNiCl2}\, R_{NaNiCl2\ mod} - I_{NaNiCl2}\, v_{OCV\ mod} + P_{NaNiCl2\ output} = 0 \quad (42)$$

Battery degradation was also considered for the salt-based battery model, which causes a reduction of the battery's total energy storage capacity due to usage. A simple linear degradation model was used, corresponding to a capacity reduction of 0.0046% per cycle, based on a previous study [56]. This corresponds to a reduced capacity of ~80% after 4,500 cycles and aligns with ZEBRA battery specifications [23]. The reduced energy storage capacity can be calculated with equation (43) below.

$$E_{stored\ NaNiCl2}(cyc = n_{cyc}) = E_{stored\ NaNiCl2}(cyc = 0) * \left[100\% - D_{NaNiCl2}\, n_{cyc}\right] \quad (43)$$

The parameters used for to create the salt-based battery simulation model are summarised in Table 3-3 below. These are based on a 9.6 kWh battery module comprised of 100 ZEBRA battery cells in series.

Table 3-3 Salt-based battery module parameters and variables used for simulation model

Parameter	Symbol	Value
Degradation rate	$D_{NaNiCl2}$	0.0046% / Cycle [56]
Module Storage Capacity	$E_{stored\ NaNiCl2}$	9.6 kWh
Cell open circuit voltage	$E_{OCV\ NaNiCl2}$	A function of SOC, and charging. Based on published experimental results [57]
No. of cells in series	$N_{NaNiCl2\ s}$	100
No. of cells in parallel	$N_{NaNiCl2\ p}$	1
No. of charge/discharge cycles	n_{cyc}	-
Internal resistance of cell or module	$R_{NaNiCl2\ i}$	A function of SOC, charging mode and C-rate. Based on published experimental results [57]

3.3.1.2. Battery Thermal Model Equations

The thermal model equations describe the heat transfer processes within the battery and its interaction with the surrounding environment that represented by equations (44) to (48). Equation (44) is the total heat loss or gain of the battery during charging, (45) is the total heat loss or gain of the battery during discharging, (46) is the total heat loss/gain of the battery during standby, (47) is the heat gain during warm-up and (48) is the change in temperature of the battery.

Heat gain or loss during charging:

$$\dot{Q}_{Total} = \dot{Q}_{Ohmic} - \dot{Q}_{Entropic} - \dot{Q}_{Ambient} \quad (44)$$

Heat gain or loss during discharging:

$$\dot{Q}_{Total} = \dot{Q}_{Ohmic} + \dot{Q}_{Entropic} - \dot{Q}_{Ambient} \quad (45)$$

Heat gain or loss during battery standby:

$$\dot{Q}_{Total} = -\dot{Q}_{ambient} \quad (46)$$

Heat gain during battery warm-up:

$$\dot{Q}_{Total} = \dot{Q}_{Heater} - \dot{Q}_{Ambient} \quad (47)$$

Change in battery temperature:

$$T_{battery} = \frac{\dot{Q}_{Total}}{mC_p\Delta T_{battery}}\Delta t \quad (48)$$

The heating terms are summarized in equations (49) and (52) and there effects are illustrated in Figure 3.13 below. The other components and parameters related to these heating terms are summarized by equations (53) to (55) and Table 3-4.

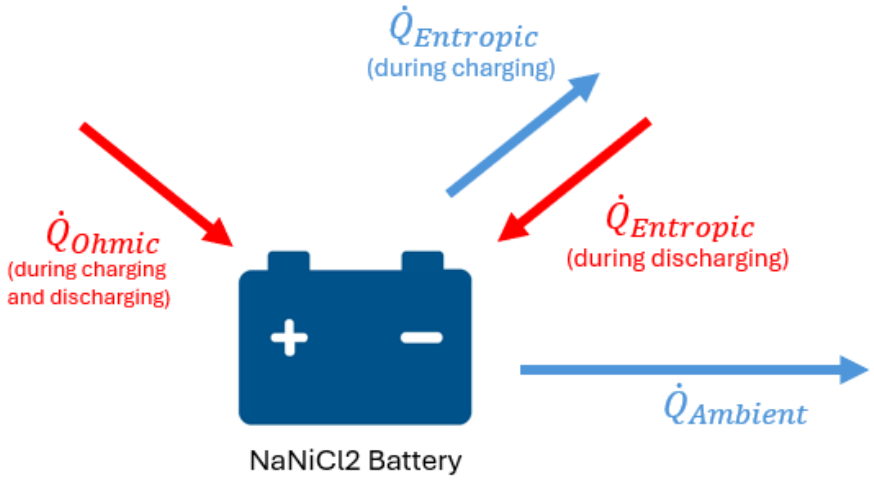

Figure 3.13. Diagram illustrating the heating of the salt-based battery during different modes

Ohmic heating causes the battery to heat during charging and discharging operations due to the irreversible effects of battery internal resistance. This is given by:

$$\dot{Q}_{ohmic} = I^2_{NaNiCl2}\, R_{NaNiCl2\ total} \tag{49}$$

Entropic heating is the reversible heating effects of the internal battery reaction. It will cause the battery to cool-down during charging due to the internal endothermic reaction. During discharging, it will cause the battery to heat up due the internal exothermic reaction. This can be determined by:

$$\dot{Q}_{Entropic} = \frac{dU}{dT} I_{NaNiCl2}\, T_{battery} \tag{50}$$

Ambient heating effects will always cause the battery to cool-down, as it is assumed that the battery temperature will always be greater or equal to the temperature of its surroundings. This can be determined by:

$$\dot{Q}_{ambient} = \frac{T_{battery} - T_{air}}{R_{Thermal\ total}} \tag{51}$$

Heating due to the integrated heater, $\dot{Q}_{Heater}$, will warm up the battery to keep its temperature above the minimum operating temperature setpoint, and is as per below:

$$\dot{Q}_{Heater} \leq 390\ W \tag{52}$$

Total thermal resistance of air and battery insulation:

$$R_{Thermal\,total} = R_{Thermal,\ insulation} + R_{Thermal,\ air} \quad (53)$$

Thermal resistance of the insulation:

$$R_{Thermal,\ insulation} = \frac{d}{A\,k} \quad (54)$$

Thermal resistance due to free air convection:

$$R_{Thermal,\ Air} = \frac{1}{A\,h} \quad (55)$$

Table 3-4: Parameters used in equations (44) - (55).

Parameter	Symbol	Value	Comments
Total mass of cells in modelled module	m	69.5 kg	Based on the mass of 1 cell [58], with 100 cells in the module.
Ave. heat capacity of the cells	C_p	870 j/kg C	Determined via curve fitting using the supplier provided warm-up and cool-down curves. This is explained in detail in subsection 3.3.1.3 below.
Entropic heat coefficient for the cells	$\frac{dU}{dT}$	2.16 x 10^{-4} V/K	Typical for ZEBRA batteries [59] [60]
Simulation time step	Δt	-	-
Ambient air temperature of surroundings	T_{air}	25 °C	Assumed
Minimum operating temperature of the battery	$T_{bat\,min}$	265 °C	-
Maximum operating temperature of the battery	$T_{bat\,max}$	350 °C	-
Thermal resistance	$R_{Thermal\,i}$	-	Where i represents air, insulation or total.
Battery Insulation thickness	d	30-50 mm	Based on supplier provided information.
External surface area of the insulation	A	0.8 - 1 m^2	Determined based on module's cell arrangement and insulation thickness.
Thermal conductivity of insulation	k	0.03 – 0.05 W/m K	Typical for fumed silica [61]

Parameter	Symbol	Value	Comments
Convective heat coefficient of free air	h	100 W/m^2 K	Assumed

3.3.1.3. Heat Capacity Estimation for the Salt-Based Battery

The heat capacity of the cells, C_p, is an important parameter for the thermal components of the salt-based battery model, as shown in the thermal equations above. This is not a parameter that can be easily and accurately calculated as the ZEBRA battery cells are comprised of various metals, salts and ceramics at unknown quantities. An average heat capacity value was estimated via curve-fitting using the temperature profiles for the battery warm-up and cool-down phases of operation. These profiles were obtained using the data from the supplier specification for the battery module and are shown in Figure 3.15 and Figure 3.15. Using equations (46) to (48), warm-up and cool-down temperature profiles were simulated, based on the ambient air temperatures and battery temperatures summarised in Table 3-5. The heat capacity was iteratively adjusted until the simulated temperature profiles for both phases matched their respective supplier-provided profiles. The most accurate results occurred for a heat capacity value of 870 j/kg °C and these are shown Figure 3.16 and Figure 3.17.

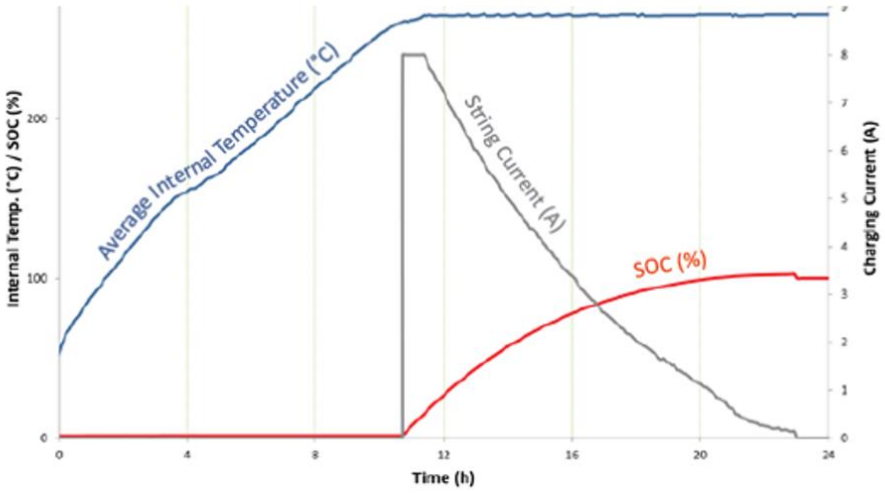

Figure 3.14 Battery module temperature and SOC for warm- up. From supplier datasheet [62]

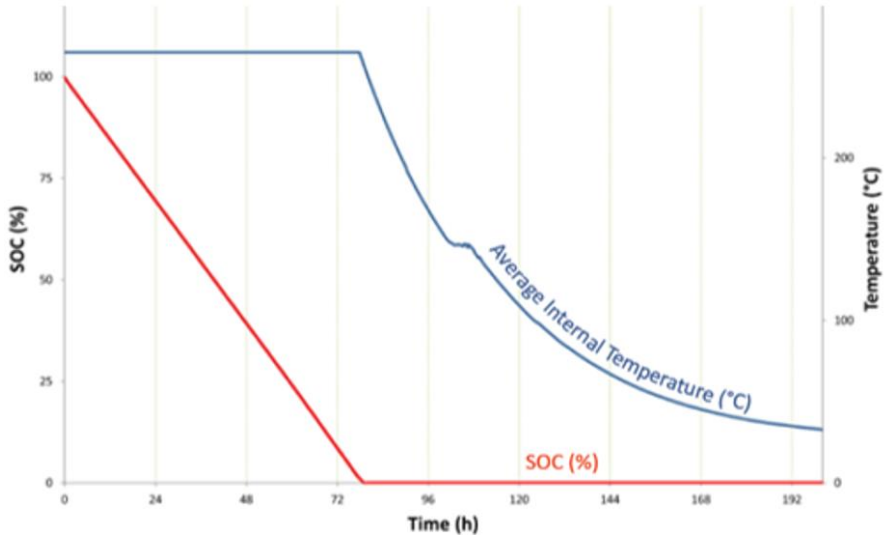

Figure 3.15. Battery module temperature and SOC profiles during cool-down. From supplier datasheet [62]

Table 3-5 Initial and final battery temperature and ambient air temperature used for simulation

Parameter	Warm-Up Phase	Cool-Down Phase
Initial Battery Temperature	50 °C	265 °C
Final Battery Temperature	265 °C	25 °C
Ambient Temperature	50 °C	25 °C

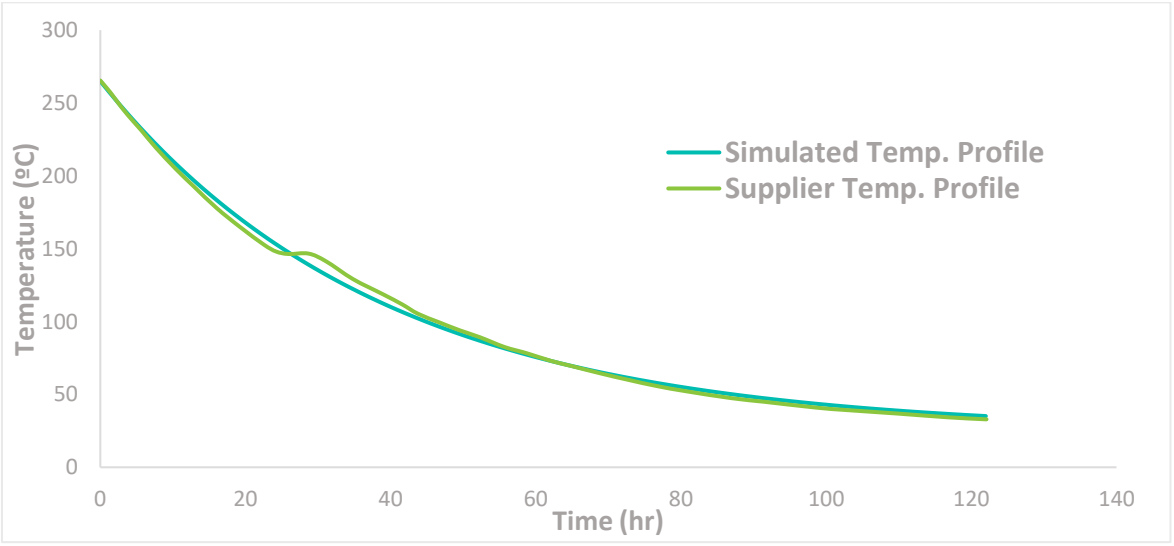

Figure 3.16 Simulated temperature profile using heat capacity of 870 j/kg °C vs supplier provided temperature profile for the cool – down phase [62].

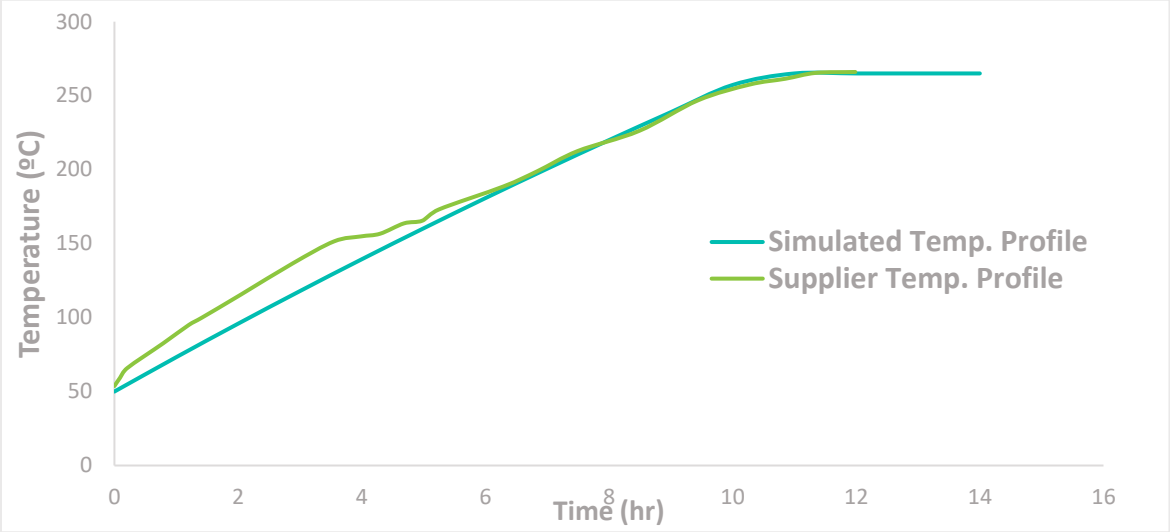

Figure 3.17 Simulated temperature profile using heat capacity of 870 j/kg °C vs supplier provided temperature profile for the warm-up phase [62]

3.3.2. Salt-Based Battery Model Results

3.3.2.1. Salt-Based Battery Model Demonstration

A charging/discharging cycle simulation was carried out to demonstrate the salt-based battery model. The simulation was carried out for a 9.6 kWh battery module over a 14-hour period at 1 minute time-steps. The initial conditions of the battery were an internal temperature of 270 °C and a SOC of 0%. For the first 500 minutes, an external power supply of 3 kW was simulated to charge the battery to 100%, followed by a subsequent power demand at 3 kW to fully discharge the battery. Note that, SOC limits are sometimes imposed on salt-based batteries depending on use case and manufacturer, to promote longevity; however, in this case we have allowed for operation within 0- 100% to observe the behaviour at extreme SOC level. The simulation results can be seen in Figure 3.18 to Figure 3.20 and the following observations are made:

- At time t = 0 min to t=126 min:
    - The battery is charging with a constant current scheme.
    - Although there is an external supply of 3 kW, the battery only charges at 2.7 kW due to the current limits of the constant current scheme.
    - Due to the internal resistance of the battery, the net received power by the battery is 2.6 kW.
    - The battery has a constant heat dissipation of 100 W, causing minor cooling of the battery. However, about 20 minutes into the charging cycle, the internal resistance of the battery, which changes with SOC, increases causing ohmic heating of the battery. The battery therefore maintains a relatively stable temperature in this time frame.

- At time t = 126 min to t = 192 min:
    - Once the battery terminal voltage reaches 274 V, it charges at constant voltage. Current and charging power decrease accordingly.
    - Due to the decreasing current, the losses due to internal resistance also decrease, hence battery charges at a higher efficiency than previously. This also reduces the ohmic heating of the battery.
- At time t = 192 min to t = 546 min:
    - Once the battery reaches a SOC of 80%, the constant voltage charging limit reduces to 267 V. The current and charging power decrease accordingly.
    - The decreasing current causes even lower internal losses, increasing the charging efficiency even further.
    - Lower internal losses correspond to significantly lower ohmic heating of the battery. The passive cooling due to the ambient temperature causes the battery temperature to reach its lower set-point of 265 °C. To prevent cooling below this limit, the battery uses some of the external supply to power its integrated heater at 100 W. Because the battery is charging at < 1 kW, and the available supply is 3 kW, there is enough surplus to power the heater.
- At time t = 546 min to t = 600 min:
    - Battery has reached 100% SOC and stopped charging.
    - There is still an external power supply of 3 kW available, and the battery uses 100 W of this to maintain its temperature above 265 °C.
- At time t = 600 min to t = 772 min:
    - There is no longer external power supply, and instead there is a power demand of 3 kW. The battery commences discharging to provide the 3 kW power supply.
    - The battery internal resistance changes with both C-rate and SOC, therefore there is a varying discrepancy between net and total power discharge. The total discharge of power varies between 3.2 to 3.7 kW, corresponding to a loss of 200 to 700 W.
    - The ohmic heating due to internal losses means that using the battery heater is no longer necessary. The battery temperature increases up to 302 °C due to the increasing ohmic heating effects.
    - Once the battery reaches a SOC of 0%, it can no longer supply the demand.
- At time t= 772 min:
    - The battery is completely discharged. The battery starts to cool due to the ambient temperature.

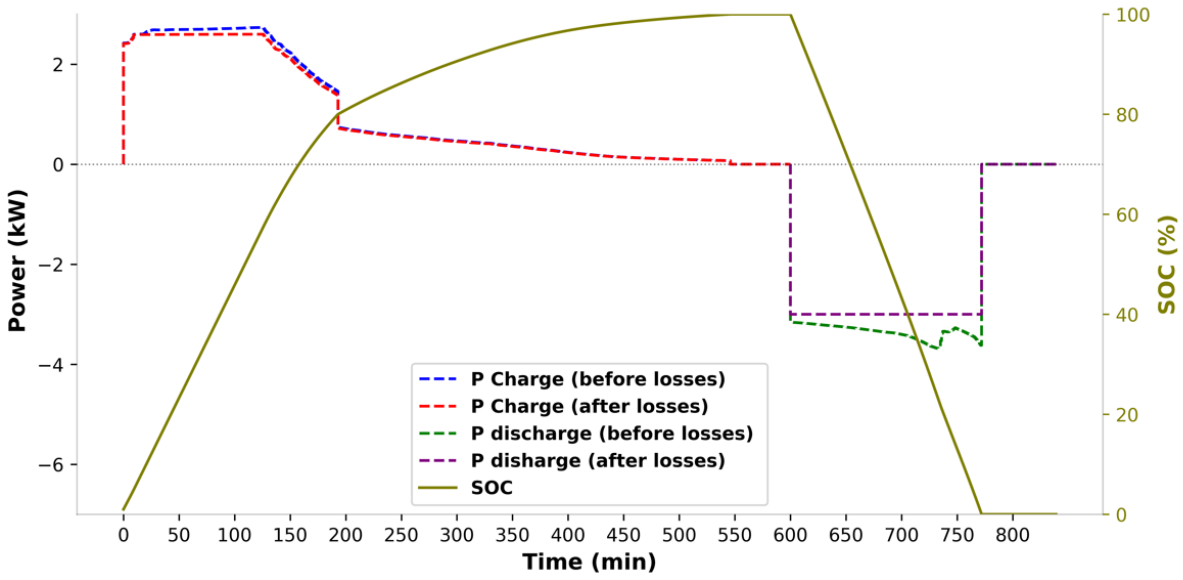

Figure 3.18 Example of a model simulation for a charge and discharge cycle of a 9.6 kWh salt-based battery showing battery power and SOC at 1 minute time-steps

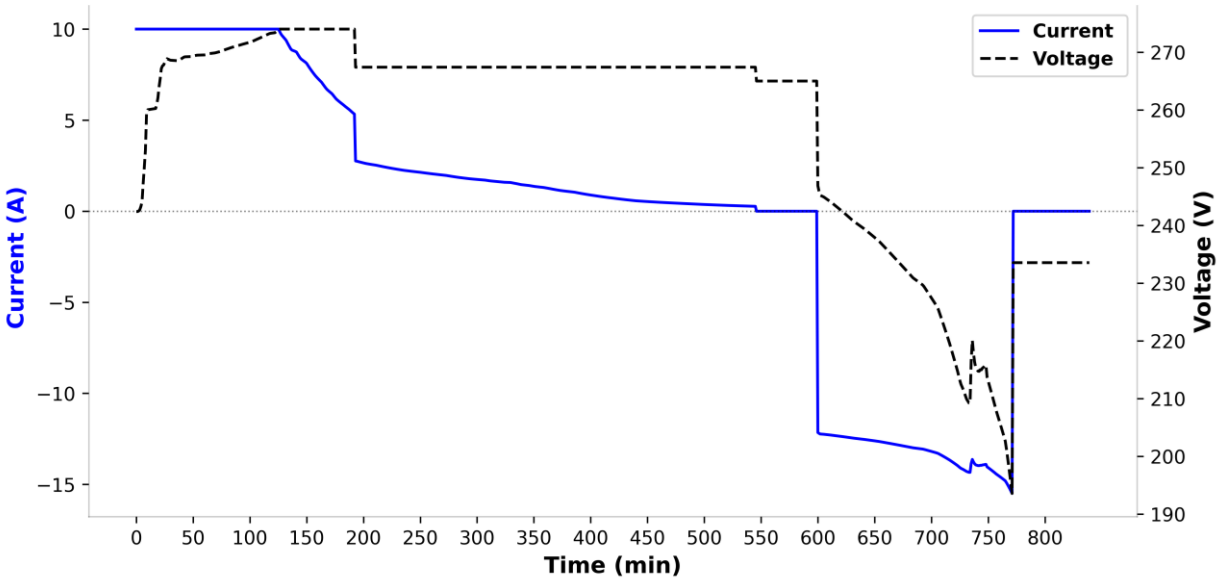

Figure 3.19 Example of a model simulation for a charge and discharge cycle of a 9.6 kWh salt-based battery showing battery terminal current and voltage at 1 minute time-steps

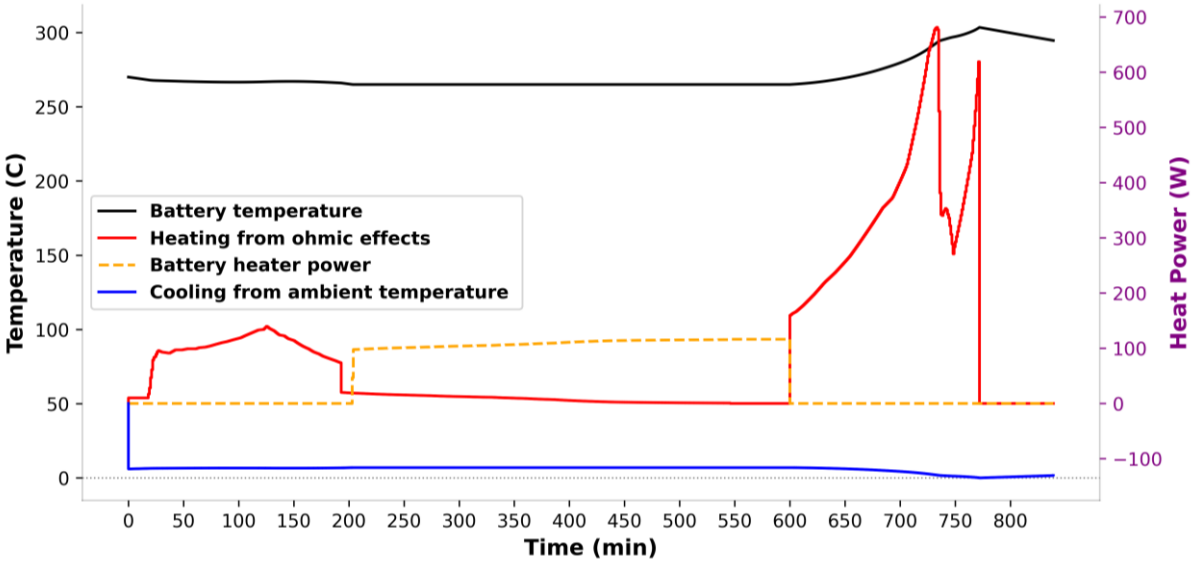

Figure 3.20 Example of a model simulation for a charge and discharge cycle of a 9.6 kWh salt-based battery showing battery temperature and heating power profiles due to ohmic effects, battery heater and passive cooling.

3.3.2.2. Salt-Based Battery Model Validation

The supplier provided real-time measurements of different performance metrics for the different operating modes of the 9.6 kWh salt-based battery module. This data was used to compare and validate the performance of the simulation model. Measurements were provided for the following battery modes:

- Warm-up and Standby
  - Battery has an initial temperature of 35 °C.
  - An available external power supply powers the battery's integrated heater to warm up the battery to its minimum temperature set point of 265 °C.
  - The battery is now on standby. The heater continues to operate to maintain the temperature at 265 °C and is powered by the external power source.
- Self-Discharge and Cool-Down
  - The battery is on standby and is at its minimum temperature setpoint (265 °C). There is no available external power to operate the battery heater.
  - The battery discharges itself to power its integrated heater and maintains its temperature at the minimum setpoint.
  - Once the battery SOC reaches 0%, it can no longer power its integrated heater. The battery will begin to cool.
- Charge and Discharge Cycling
  - The battery charges when its SOC is below 100%, there is an external power supply available, and its temperature is between 265 and 350 °C.
  - The battery discharges when its SOC is above 0%, there is an external power demand, and its temperature is 265 and 350 °C.

Warm-Up and Standby Phase Validation

A simulation for the warm-up phase was carried out and the results were compared to the measurements to validate the model under this mode of operation. The results are shown in Figure 3.21 and Figure 3.22. Looking at the measured data, the heater provides intermittent periods of heating between 180 – 340 W and it is not yet clear to FBK how the BMS decides the level and duration of heating. Currently, FBK are waiting for clarification from the supplier about this; however, for the purpose of validation, the warm-up simulation was carried out by replicating the exact same heating power input as per the measured data. For standby, however, the simulation model used constant heating to maintain 265 °C, whereas the tested battery used short bursts of heating.

The measured and simulated battery temperature profiles show good agreement with some minor discrepancies. In the first 10 hours of warm-up, the simulation results show lower battery temperatures compared to the experimental results; however, after 10 hours this point, the simulation results match the measurements. This good agreement indicates that the thermal parameters of the battery model have sufficient accuracy, however, to complete the validation, it would be beneficial to understand the heating control logic of the battery during this phase.

During the standby phase, the measured temperature tends to fluctuate due to the intermittent bursts of heater activity corresponding to 210 W and 340 W of heating. The simulation model differs in this aspect as it maintains a constant temperature a the minimum setpoint of 265 °C by applying a constant heating of 100 W. As mentioned previously, it would be beneficial to understand this heating logic and updated the model accordingly to improve accuracy.

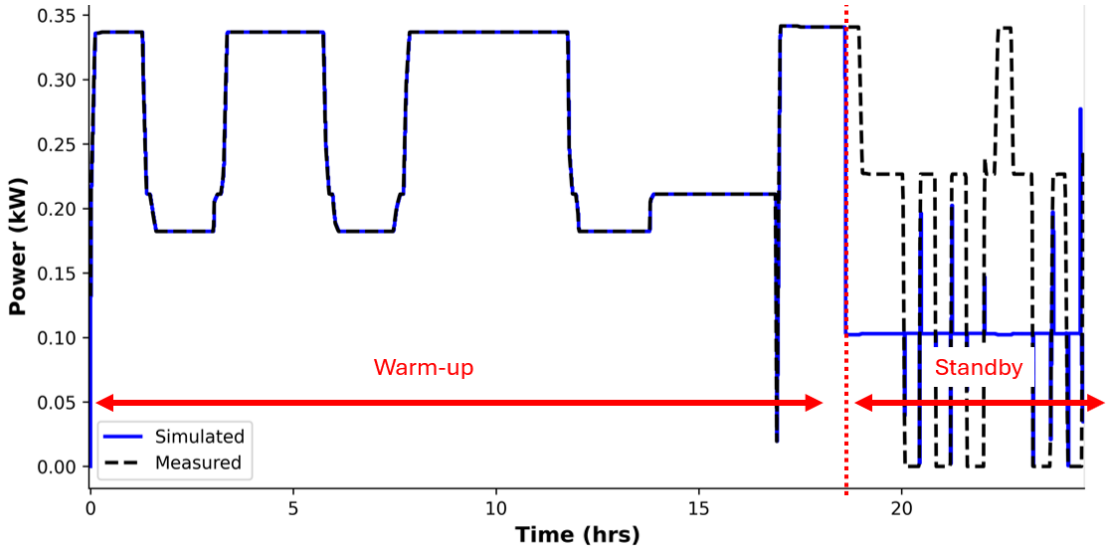

Figure 3.21. Measured and simulated results for battery heating power during the warm-up and standby phase for a 9.6 kWh salt-based battery.

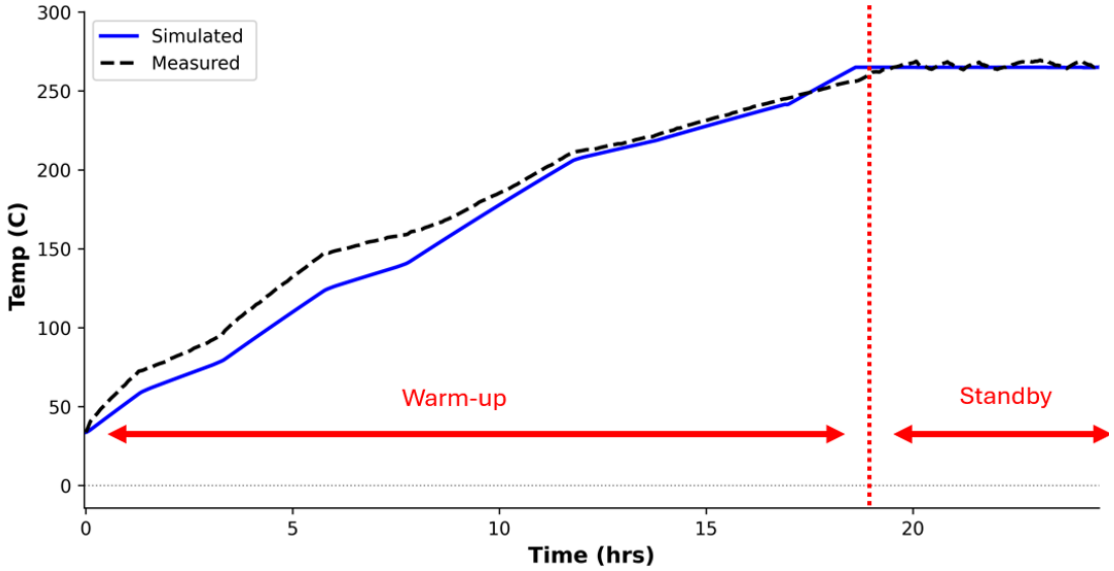

Figure 3.22. Measured and simulated results for battery temperature during the warm-up and standby phase for a salt-based battery.

Self-Discharge and Cool-Down Phase Validation

Figure 3.23 shows the measured and simulation profiles for temperature and SOC during self-discharge and cool-down. There is good agreement between the simulation and experimental results with some minor discrepancies. For example, in the experimental temperature profile, a constant temperature of 150 °C at t = 100 hrs for 3 hours. This can be explained due to the latent heat of fusion of the molten $NaAlCl_4$ salt present in the battery cells, which changes from a liquid to solid phase [63]. These effects were ignored in the simulation model to maintain simplicity. Additionally, the experimental profile discharges quicker than the simulation model, hence the cool-down phases start ~ 4 hours earlier. This discrepancy accounts for about 5% of the time difference when considering the entire 77-hour self-discharge phase and hence it can be deemed acceptable.

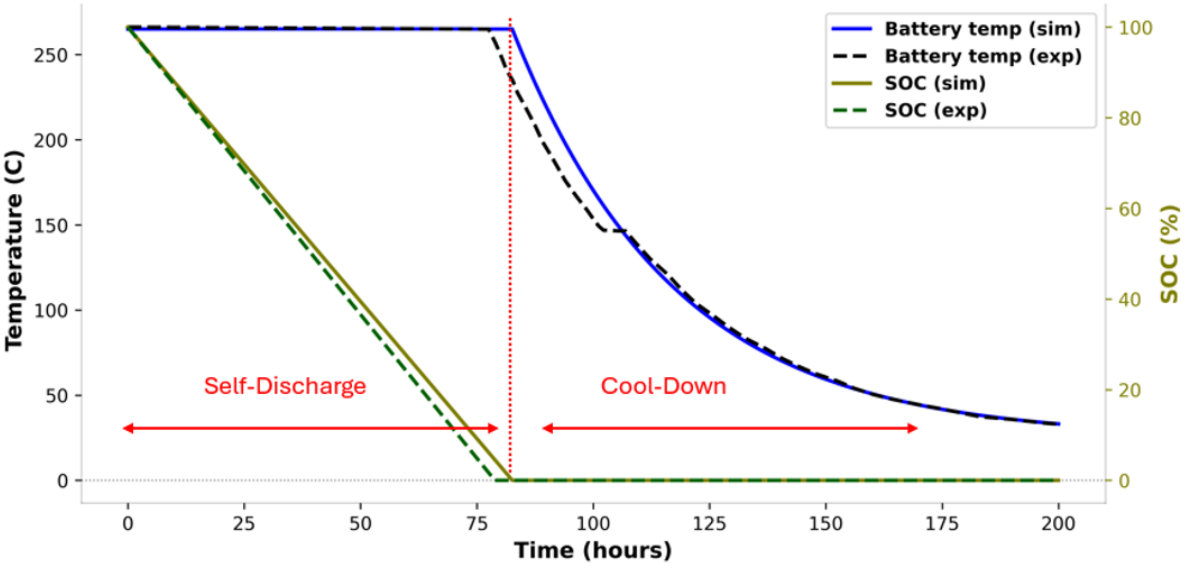

Figure 3.23. Measured and simulated results for the battery temperature and SOC during self-discharge and cool-down phases [62] **for a 9.6 kWh salt-based battery.**

Charge and Discharge Cycling Validation

Various battery measurements were provided for the 9.6 kWh salt-based battery module during several charge & discharge cycles, and these are shown in Figure 3.24a - e. The experimental results show battery performance for 6 partial discharge & charge cycles, with a requested discharge load of ~3 kW and an input charge load of ~2.5 kW. To validate the simulation model for this operating condition, the same charge & discharge cycles were simulated and the corresponding results are also summarized in Figure 3.24a – e below.

By comparing the experimental and simulated results, generally good alignment can be seen between the two, indicating that the simulation model is reasonably accurate. Minor discrepancies occur between battery power, current and voltage, as described in the points below; however, the level of error is not significant enough to affect our subsequent long-term analysis to be carried out in task D2.3 and therefore is deemed acceptable. The discrepancies are as follows:

- Temperature shows the biggest discrepancy. Although it follows the same general profile, the simulated results have shallower peaks than the measured results at the end of each charge and discharge cycle, indicating that the model undergoes experiences less heating and cooling effects. This could be due to the following model limitations or inaccuracies:
    - The battery internal resistance which contributes to joule heating during battery operation, has not been modelled accurately. The internal resistance varies with C-rate, SOC, temperature and operating mode, and is implemented into the battery simulation model as a look-up table, using linear interpolation to extract the appropriate value corresponding to the exact battery operating

condition. There may be limitations with the accuracy of these values used, as they were taken from a published study and not based on supplier-provided parameters.

- Entropic heating, which contributes to battery heating during discharge and cooling during charge, may not be accurate. There is limited information on the entropic heating coefficient for $NaNiCl_2$ batteries and how it may vary with battery operating conditions. A reported value of 2.16 mV/K has been used for both charging and discharging modes [59] [60].
- Heat capacity may not be accurate, which has been approximated as 870 J Kg / K by curve fitting (see sub-section 3.3.1.2).

- The simulation shows slightly lower SOC after each discharge cycle compared to measured values. This might be due to the model having greater losses on the discharge cycle, causing the battery to discharge more energy. This could be due to higher internal resistances in the model, which could also explain why the model experiences greater temperatures at the end of each discharge cycle.
- Hours 10 – 11, when looking at the current and power results, the constant current charging cycle occurs for longer for the simulated model. This could be due to the model starting from a lower initial SOC at the start of the charge (between 8-9 hours), and therefore stays in the CC charging mode for longer until a terminal voltage of 274 V has been reached.

Lastly, the validation results were unable to determine whether the battery's degradation was accurately captured in the model. Similar to the VRFB, the simulation and experimental results for the salt-based battery were based on ~ 6 charge and discharge cycles; however, meaningful degradation can only be observed after hundreds of cycles. To incorporate degradation into the validation, long-term experimental data covering many cycles would be required, but such data was not available. For the next steps in deliverable D2.3, the salt-based battery will be simulated over a long-term period, and it is expected that degradation effects will significantly influence the results. Therefore, the current validation only accounts for short-term behaviour, and long-term degradation effects are not fully considered.

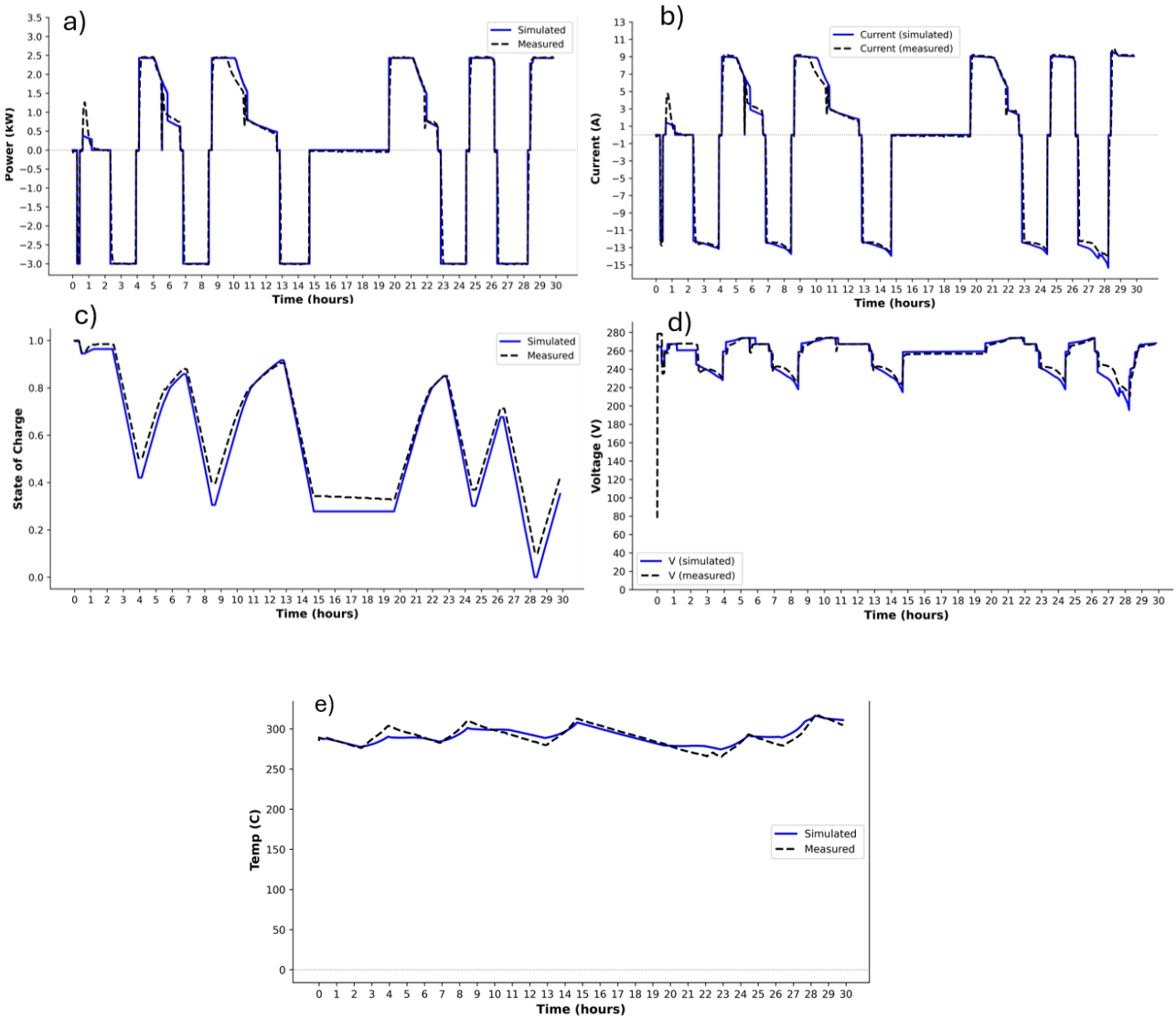

Figure 3.24 Measured and simulated results for the 9.6 kWh salt-based battery during charging and discharging. a) Battery charging and discharging power b) Terminal current c) State of charge d) Terminal voltage e) Battery internal temperature.

3.4. MODEL OF SUPERCAPACITOR

This section outlines the equations that describe the power dynamics of a supercapacitor in order to develop a simulation model for this component. The model is designed to capture the key elements of the supercapacitors' internal functions and its interactions with external systems, allowing for accurate performance forecasting and effective management.

3.4.1. Mathematical Model of the Supercapacitor

A simple supercapacitor model was developed in Python, based on the equivalent circuit model and this is depicted in the diagrams in Figure 3.25 and Figure 3.26. The power flow equations for the charging and discharging cycles are described in equations (56) and (57), respectively. The parameter, C, represents the capacitance and R_{ESR} is the equivalent series

resistance, which corresponds to the SC's internal resistance. During the charging cycle, the supercapacitor will receive a power input, $P_{SC\ input}$ from some external supply. The net power received by the SC, $P_{SC\ Internal}$, is the input power net of its internal losses, $P_{SC\ loss}$. The integral of the internal power, $P_{SC\ Internal}$ is the net energy received and stored by the SC, denoted by E_{SC} and described by equation (58). During discharging, the opposite occurs, where an external load requires some power supply from the SC, denoted by $P_{SC\ output}$. The SC will discharge a total power of $P_{SC\ Internal}$ which accounts for the power demand $P_{SC\ output}$ and any internal losses, $P_{SC\ loss}$. The derivative of $P_{SC\ Internal}$ is the total energy used by the SC to supply the load.

$$P_{SC\ Internal} = P_{SC\ input} - P_{SC\ loss} \quad (56)$$

$$P_{SC\ internal} = P_{SC\ output} + P_{SC\ loss} \quad (57)$$

$$E_{SC} = \int P_{SC\ internal}\, dt \quad (58)$$

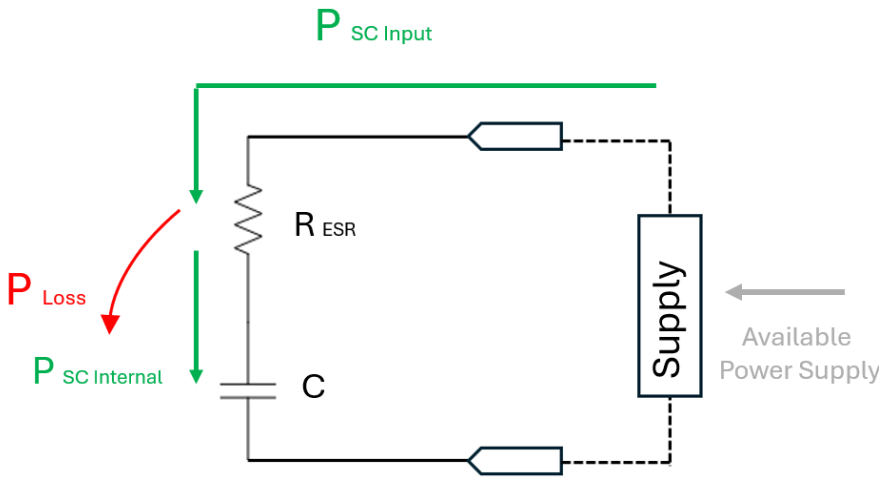

Figure 3.25. Supercapacitor equivalent circuit model illustrating the charging cycle

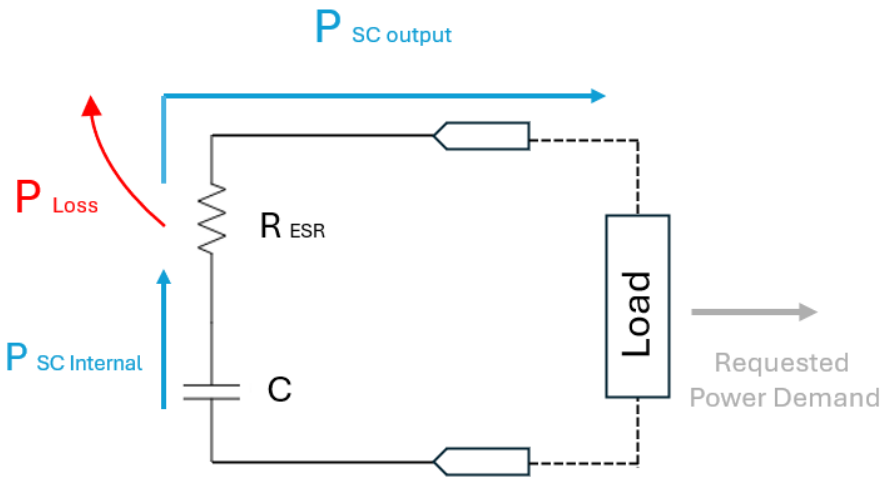

Figure 3.26. Supercapacitor equivalent circuit model illustrating the discharging cycle.

In the application of the model, the known inputs are $P_{SC\ input}$and $P_{SC\ output}$, and it is desired to determine $P_{SC\ Internal}$ for different load profiles. A similar approach to the VRFB and $NaNiCl_2$ model was used to develop a set of quadratic equations from equations (56) and (57), to be able to solve for the SC terminal current, I_{SC}, as per equations (59) and (60) for charging and discharging, respectively.

$$-I^2{}_{SC}\frac{N_{SC\ series}}{N_{SC\ parallel}}R_{ESR\ sub} - I_{SC}N_{SC\ series}v_{SC\ sub} + P_{SC\ input} = 0 \quad (59)$$

$$I^2{}_{SC}\frac{N_{SC\ series}}{N_{SC\ parallel}}R_{ESR\ sub} + I_{SC}N_{SC\ series}v_{SC\ sub} + P_{SC\ output} = 0 \quad (60)$$

The term $N_{SC\ series}$ is the number of SC sub-modules in series that make-up the SC module, $N_{SC\ parallel}$ is the number of SC sub-modules in parallel, $v_{SC\ sub}$ corresponds to the open circuit voltage for each sub-module in the SC module, and $R_{ESR\ sub}$ is the internal resistance of the SC sub-module. The open circuit voltage can be determined by the stored charge in the capacitor and the capacitance, as per equation (61)[64]. Stored charge can be determined using equation (62), where the maximum possible stored charge, $Q_{Max\ sub}$ is either provided by a technical datasheet, or determined by rearranging equation (61). It is noted that for a capacitor, the definition of SOC is different than that for a battery, where it literally represents the amount of charge stored in a capacitor, relative to the maximum possible stored charge [65]. In a battery, SOC corresponds to the amount of energy stored, relative to its maximum energy storage capacity.

$$v_{SC\ sub} = \frac{Q_{sub}}{C_{sub}} \quad (61)$$

$$Q_{sub} = Q_{Max\ sub}SOC_{SC} \quad (62)$$

Equations (63) to (65) show the conversion for voltage, charge, and capacitance from sub-module to module.

$$v_{SC\ mod} = N_{SC\ series}v_{SC\ sub} \quad (63)$$

$$Q_{mod} = N_{SC\ parallel}Q_{sub} \quad (64)$$

$$C_{mod} = \frac{N_{SC\ parallel}}{N_{SC\ series}}C_{sub} \quad (65)$$

A degradation model was also implemented to account for the cycle aging of the supercapacitor. A supercapacitor can typically carryout 1,000,000 cycles until its capacitance decreases to 80% of its original value and its internal resistance increases to 200% of its original value [66]. Assuming that degradation of the supercapacitor is approximately linear, to maintain simplicity, degradation rates of 2 x 10^{-5} % per cycle and 1 x 10^{-4}% per cycle were used for capacitance and internal resistance degradation rates. The degraded submodule capacitance and internal resistance can be calculated via equations (66) and (67).

$$C_{sub}(cyc = n_{cyc}) = [100\% - D_c * n_{cyc}] * C_{sub}(cyc = 0) \quad (66)$$

$$R_{ESR\,sub}(cyc = n_{cyc}) = [100\% + D_R * n_{cyc}] * R_{ESR\,sub}(cyc = 0) \quad (67)$$

For this project, a SC sub-module was modelled with the properties summarized in Table 3-6. Please note that, due to commercial sensitivity of the component used, only a range has been provided.

Table 3-6. Parameters and variables used to model the SC sub-module

Parameter	Symbol	Value
Capacitance	C_{sub}	150 - 200 F
Capacitance degradation rate	D_c	2 x 10^{-5} % / Cycle
Resistance degradation rate	D_R	1 x 10^{-4}% / Cycle
Energy leaving or entering the SC	E_{SC}	-
Total energy storage capacity	$E_{SC\,sub\,max}$	40 – 60 kJ
Peak power	$P_{SC\,sub\,pk}$	20 kW
Sub-modules arranged in parallel	$N_{SC\,parallel}$	1
Sub-modules arranged in series	$N_{SC\,series}$	1
Number of cycles	n_{cyc}	-
Internal Resistance	$R_{ESR\,sub}$	8 - 15 m Ω
Maximum open circuit voltage	$v_{SC\,sub\,max}$	27 V
Minimum open circuit voltage	$v_{SC\,sub\,min}$	12 V

3.4.2. Supercapacitor Model Results

3.4.2.1. Supercapacitor Model Demonstration

To demonstrate the SC model, a 20 kW_{pk} SC sub-module was simulated where it was subject to a 3 kW charging load for 20s followed by a subsequent discharging load for 20s and simulated with 0.1s time-steps. The charging & discharging and SOC profiles are shown in Figure 3.27 below. Looking at the charging & discharging profile, the following can be observed:

- At time t = 0s to t = 20s:
  - An external 3 kW supply charges the SC, where it initially starts from a minimum SOC of 45% at 0s and reaches 100% at 20s.
  - Although 3 kW is delivered to the SC, the internal losses in the SC result in only about 2.6 to 2.9 kW reaches the cells of the SC and becomes stored as charge. This corresponds to an efficiency of 86 to 99%, which varies depending on the SC's SOC, and the amount of power entering the component.
- At time t = 20s to t = 50s:
  - An external supply of 3 kW is still available throughout this charge cycle; however, the SC now has a SOC of charge of 100%, therefore can no longer receive any more charging power.
- At time t = 50s to t = 70s:
  - There is no more external supply to charge the SC. There is now an external demand of 3 kW.
  - The SC discharges to meet the 3 kW demand for 20s, and in this period the SOC decreases from 100% to 44%.
  - For the SC to be able to supply 3 kW, it must discharge a greater load of approximately 3.1 to 3.7 kW, to take into account the internal losses. This corresponds to an efficiency of 80-96%.
- At time t = 70s to t = 100s:
  - At 70s, the SC has its minimum SOC of ~45% and cannot deliver anymore power.
  - SC remains on standby at its minimum SOC until there is an external charging supply.

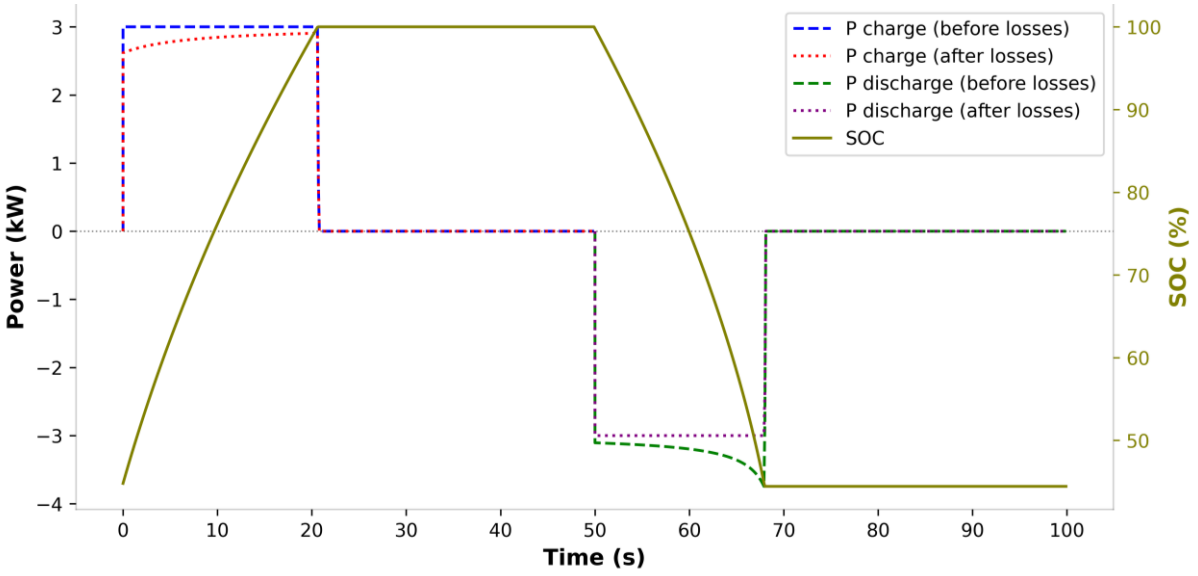

Figure 3.27. Power and SOC profiles for a 20 kW SC during a charge and discharge cycle. SC is subject to a 3 kW supply load for 20s for charging, followed by a 3kW demand for 20s for discharging. The simulation was carried out with time-steps of 0.1s time steps.

3.4.2.2. Supercapacitor Model Validation

The supplier provided measurements for current, voltage and power for the supercapacitor sub-module, during a constant current discharge test, and these are shown in Figure 3.28. A fully charged SC sub-module was discharged at a constant current of 200A until it reached a minimum terminal voltage setpoint, followed by a subsequent charge at the same current until the maximum terminal voltage setpoint was reached. Three simulations with the SC sub-module model were carried out to replicate the test and compare results, and these simulations corresponded to 3 different SC models as described below:

- Model 1 – Based on the original parameters summarized in Table 3-6 in Section 3.4.1
- Model 2 – Internal resistance increased by 2.75x to improve model accuracy
- Model 3 – Internal resistance & capacitance adjusted to improve model accuracy
    - Internal resistance adjusted by 1.8x
    - Capacitance during discharge adjusted by 0.7x
    - Capacitance during charge adjusted by 0.87x

SC Model 1 Results

When comparing the experimental results with those from simulation model 1, a large discrepancy can be observed. The experimental results show that the SC is discharging and charging faster compared to the test model. This may be explained due to the SC having much higher internal losses than the simulation model. The simulation model considers losses with a constant equivalent series resistance (ESR), which is a parameter provided by the manufacturer. This is a nominal value and may not be entirely accurate to assume that it remains constant over the charge cycle. The SC temperature may change the internal

resistance; and considering that the measurements shown in Figure 3.28 were taken from the last pulse of a multiple charge/discharge cycle operation, it is expected that the SC temperature would have increased when compared to its initial conditions. This heating may have affected the internal resistance of the SC.

SC Model 2 Results

By increasing the SC's internal resistance by a factor of 2.75, the simulation results align with the experimental results significantly better than with model 1, particularly when comparing the power profiles. This indicates the need for a more precise internal resistance parameter as the nominal ESR value is not sufficient to simulate the internal losses accurately. In saying this, minor discrepancies are still observed when comparing the terminal voltage profiles for the model 2 simulation results with the experimental profile. For example:

- At the beginning of the discharge cycle at time t= 23s, experimental terminal voltage is 23.9 V, whereas the simulation profile has a lower terminal voltage of 22.5 V.
- When operation changes from discharge to charge at time t = 35s, the simulation model shows a greater initial terminal voltage of 20.5 V whereas the experimental results have this at 15.9 V.
- Additionally, the gradient of the terminal voltage during discharge and charge phases is less steep when compared to the experimental results.

These discrepancies may indicate that internal resistance is not the only parameter that needs calibration, and that an accurate value for capacitance should also be considered.

SC Model 3 Results

The updated parameters for model 3 were determined by iteratively adjusting the internal resistance and capacitance values until simulation results had better alignment with the experimental results. First the internal resistance was adjusted until the initial terminal voltages for the discharge and charge cycle were approximately equal to the corresponding experimental values. Secondly, different capacitance values were approximated for the discharge and charge cycle. For the discharge cycle, the capacitance was adjusted until the simulation could achieve the minimum terminal voltage setpoint at 35s. A similar procedure was used for the charge cycle, where the capacitance was determined when the model reached the maximum terminal voltage setpoint at 41s. By comparing the simulation and experimental results, it is clear that model 3 is more accurate than model 1. The most notable discrepancy for model 3 is the linear behaviour of the terminal voltage during charge and discharge, whereas the experimental results display non-linear behaviour. When comparing the results with Model 2, it is evident that during discharge, the power and terminal voltage profiles of Model 2 align more closely with the experimental data than those of Model 3; however, the opposite is true during charging. Therefore, it is not entirely clear whether model 2 or model 3 is more suitable. Further experimental results are required to carry out validation

of model 2 and 3 and confirm which approach is more suitable for modelling the SC. Despite this, the errors for SC model 2 and 3 are minor; and considering that the SC will be used for a long-term analysis in subsequent task D2.3, the level of error is deemed acceptable for the purpose of our project.

Lastly, the validation results were limited in determining whether the degradation of the SC was accurately represented in the model. Similar to the VRFB and the salt-based battery, the simulation and experimental results for the SC were based on a single charge-discharge cycle. However, significant degradation effects would be observed after thousands of cycles. To effectively include degradation in the validation, long-term experimental data spanning many cycles would be necessary, but such data was not available at the time. In the upcoming tasks for deliverable D2.3, the SC will be simulated over an extended period, with the expectation that degradation will have a meaningful impact on the results. Therefore, it must be stated that the current validation only reflects short-term behaviour of the SC, leaving long-term degradation effects not fully assessed.

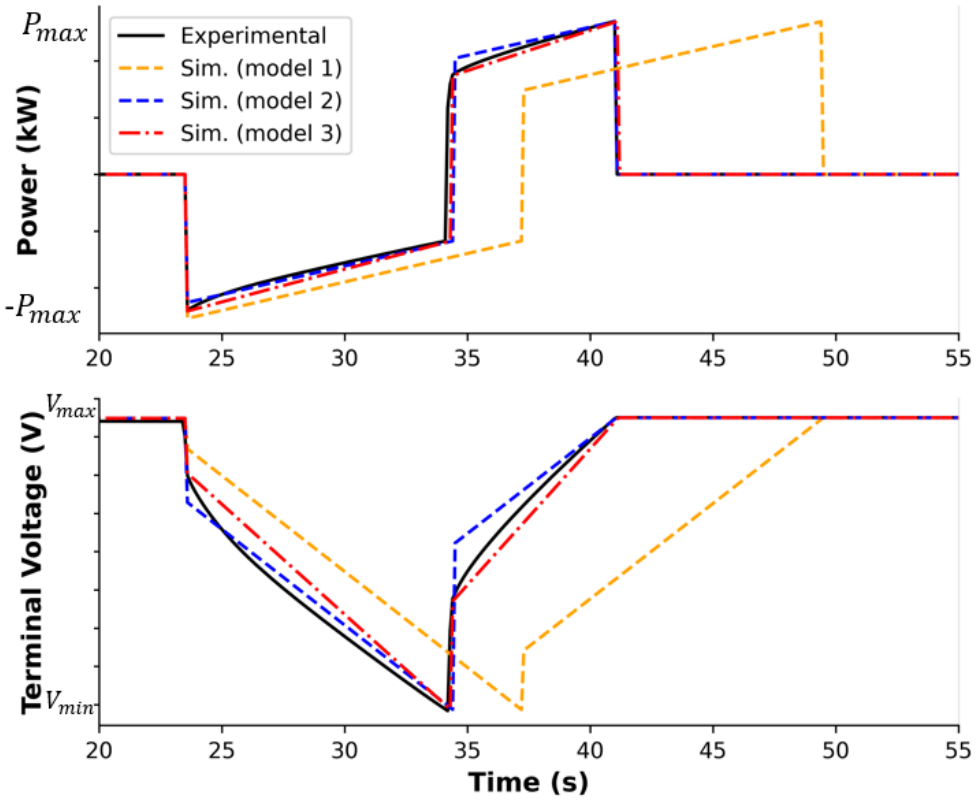

Figure 3.28 SC sub-module experimental vs simulation results for a constant current discharge and charge at 200 A. Y axis values have been obscured at the manufacturers request.

4. INTERACTION MODELING AND OPERATIONAL STRATEGY

In this chapter, we focus on the interaction modelling and operational strategies for HESS that combine RFB/salt-based battery with supercapacitor. Understanding how HESS can be utilized under different scenarios is crucial to determine their technical and economic viability [67]. We have described various working conditions and applied a comprehensive framework to assess whether the integration of RFB or salt-based batteries with SC is suitable across diverse scenarios.

Traditionally, long-term techno-economic optimization strategies for battery systems have employed larger time steps, such as 1 hour or 15 minutes [68]. These time resolutions are sufficient for capturing the overall performance and trends of battery operations over extended periods [69]. However, they may not adequately represent the rapid response capabilities of SCs. To accurately model the role of SC, it is essential to consider smaller time frames, such as minutes or seconds [70]. This finer temporal resolution allows for a more precise analysis of the SC's contribution, especially in managing short-term power fluctuations and enhancing system efficiency [71]. Although we do not analyse the dynamic behaviour [72] of the system in D2.2, we have conducted a techno-economic analysis using HESS models. This analysis provides a platform that will serve as the foundation for D2.3, where this platform will be used for sizing HESS under various applications.

4.1. DEFINING THE INTERACTION MODELS BETWEEN RFB/SALT-BASED BATTERIES AND SC

In the SMHYLES project, two HESS configurations will be installed, as summarised below:

1. **DEMO#01:** An aqueous-based RFB combined with an aqueous-based SC (AHESS).
2. **DEMO#02:** A Salt-based battery combined with an aqueous-based SC (SHESS)**.**

These configurations will be tailored for different scenarios and use cases based on the specific needs of each demonstration site, as described in Deliverable D2.1. In D2.2, the techno-economic assessment of HESSs in various operational contexts is analysed. To complement the usage of HESS and understand their techno-economic benefits across different scenarios, it is developed a comprehensive platform. This platform incorporates detailed models of HESS components to analyse their performance over the long term. By including long-term optimization methods, we aim to provide demo owners with valuable insights into how the usage of HESS under different scenarios can enhance profitability and system stability. Additionally, this platform will serve as a foundation for D2.3, where more detailed scenarios for the optimal sizing of HESS will be explored.

In the first configuration, due to technological limitations, the RFB may de-rate its power output during charging processes. This de-rating means the RFB cannot always charge at its nominal power level, leading to reduced performance and efficiency. We observed that the SC can effectively compensate for the power rate restrictions of the RFB and the integration of the SC provides additional flexibility for the HESS by:

- **Enhancing Charging and Discharging Rates:** The SC can charge and discharge at faster rates than the RFB, allowing it to handle rapid power fluctuations that the RFB cannot manage alone.
- **Smoothing Power Profiles:** By absorbing excess energy or supplying power quickly, the SC helps in providing a smoother overall power profile for the HESS.
- **Mitigating De-rating Effects:** The SC compensates for the RFB's de-rated power output, ensuring that the system can meet the required power demands more effectively.

In the second configuration, the SC compensates for the limitations of the salt-based battery, which can be affected by the following derating events:

- **Enhancing Charging and Discharging Rates:** The SC can charge and discharge at faster rates than the salt-based battery, allowing it to handle rapid power fluctuations that the salt-based battery cannot manage alone.
- **Temperature Sensitivity:** Salt-based batteries have operational constraints based on their minimum and maximum temperature set-points which affecting their performance.
    - When the battery temperature approaches the minimum temperature set-point due to ambient or entropic cooling, the battery will use an integrated heater to heat itself by either self-discharging, using some externally available power source. This will affect battery operation and may limit the amount of power it can recharge itself with or supply.
    - When the battery temperature approaches the maximum temperature set-point, it must cool passively as it has no active cooling system. In such a case, the battery will derate to minimize self-heating effects during operation.
- **State of Charge Restrictions:** Technological restrictions related to SOC can prevent the battery from providing sufficient power when needed, where the battery operation will derate to prevent an overcharge or over-discharge.
- **Current and Voltage Limits:** Technological restrictions related to current and voltage. For example, the salt-based battery follows a constant current and constant voltage charging, hence derating can occur to maintain battery charging within these limits.

This synergy between the SC and both batteries enhances the operational flexibility and reliability of the HESS, making it more adaptable to varying energy demands and generation patterns. Beyond compensating for battery limitations, the SC plays a crucial role in enhancing

system stability. SCs can respond to rapid power fluctuations, effectively reducing spikes that can occur in power systems. By smoothing out sudden changes in power flow, the SC helps maintain a stable and high-quality power supply. Additionally, the ability of the HESS to manage power spikes makes it more compatible with grid requirements and can prevent potential disruptions. Our analysis takes these stability benefits into account, demonstrating that the integration of SCs not only improves performance but also contributes to the robustness of the energy system.

We employ SCs primarily to compensate for the limitations of RFBs and salt-based batteries, particularly concerning their power de-rates. Operational limits can cause these batteries to de-rate, preventing them from charging at their nominal power levels under certain conditions. This derating leads to reduced performance and efficiency. Integrating SC mitigates these limitations by absorbing excess power that the batteries cannot handle, thereby ensuring that the batteries operate within their optimal parameters. A critical aspect of our operational strategy is using SC to reduce the curtailment of PV energy. SC can absorb power spikes occurring in shorter time frames that exceed the power handling capabilities of traditional batteries [67]. By capturing this excess energy, SCs prevent potential energy losses and facilitate the subsequent transfer of this energy to the batteries when conditions are more favourable. This approach enhances the overall efficiency of the energy storage system and maximizes the utilization of generated PV power. Figure 4.1 shows the general overview of our approach.

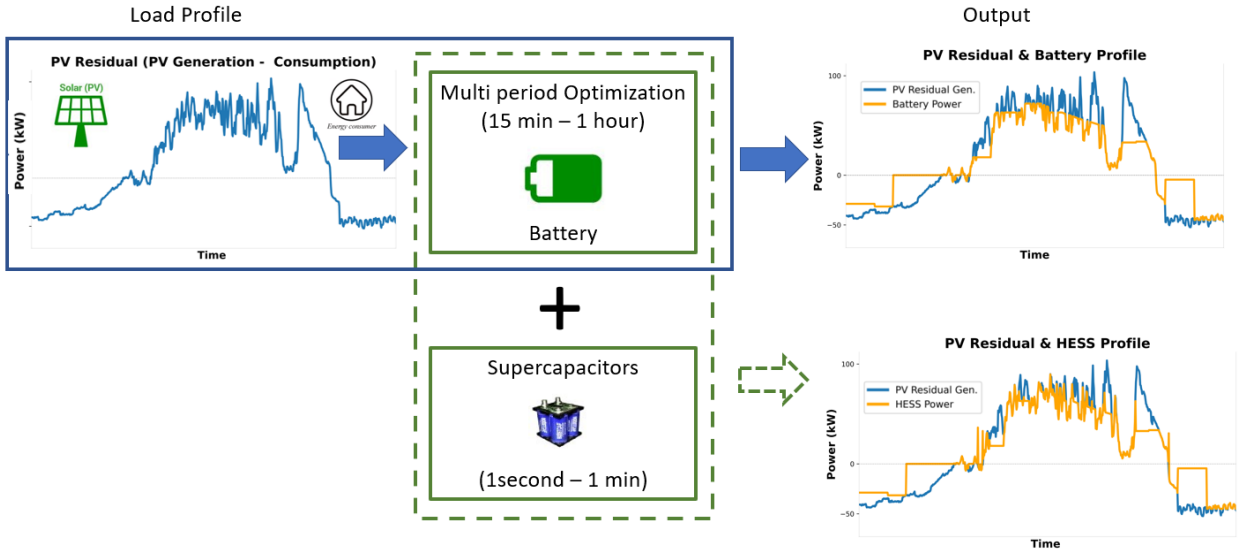

Figure 4.1 General overview of the approach using multi-period optimization for battery and HESS arrangements.

4.2. IMPLEMENTATION OF MULTI-OBJECTIVE OPTIMIZATION TOOLS

We have implemented data-driven multi-period optimization strategies to enhance the optimal management and planning of HESS. This tool builds on previous applications, such as

the optimization of Li-ion batteries in power systems, with the goal of increasing the profitability of battery energy storage systems (BESS) operations in day-ahead and balancing markets in which the tool accounted for both calendar and cycle aging of a Li-ion battery, incorporating these factors into the cost function for realistic economic assessments [74]. Additionally, an updated version of this tool has been successfully used for real-time BESS optimization, considering the aging costs of BESS [75].

The foundation of this optimization tool lies in the use of a genetic algorithm (GA) as the core optimizer, operating on an hourly timeframe and optimizing BESS performance daily (24-hour cycles). These strategies have proven effective for long-term techno-economic optimization over periods of a year, emphasizing their flexibility and robustness. Notably, the tool was introduced for self-consumption maximization in earlier work [76], demonstrating its adaptability to diverse energy management objectives.

We have enhanced the optimization tool for a recent study to incorporate advanced systems, such as RFBs and SCs, with a focus on the techno-economic optimization of HESS for electric vehicle (EV) stations [77]. A recent updated version incorporates both high-temporal and low-temporal input data for HESS operation, enabling more precise and dynamic energy management. Figure 4.2 illustrates the general workflow of the updated tool, emphasizing its key components.

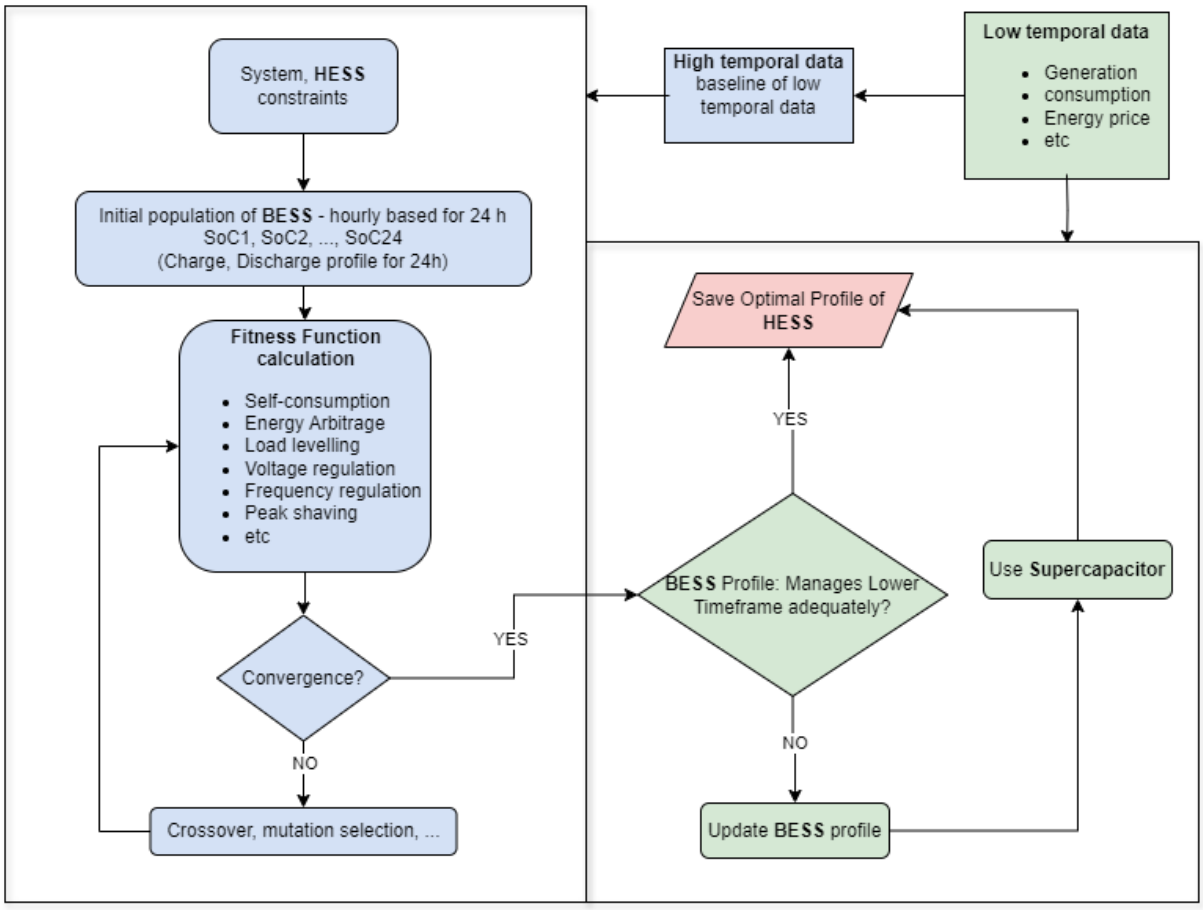

Figure 4.2 Multi-Objective-Multi-Period optimization for HESS general workflow

The tool leverages both high-temporal data (e.g., frequency regulation) and low-temporal data (e.g., energy prices and consumption baselines) for optimization. Specially, if BESS profiles do not meet operational requirements for shorter timeframes, SC is integrated to handle high-frequency fluctuations, ensuring system reliability and efficiency. By incorporating SCs into our optimization framework, we leverage their rapid response capabilities to complement the slower dynamics of RFBs and salt-based batteries. This synergy allows the HESS to effectively respond to market signals, manage fluctuating energy demands, and maximize profits through strategies such as energy arbitrage. Besides, our multi-objective optimization approach balances economic and technical goals, such as minimizing operational costs, reducing PV curtailment, and enhancing HESS efficiency by preventing excessive charging/discharging rates. By addressing these objectives, we develop operational strategies that not only improve the performance and profitability of HESS but also align with sustainable energy management practices.

While numerous applications of HESS have been discussed in the literature [78], our work distinguishes itself by adopting scenarios that closely resemble real-world conditions. There is a notable scarcity of long-term techno-economic assessments that simultaneously consider both the short-term dynamics required for SC and the longer-term operations relevant for

batteries over periods like one year. D2.2 addresses this gap by providing a simulation tool that will be used in D2.3, where a novel and comprehensive analysis will integrate dual time frames into the evaluation of HESS performance. The significance of this work lies in its provision of a versatile framework, applicable to real-time HESS applications within Energy Management Systems (EMS), by updating the current tool structure. This framework can generate setpoints that account for different market schemes, HESS time frames, and operational restrictions. By considering both the rapid response of SCs and the energy capacity of batteries, the framework offers a practical tool for optimizing HESS operations in various market and demand scenarios [79]. The methodologies and findings from this study will also be used in D2.3, which focuses on the sizing of HESS. By understanding the operational interactions and constraints of the combined energy storage technologies, we can develop more accurate sizing models that ensure the HESS meets performance expectations while remaining economically viable.

In the subsequent sections (Section 4.3 and 4.4) we showcase our optimization tool with preliminary analyses for HESS co-located with PV. Section 4.3 demonstrates how the tool could be used to maximize self-consumption, and Section 4.4 demonstrates how the tool can be optimized for energy arbitrage. All the data used in this work is real data and obtained from [80]. The data includes information on PV production and consumption over a long-term period of more than one year, with varying temporal resolutions such as daily, hourly, minute-based, and, for some periods, even second-level granularity. By adjusting the IP settings, the data can be expanded to access information from different user categories, including households, commercial entities, and industrial operations.

4.3. SHOW CASE OF HESS FOR SELF-CONSUMPTION ENHANCEMENT

In this section, we demonstrate the interaction between batteries and supercapacitors within a HESS, showing how the SC's contribution increases self-consumption and reduces PV curtailment without considering any optimization. Three types of simulations were carried out:

1. Battery only - Simulated with a temporal resolution of 1 minute.
2. HESS – Battery and SC both simulated with a temporal resolution of 1 minute
3. HESS – Battery was simulated with a temporal resolution of 1 minute and SC simulated with a temporal resolution of 1 second.

The purpose of simulation 1 and 2 was to understand the efficacy of the HESS by assessing the additional support provided by the SC. The purpose of simulation 2 and 3 was to compare and highlight the impact of the SC’s temporal resolution on the HESS performance. A total of 5 simulations were carried, where the VRFB was used for all 3 simulation types, and the salt - based battery was used for simulation 1 and 2 only.

To clarify the self-consumption concept in the proposed methodology, Figure 4.3 shows an example of the power time evolutions of each component. When PV overproduction occurs, the BESS charges until it reaches maximum SOC. Subsequently, during PV underproduction, the BESS supplies the residual power demand to maximize the self-consumption of the PV production.

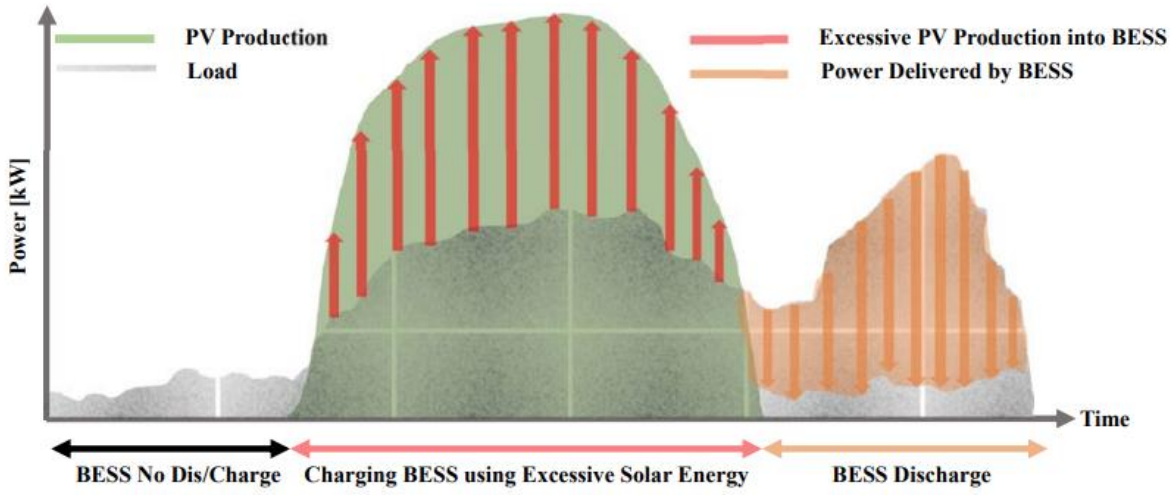

Figure 4.3 Example of time evolutions of powers for maximisation of self-consumption of PV [76]

By analysing the residual power, the difference between PV generation and load demand, we illustrate the benefits of integrating an SC with a BESS. The objective function of self-consumption (denoted as $F_{self\ consumption}$) is presented in equation (68), which aims to minimize the difference between the residual power (as per equation (69)) and HESS power (as per equation (71)). As described in the equation (70), a positive $P_{residual}$ corresponds to excess solar production that will be curtailed, whereas a negative $P_{residual}$ corresponds to residual demand that must be met via other sources (eg the grid). By using a HESS, $P_{residual}$ is reduced as excess solar production can be used to recharge the system, hence reducing the amount of solar curtailment; and the HESS can discharge to help meet some of the residual demand, reducing the amount required from the grid.

$$F_{self\ consumption} = \min \left| \int P_{residual} - P_{HESS}\ dt \right| \quad (68)$$

Where:

$$P_{residual} = P_{PV} - P_{consumption} \quad (69)$$

$$Residual\ Power = \begin{cases} Excess\ PV\ to\ Curtail & 0 < P_{Residual} \\ Residual\ Demand & 0 > P_{Residual} \end{cases} \quad (70)$$

$$P_{HESS} = P_{battery} + P_{SC} \quad (71)$$

$$Battery\ Mode = \begin{cases} Charging & 0 < P_{battery} \\ Discharging & 0 > P_{battery} \end{cases} \quad (72)$$

$$SC\ Mode = \begin{cases} Charging & 0 < P_{SC} \\ Discharging & 0 > P_{SC} \end{cases} \quad (73)$$

In the initial scenario, the battery operates on a minute-by-minute basis to smooth out the residual power. While this approach reduces some mismatch between PV generation and load demand, the battery's inability to handle sudden power fluctuations, due to technological restrictions, leads to higher PV curtailment and lower self-consumption rates. The example in Figure 4.4 shows the results of a simulation using a RFB system coupled to a PV plant. The RFB is comprised of 3 x 15 kW / 125 kWh modules, corresponding to a total system size of 45 kW / 375 kW. It is noted, however, that the nameplate power of 45 kW for this system is a nominal value and will vary with SOC. In the proceeding results, it can be seen that the system can achieve a peak power of up to 75 kW; therefore, to prevent confusion when analysing the results, the system will henceforth be referred to as a 75 kW/375 kWh RFB. In this arrangement, the RFB will recharge using the solar production when there is a surplus of PV generation (when PV residual generation is positive); however, the RFB will only be able to recharge at its maximum rated power. When solar generation exceeds the RFB's maximum rated charging power, the excess solar will be curtailed. When there is a power consumption, denoted by a negative PV residual generation, the RFB will discharge to help meet the demand. The RFB can only discharge up to its maximum rated discharge power, and any power demand that exceeds this must be met by some other source. In an ideal scenario where an energy storage system is employed to maximize self-consumption, the RFB charging and discharging profile would match the PV residual generation profile. This is not the case in the example due to the limitations of the RFB.

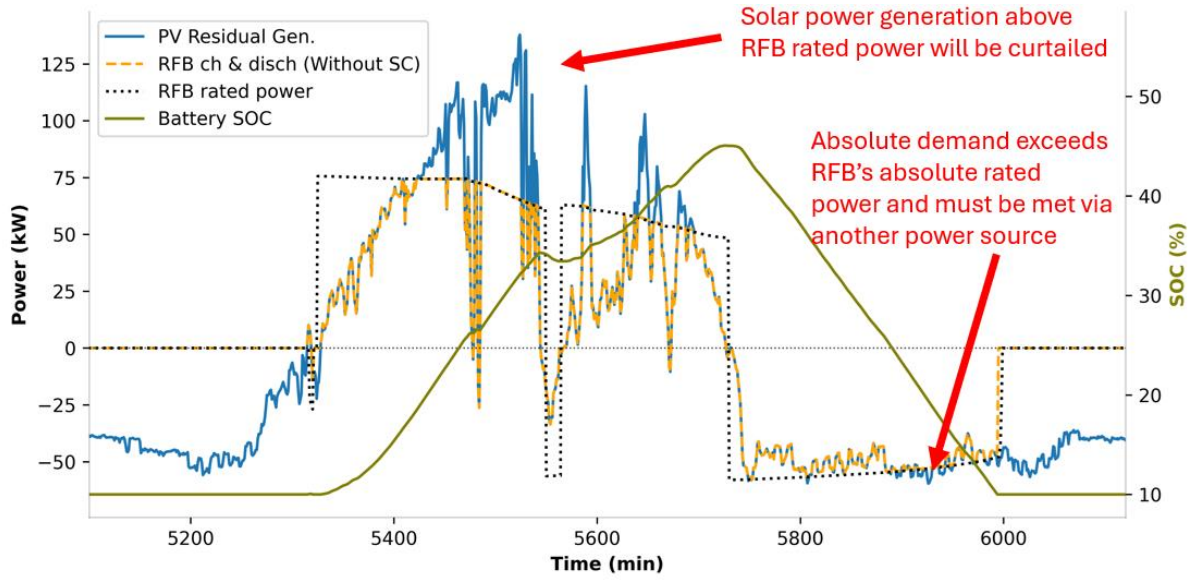

Figure 4.4 Example of a 75 kW/ 375 kWh VRFB coupled to a 140 kWp PV plant, to be used for self-consumption, with a temporal simulation resolution of 1 minute.

A similar simulation was carried out as above, this time using a HESS comprised of a 75 kW/ 375 kWh RFB and a 1000 kW SC. We note that the size of the SC is based on peak power of a module comprised of 50 sub-modules described in Table 3-2 in Section 3.4.1. Figure 4.5 shows the charge and discharge profiles for the RFB and SC components, and Figure 4.6 shows the total charge and discharge profile for the entire HESS. During charging, the HESS can absorb PV generated power at greater levels than the maximum RFB rated power, due to the addition of the SC. A similar outcome is shown during discharge. By comparing Figure 4.4 and Figure 4.6, it is clear that the HESS charge and discharge profile matches the residual PV generation profile better than the 'RFB only' case, indicating that the HESS is better suited for self-consumption. Introducing the SC into the HESS allows for better management of short-term power spikes. The SC's rapid response capability enables it to absorb excess energy that the battery cannot handle within each minute interval.

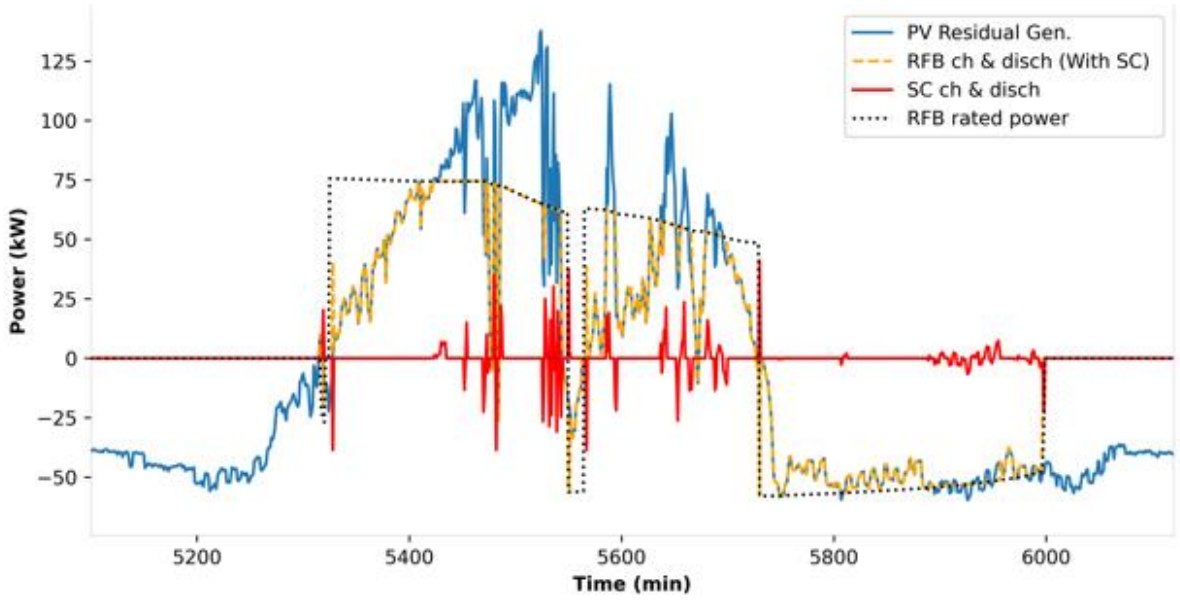

Figure 4.5 Charge and discharge profiles for the VRFB and SC when they are interacting together to maximize self-consumption of a 140 kWp PV plant. The component sizes were: 75 kW/ 375 kWh VRFB, and 1000 kW SC. The temporal resolution of the simulation was 1 minute.

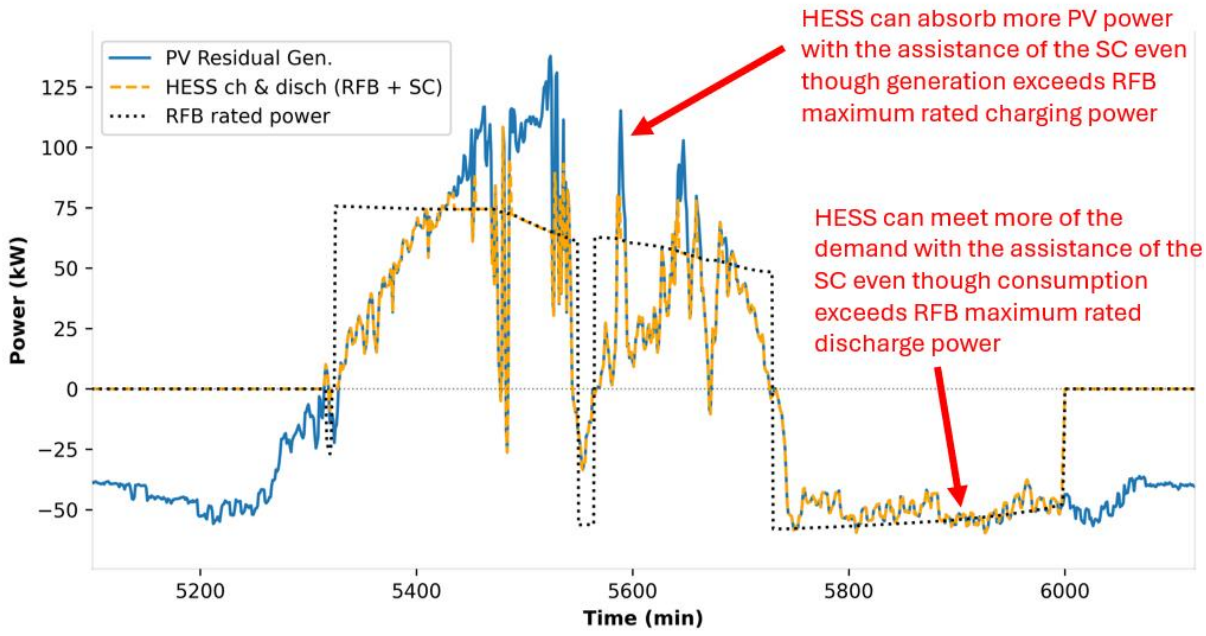

Figure 4.6 Charge and discharge profile for the entire HESS (SC + RFB power profiles) when coupled to the 140 kWp PV plant to maximize self-consumption. The component sizes were: 75 kW/ 375 kWh VRFB, and 1000 kW SC. The temporal resolution of the simulation was 1 minute.

When operating the battery on a second-based timeframe, it provides more granular control over its charging and discharging processes. However, even with this finer temporal resolution, the battery alone still struggles with rapid power fluctuations occurring within seconds. The high-frequency components of the residual power remain unaddressed,

resulting in persistent PV curtailment and suboptimal self-consumption (see Figure 4.4), like the minute-based analysis. By integrating the SC into the second-based timeframe, we observe that the SC effectively handles the rapid fluctuations in the residual power, absorbing and releasing energy within seconds.

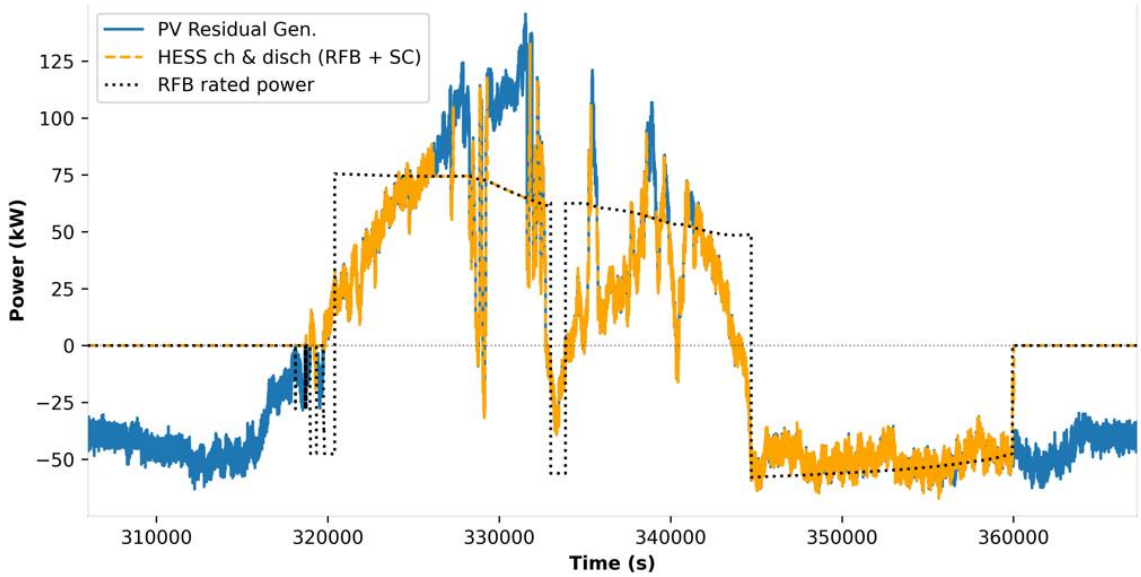

Figure 4.7 Charge and discharge profile for the entire HESS (SC + RFB power profiles) when coupled to the 140 kWp PV plant to maximize self-consumption. The component sizes were: 75 kW/ 375 kWh VRFB, and 1000 kW SC. The temporal resolution of the simulation was 1 second.

A preliminary analysis was carried out to compare results between a simulation with a 1-minute resolution vs a simulation with a 1-second resolution, and this is summarised in Table 4-1. The simulations were carried out using a 75 kW/375 kWh RFB and 1000 kW SC, coupled to a 140 kWp PV plant, over a period of 9 days. The results show the total curtailed solar energy (generated solar energy that could not be used by the storage system or load) and the unmet residual demand energy (demand that was not met by the solar plant and the storage system). The results also compare for the case of using a battery only and the HESS. By comparing the 1 minute and 1 second resolution results, we can see that the maximum relative difference between them is 0.3%, this is due to the balance between charging and discharging processes of SC. Although using data with 1-second resolution can provide more accurate simulation results, this is at the expense of computational effort and requires a significantly longer time to perform. Since the focus of the study is a long-term (one-year) techno-economic analysis, the difference between using second-based or minute-based timeframes is not substantial. Therefore, while the SC handles immediate power spikes and the battery manages longer-term energy shifts, the overall efficiency is maximized without significantly impacting the long-term analysis outcomes. Considering that relative difference in results is insignificant, 1-minute resolution has been deemed acceptable and further simulations will use this as the simulation time-step.

Table 4-1. Results comparing the self-consumption of a PV system with 'battery only' and 'HESS' scenarios. The results also compare simulations carried out at 1-second and 1-minute intervals over a 9-day period.

	1 Second Resolution		1 Minute Resolution		Error (Sec vs Min)
	Battery Only	HESS	Battery Only	HESS	
Curtailed Solar (kWh)	674	650	672	650	0-0.3%
Unmet Residual Demand (kWh)	4,764	4,755	4,762	4754	0.02-0.04%

Figure 4.8 shows the new residual power when using only a RFB and when using a HESS, based on the 9-day simulation as described above. The new residual is the original PV residual minus the charging or discharging power of the battery or HESS. Figure 4.9 presents a closer inspection of the results over the course of day 4 of the simulation. When using the HESS, there is less curtailed solar and less residual demand, when comparing to the 'RFB only' profile. This demonstrates the efficacy and benefits of using the SC with such a strategy. The results in Table 4-2 further demonstrate this, showing that a HESS causes 3.3% less curtailment and 0.2% less demand over a 9-day period.

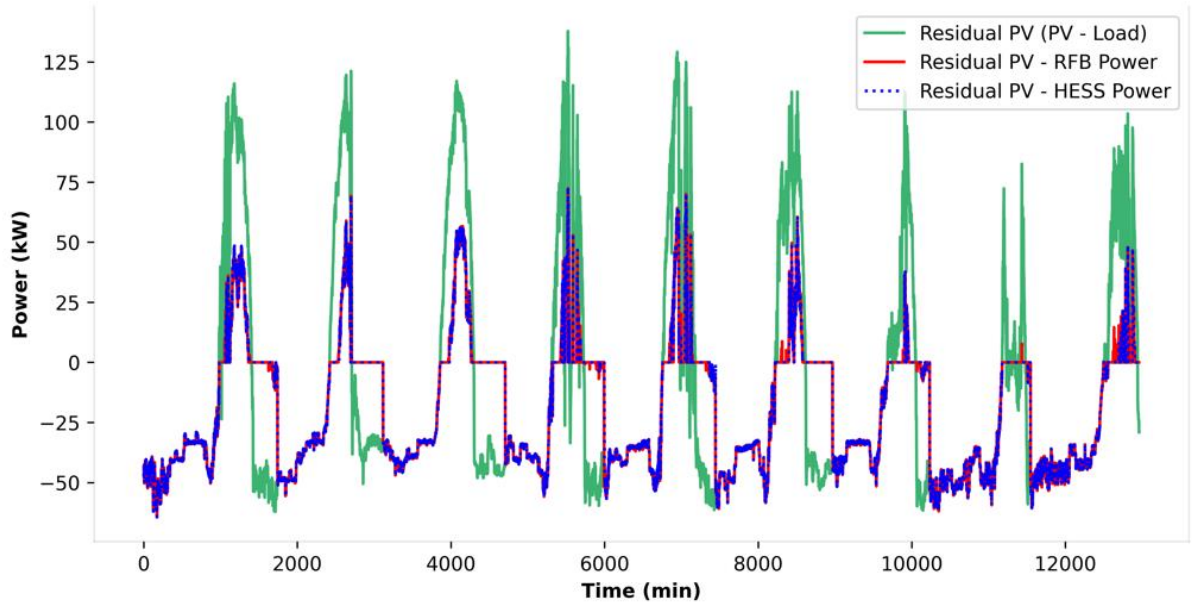

Figure 4.8 New residual power with RFB (Residual PV – RFB Power) and HESS (Residual PV – HESS Power) when coupled to a PV plant over a 9-day period. The VRFB was sized at 75 kW/ 375 kWh and the SC at 1000 kW.

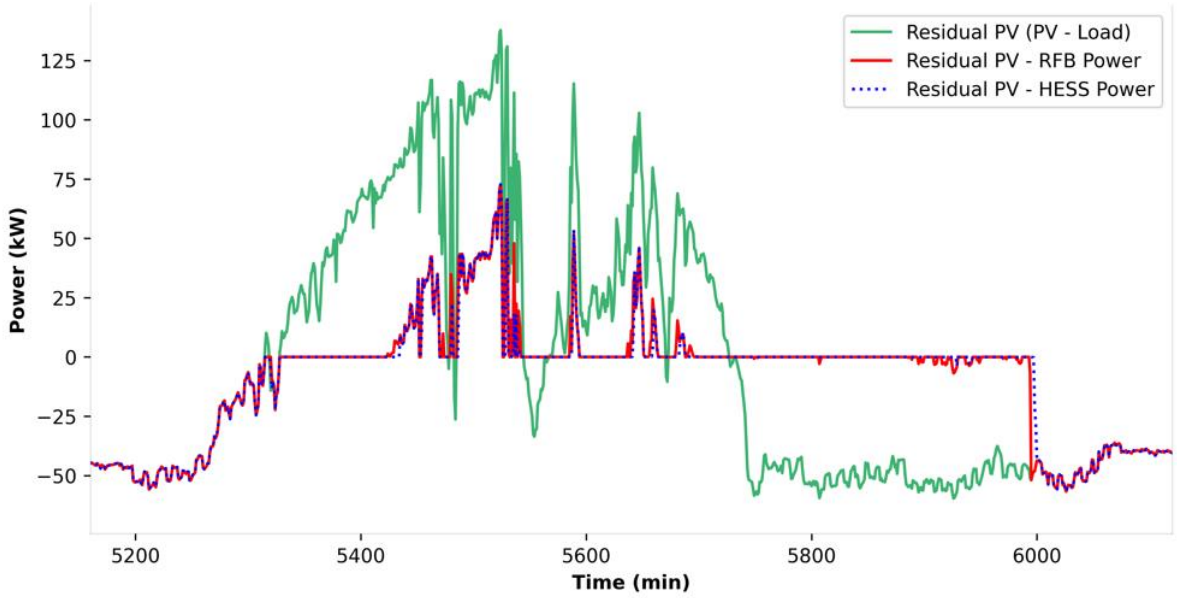

Figure 4.9 New residual power with RFB (Residual PV – RFB Power) and HESS (Residual PV – HESS Power) when coupled to a PV plant over a 9-day period, with a closer inspection on day 4. The VRFB was sized at 75 kW/ 375 kWh and the SC at 1000 kW.

Table 4-2 Total curtailed solar and residual demand energy when using an RFB vs HESS over 9 days.

	Storage System		RFB vs HESS Difference	
	RFB Only	**HESS**	**Abs**	**%**
Curtailed Solar (kWh)	672	650	- 22	-3.3%
Unmet Residual Demand (kWh)	4,762	4754	-8	-0.2%

A preliminary simulation for a single day was also carried out using the salt-based battery model with the same residual PV data as for the RFB example. This was carried out for a nominal battery size of 75 kW / 288 kWh, comprised of 2 sub-modules in series and 15 in parallel. For better comparison with the RFB, it would have been preferable to simulate a salt-based battery of the same rated power and storage capacity as the RFB; however, both battery models are based on modules that have a fixed rated power and energy storage, therefore it was not possible to develop two identical models without deviating from the supplier provided battery parameters. Because the interaction algorithm between the battery and SC is based on the battery rated power and the excess PV generation, we focussed on simulating an RFB and salt-based battery with similar power ratings of 75 kW.

Figure 4.10 to Figure 4.13 demonstrate how the salt-based battery may work for this single day, when it has an initial SOC of 15% and battery temperature of 280 °C. The residual PV data used was day 4, to compare with the similar results for the RFB shown in Figure 4.4 to Figure 4.6. Figure 4.10 shows the salt-based battery's charge and discharge profile over day 4, as well

as its corresponding temperature and SOC. Figure 4.11 shows the behaviour of the salt-based battery when it interacts with the SC to form a HESS and Figure 4.12 shows the overall charge and discharge profile for the entire HESS. By incorporating the SC with the salt-based battery, the charging profile of the HESS follows the residual load profile more faithfully compared to the battery only scenario, and this is similar to what was observed in the RFB simulations. Lastly, Figure 4.13 compares the original residual power with new residual power for the battery only (Residual power – Salt-based battery power) and HESS (Residual power – HESS power) scenarios, and Table 4-3 provides the total amount of curtailed solar energy and new residual demand energy over the simulated period. Based on the results, there is a benefit to using the SC, as the HESS experiences 2.4% less solar curtailment and a 0.7% lower new residual demand, when compared to the battery only scenario.

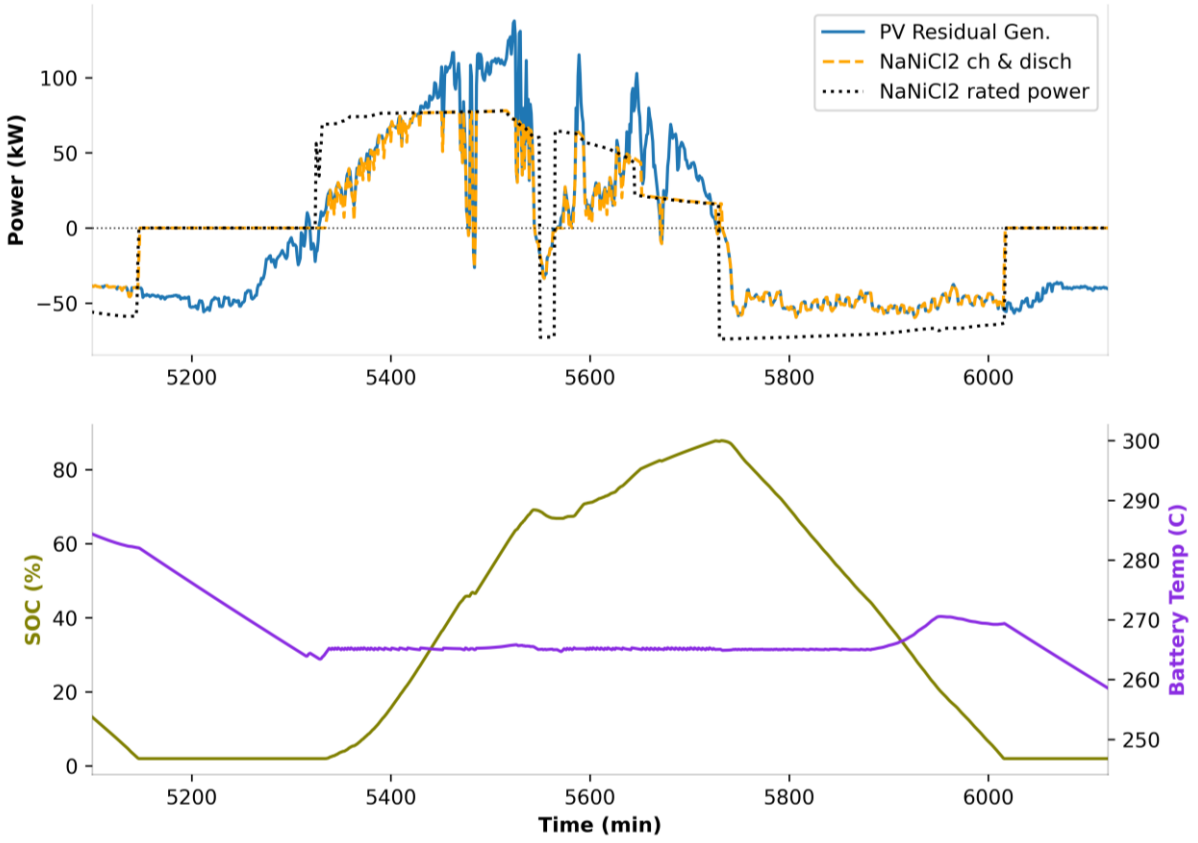

Figure 4.10. Charge and discharge profile for a 75 kw/ 288 kWh salt-based battery coupled to a 140 kWp PV plant to increase self-consumption, simulated at a temporal resolution of 1 minute.

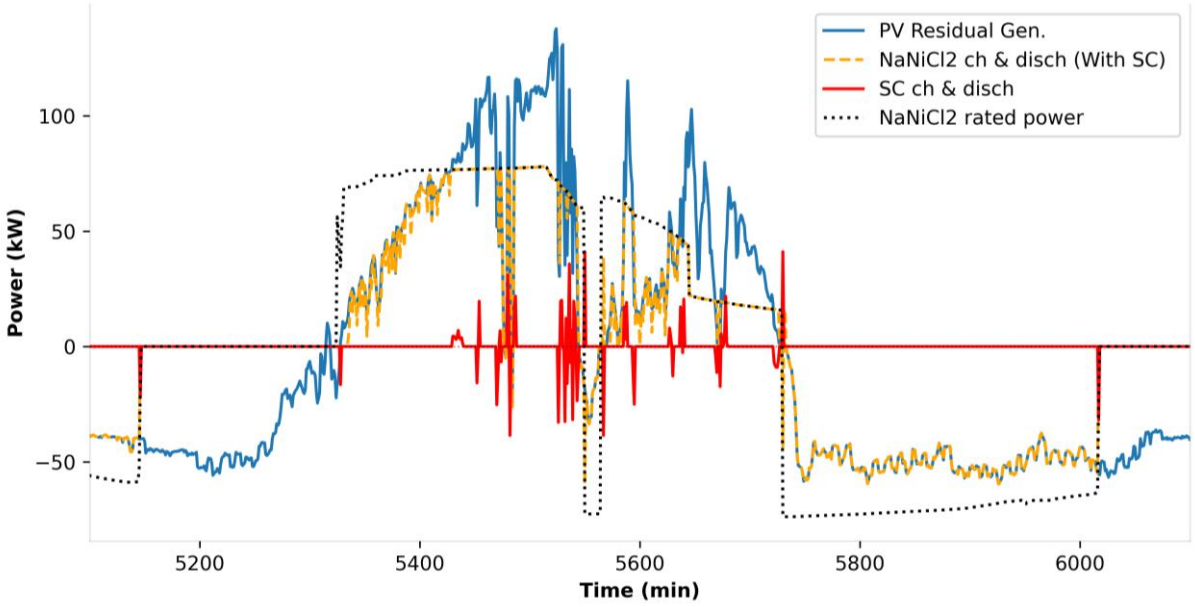

Figure 4.11. Charge and discharge profiles for the $NaNiCl_2$ battery and SC when they are interacting together to maximize self-consumption of a 140 kWp PV plant. The component sizes were: 75 kW/ 288 kWh $NaNiCl_2$, and 1000 kW SC. The temporal resolution of the simulation was 1 minute.

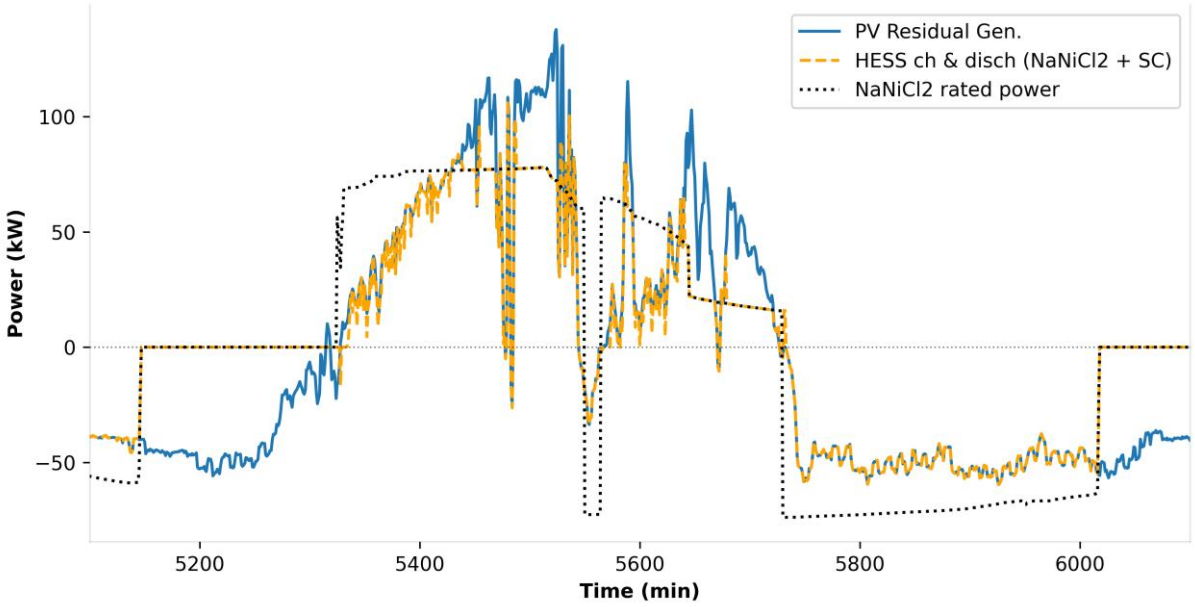

Figure 4.12. Charge and discharge profile for the entire HESS (SC + $NaNiCl_2$ power profiles) when coupled to the 140 kWp PV plant to maximize self-consumption. The component sizes were: 75 kW/ 288 kWh $NaNiCl_2$, and 1000 kW SC. The temporal resolution of the simulation was 1 minute

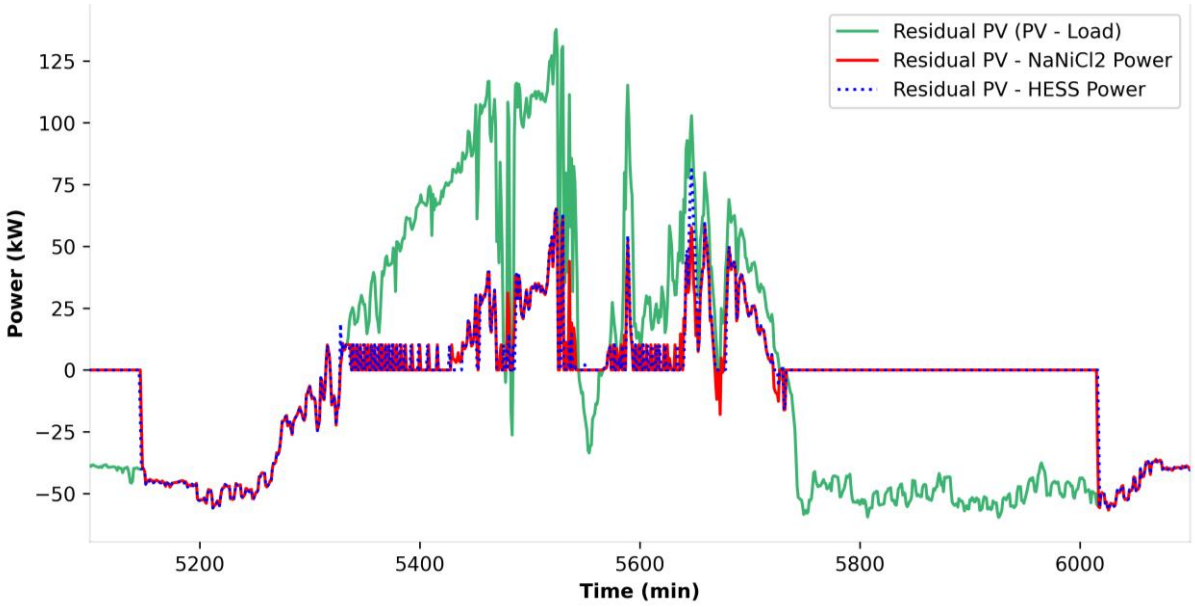

Figure 4.13. New residual power with $NaNiCl_2$ (Residual PV – $NaNiCl_2$ Power) and HESS (Residual PV – HESS Power) when coupled to a 140 kWp PV plant. The $NaNiCl_2$ battery was sized at 75 kW/ 288 kWh and the SC was sized at 1000 kW.

Table 4-3 Total curtailed solar and residual demand energy when using a Salt-based battery ($NaNiCl_2$) vs HESS a single day (day 4)

	Storage System		$NaNiCl_2$ vs HESS Diff.	
	$NaNiCl_2$ Only	**HESS**	**Absolute**	**%**
Curtailed Solar (kWh)	85	83	-2	-2.4%
New residual demand (kWh)	278	276	-2	-0.7%

4.4. OPTIMIZATION OF HESS FOR ENERGY ARBITRAGE

In this section, we showcase how our optimization tool, introduced in Section 4.2, demonstrates the interaction between batteries and SCs within a HESS for energy arbitrage purposes. In another words, the optimization of the HESS is explored, both with and without the integration of a SC. We implemented a multi-period optimization strategy using a genetic algorithm (GA) for the RFB and Salt based Battery, optimizing the battery's operation on an hourly basis for energy arbitrage purposes. This approach aimed to determine the optimal power exchange in each hour to maximize economic benefits by leveraging fluctuations in energy prices. Figure 4.13 shows the flowchart of the GA based optimisation process for energy arbitrage.

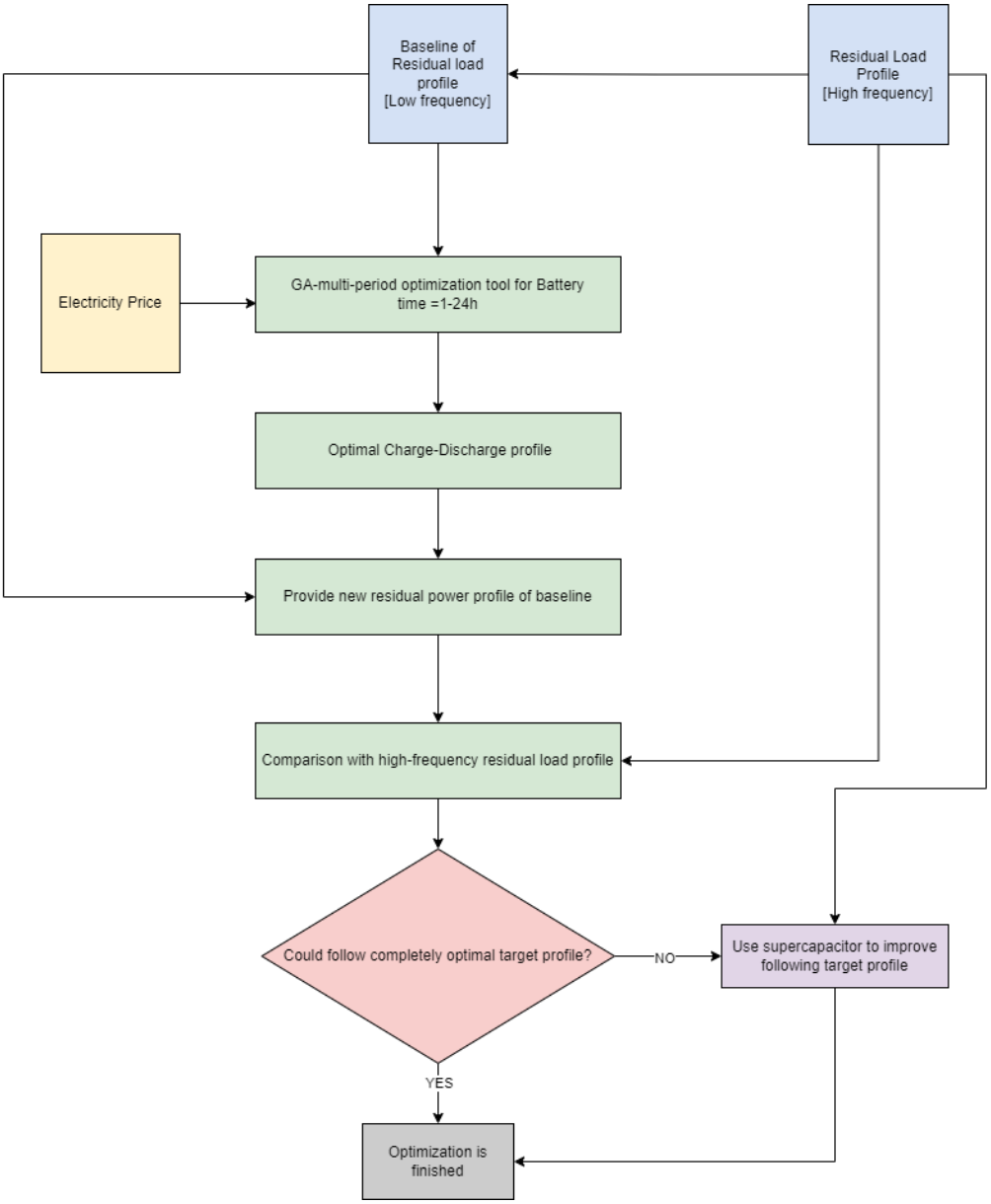

Figure 4.14 Flow chart of the HESS optimization process for energy arbitrage.

In the optimization process, an optimal hourly power profile for the battery is obtained to maximize arbitrage opportunities [81]. However, technological restrictions, such as power de-rating at certain levels, prevent the RFB and Salt-based battery from following the optimal requested power profile precisely. To address this challenge, the SC that forms part of the HESS, operates at a lower time frame, providing rapid response capabilities that complements the slower dynamics of the battery. When the battery cannot follow the optimal power profile due to de-rating of its power, the SC automatically offers support by absorbing excess power that the battery cannot handle, preventing energy losses and reducing PV curtailment. In other words, the SC maintains a more stable power profile for the battery by smoothing power fluctuations, managing short-term power spikes and dips. This integration of the SC allows the system to follow the optimal power profile more closely, enhancing both economic and

technical performance. The objective function of arbitrage, denoted as $F_{arbitrage}$ is presented in equation (74), and corresponds to minimizing the cost of total electricity used. The cost of electricity purchased from the grid, $C_{grid}(t)$ is based on the dynamic electricity pricing that varies depending on the time of the day. The residual power, $P_{resiudal}$, and HESS power, P_{HESS} , are described in further detail by equations (68) to (73) in Section 4.3. It is noted that this objective function only applies when the new residual power (equation (75)) is below zero. In such a situation, HESS discharge power was not sufficient to meet the entire demand, hence there is still some remaining load that must be provided by purchasing from the grid. If the new residual is above zero, there is still excess solar despite using the PV generation to recharge the battery. In this case, the excess solar net of battery charging will be curtailed; however, it is also possible to simulate a separate case where the excess solar is sold back to the grid and hence further reducing the costs.

$$F_{arbitrage} = \min \int |[P_{residual} - P_{HESS}\ ]dt| * C_{grid}(t) \qquad [P_{residual} - P_{HESS}\ ] \leq 0 \tag{74}$$

$$P_{New\ Residual} = P_{residual} - P_{HESS} \tag{75}$$

Figure 4.15 below shows a 24-hour simulation for an RFB coupled to a PV plant, with an optimized charging and discharging schedule obtained from the Genetic Algorithm (GA). The graph also shows the unit cost of electricity for each hour of the day, which is based on a dynamic retail price by Pacific Gas and Electric Company (PG&E) [82].An optimized schedule is one that will reduce the total cost of electricity for the consumer, and in this case corresponds to times when there is a demand and electricity:

- The battery will discharge when there is a demand and electricity is at medium to high price ($0.21/kWh – $0.40 /kWh). This will reduce the amount of electricity that must be purchased from the grid at these higher prices.
- The battery will recharge when:
    - There is an excess in solar generation i.e. the residual PV power is positive
    - When electricity prices are in the low to medium range ($0.18 /kWh to $0.21/kWh).

During battery charging phase, there are three distinct time periods where the RFB is not utilizing the entire amount of excess solar production, resulting in curtailment of the surplus PV power. This occurs at the following periods:

- At time t = 10 hrs to t = 11 hrs:
    - The GA has determined that the optimum operation for the RFB is to recharge at 75 kW for this hour.
    - At this time, the minute-based solar generation fluctuates between 0kW up to 110 kW and the RFB can only recharge at the rate of the available solar

generation. Although the optimized battery charging schedule is 45 kW for the hour, if the minute-based solar generation falls below 45 kW (e.g., 5 kW), the battery can only charge at this amount.

- Because the optimum charging rate is 45 kW, any solar generation above this rate will not be used by the battery. Therefore, the battery follows the fluctuating solar profile between 0 to 45 kW and solar production between 45 to 110 kW will be curtailed.
- This scenario is a good example of where the SC could be used to reduce solar curtailment. When solar production > 45 kW, the SC could use excess power to recharge. When the PV generation < 45 kW, the SC could recharge the RFB to maintain the RFB's optimized charging rate.

- At time t = 11 hrs to t = 12 hrs:
  - The GA has determined that the optimum operation for the RFB is to recharge at 63 kW and the minute-based PV production fluctuates between 10 kW to 120 kW.
  - Due to technological limits of the RFB (i.e. the cell voltage must be kept below 1.5 V), it can only recharge at a maximum rate of 45 – 50 kW.
  - Therefore, the RFB will charge by following the PV generation profile, between 10 to 50 kW. Any solar production above 45 – 50 kW will be curtailed.
  - Similar to the previous hour, this is another situation where the SC could be used to reduce solar curtailment. When the rate of solar production is above the RFB's maximum charge rate (45 - 50 kW), the SC could use the excess solar power to recharge, and when it is below this limit, the SC could recharge the RFB.
- At time t = 12 hrs to t = 16 hrs:
  - The optimized charging schedule determined by the GA is 32 – 54 kW, however, the maximum RFB charge limits are lower than this range and correspond to 24 – 45 kW. Any solar production above the maximum charging limits will be curtailed.
  - Solar generation fluctuates between 50 to 100 kW, and it is always above the maximum RFB charging limits, therefore there will always be some solar curtailment for the entirety of the period.
  - A SC would not provide any benefit for this period. As per the point above, solar production constantly exceeds the RFB charging limit during this period, therefore the RFB is charging at its maximum possible rate. Additional power provided by the SC could not be accepted by the battery.

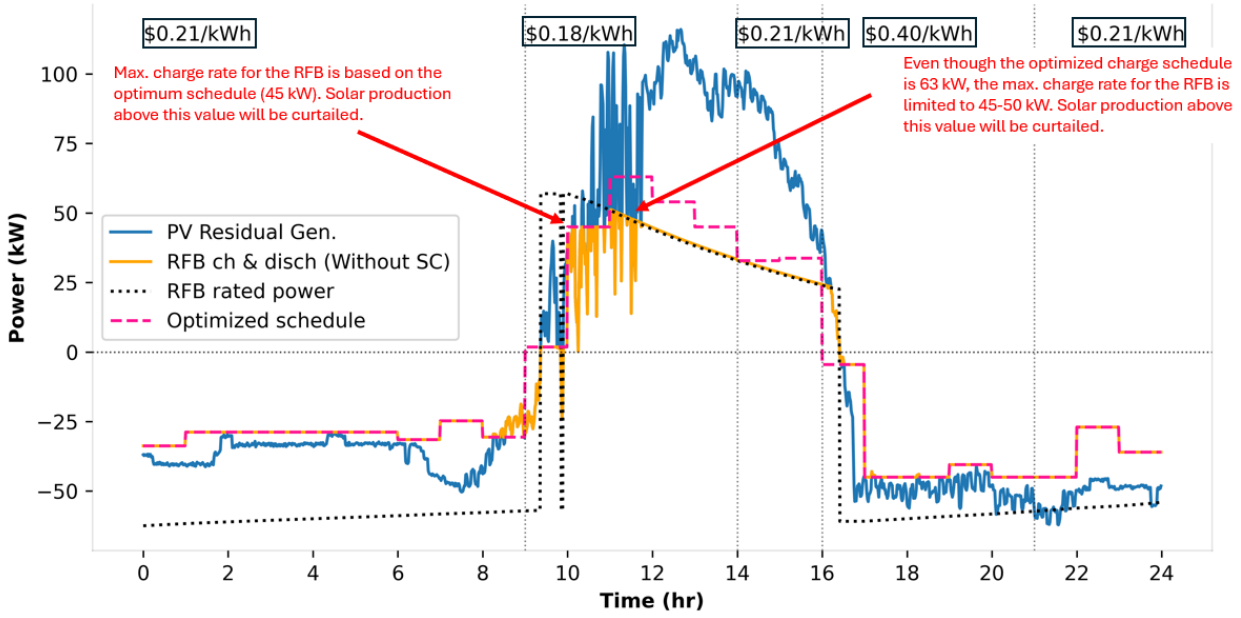

Figure 4.15. Example of a GA multi-period optimize 75 kW/ 375 kWh VRFB charging and discharging schedule, when coupled to a 140 kWp PV plant, with a temporal simulation resolution of 1 minute.

By incorporating a SC into the arrangement, the RFB charging is brought closer to the optimum target charging rate during hours 10 – 12 and solar curtailment can be reduced. The simulation results in Figure 4.16 show the 24-hour RFB charging profile when it is coupled with a SC, and is compared to the original RFB profile without a SC (as per Figure 4.15). Figure 4.17 shows a closer inspection of the results occurring in hour 10. It can be seen how the SC recharges when there is excess solar power not used by the battery, and then discharges to supply power to the RFB, when the RFB charges below the optimized target rate. There is a clear difference in RFB charging profiles with SC vs without SC and the advantage of using the SC is evident. Figure 4.18 and Figure 4.19 demonstrate similar results for the salt-based battery.

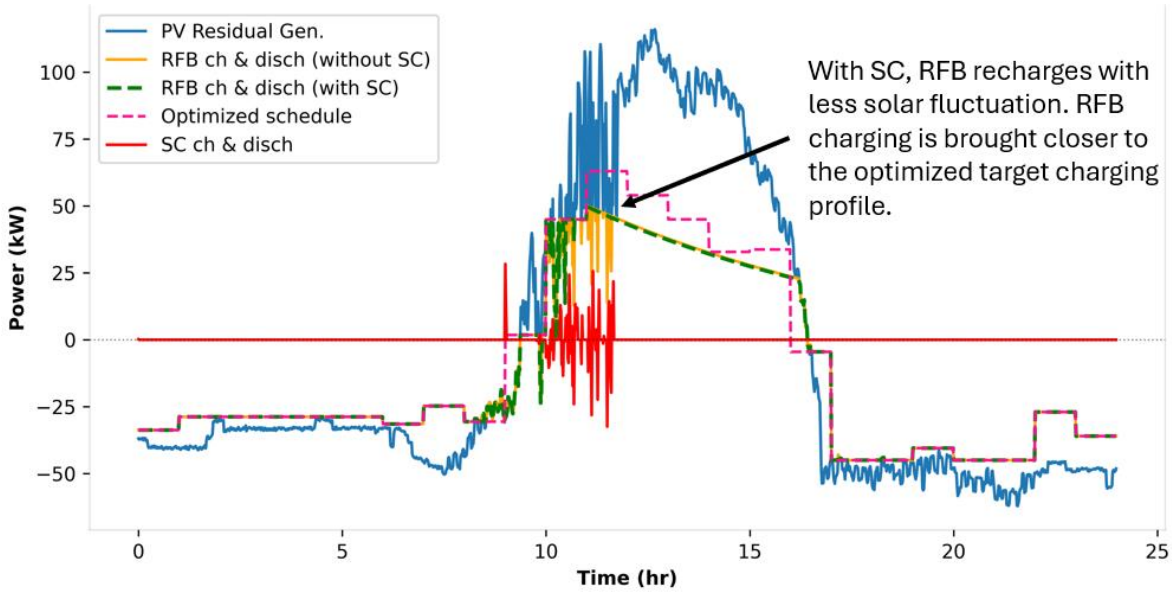

Figure 4.16 Example of a GA multi-period optimized 75 kW/ 375 kWh VRFB charging and discharging schedule, with a 1000 kW SC added to smooth out fluctuations from the available PV generation. The temporal resolution of the simulation was 1 minute.

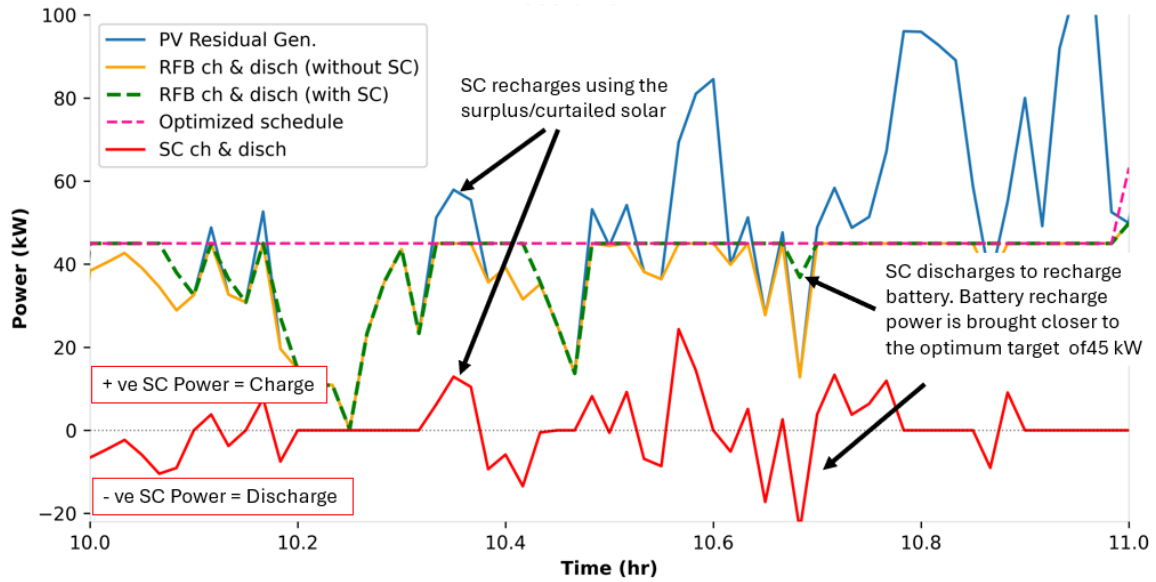

Figure 4.17 Closer inspection of the GA multi-period optimized 75 kW/ 375 kWh VRFB and 1000 kW SC charging and discharging schedule. The temporal resolution of the simulation was 1 minute.

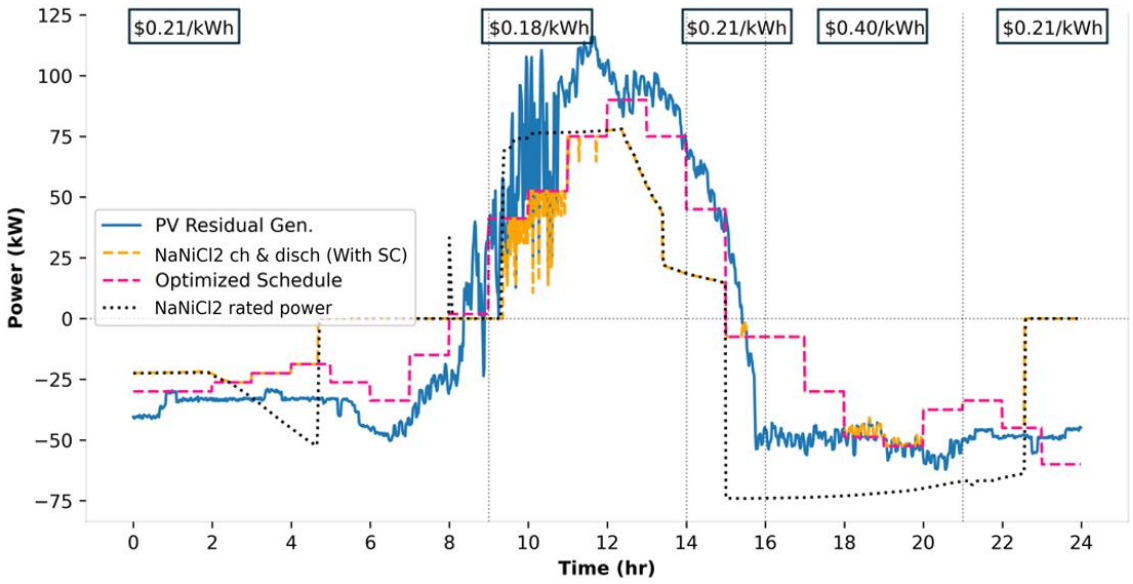

Figure 4.18 . Example of a GA multi-period optimized 75 kW/ 288 kW $NaNiCl_2$ battery charging and discharging schedule, when coupled to a 140 kWp PV plant. The temporal resolution of the simulation was 1 minute.

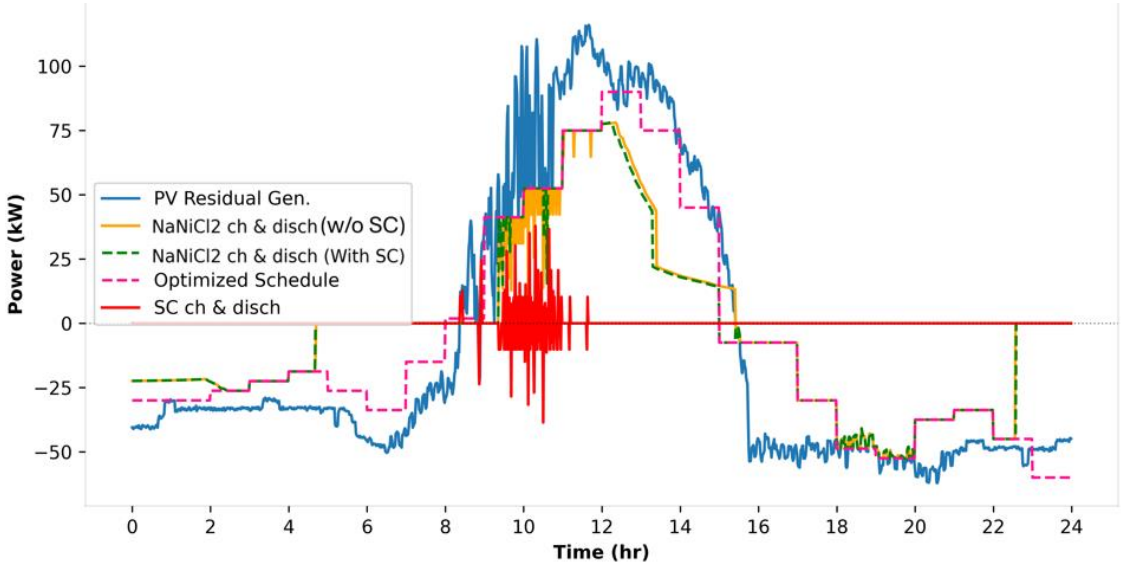

Figure 4.19 Example of a GA multi-period optimized optimized 75 kW/ 288 kW $NaNiCl_2$ battery charging and discharging schedule, with a 1000 kW SC added to smooth out fluctuations from the available PV generation. The temporal resolution of the simulation was 1 minute.

As mentioned, the power demand that cannot be met by the PV plant or the storage systems must be purchased from the grid. The total cost of electricity of purchased over the 9-day period is summarised in Table 4-4 below, for the following scenarios:

- No storage
- Battery only storage with RFB
- HESS storage with RFB and SC
- Battery only storage with the salt-based battery
- HESS storage with the salt-based battery and SC

By comparing the battery only scenarios with the no storage option, incorporating a battery in the arrangement will result in energy cost savings and the results indicate a cost reduction of 5.7 – 14.4%. The RFB gave greater cost reductions, however it is difficult to directly compare the two batteries this way considering they had different rated power and energy storage capacities. The RFB had greater storage capacity by ~87 kWh, which contributed to this cost savings difference. Furthermore, the salt-based battery would have used a significant portion of its stored energy and PV generated power for the heating requirements to maintain within its operating temperature. By incorporating a SC for both batteries, there is a cost reduction of 1.4 to 7.8%. The HESS with the salt-based battery has a greater cost savings when comparing with the respective battery only scenario; however, the total energy cost of $1523 is still greater than the cost savings between RFB only vs no storage.

Table 4-4 Summary of energy cost when using a battery only (RFB or $NaNiCl_2$) vs when using the HESS

	Arrangement	**RFB**	**$NaNiCl_2$**
Total Cost of Energy	No Storage	$1740	$1740
	Battery Only	$1490	$1641
	HESS (Battery + SC)	$1469	$1523
Rel. Difference	Battery only vs No Storage	-14.4%	-5.7%
	Battery only vs HESS	-1.4%	-7.8%
Abs. Difference	Battery only vs No Storage	-$250	-$99
	Battery only vs HESS	- $21	-$118

Discussion

In our techno-economic analysis of the HESS, we are acknowledged that SCs possess a high-power density, making them highly suitable for managing high-frequency power fluctuations occurring within fractions of a second. While SCs are typically employed for primary control due to their rapid response capabilities, this work explores their role not in primary system control but in contributing to economic performance and long-term planning, leveraging their complementary behaviour with batteries. Our analysis highlights the significant role of SCs in energy arbitrage, demonstrating their potential to be effectively utilized in such analyses,

which is a novel application. For the purposes of our long-term analysis, we focus on the use of SC within a minute-based timeframe. This approach assumes that minute-based fluctuations sufficiently capture the realities relevant to techno-economic assessments. While rapid spikes and fluctuations occurring within each minute may not be explicitly captured at this resolution, the minute-based analysis strikes a practical balance between capturing essential system dynamics and maintaining computational feasibility over extended periods. Moreover, the minute-based timeframe is well-suited to our objective, as the focus is not on real-time system control but on evaluating how the HESS can enhance overall performance and profitability. This resolution enables a comprehensive assessment of the benefits and operational strategies of integrating SC into the HESS.

The evaluation of both configurations demonstrates that the integration of SCs into HESS is beneficial for planning and management purposes. Specifically, we have shown that SCs provide additional flexibility in operation, allowing the HESS to adapt to various scenarios and demands. Our approach incorporates higher timeframes for battery management and lower timeframes for SC operations, ensuring that long-term energy storage and short-term power fluctuations are effectively handled. Furthermore, the integration of SCs offers significant techno-economic advantages, including increased profitability through better utilization of energy resources and improved system stability. The developed platform is a valuable tool for demo owners, providing insights into the potential profitability and stability improvements from using HESS under different scenarios. It also lays the groundwork for more detailed analyses in D2.3, focusing on the optimal sizing of HESS. In summary, the integration of SC with both aqueous-based RFBs and salt-based batteries enhances the performance, flexibility, and economic viability of HESS. By addressing the specific limitations of each battery type and improving system stability, SCs play a vital role in optimizing energy storage solutions within the SMHYLES project.

5. CONCLUSION AND FUTURE WORK

The development of Hybrid Energy Storage System (HESS) digital models in this deliverable (D2.2) represents a cornerstone achievement in the SMHYLES project, providing a comprehensive framework for optimizing the design, operation, and economic viability of advanced energy storage systems. By integrating complementary technologies such as Redox Flow Batteries, Salt-based Batteries, and Supercapacitors, these models showcase the versatility of HESSs in addressing diverse energy storage needs, ranging from rapid-response ancillary services to long-duration energy balancing. This work demonstrates the potential of HESSs to address critical challenges in modern energy systems, including managing grid variability, supporting renewable energy integration, enabling energy arbitrage, and increasing the self-consumption of renewable energy sources (RESs).

Each HESS component, Redox Flow Batteries, Salt-based Batteries, and Supercapacitors, has been separately modelled and validated with experimental data, highlighting the robustness and reliability of these models. They provide critical insights into the techno-economic performance and operational dynamics of HESS components across various scenarios. These models form the foundation for optimizing HESS design and operations, ensuring their applicability in industrial microgrids and grid services.

Additionally, a multi-objective, multi-period optimization platform has been developed within D2.2 to optimize the interaction between Aquas HESS (AHESS) and Salt HESS (SHESS), enabling long-term techno-economic assessments. This platform accounts for the fast response capabilities of supercapacitors and the slower response characteristics of batteries, showcasing its application in scenarios such as energy arbitrage. It also serves as a foundation for further studies under Task 2.3 in Deliverable D2.3, which will focus on optimizing the sizing of HESS components. These future studies will explore various scenarios and use cases introduced in D2.1, further enhancing the scalability and practicality of HESS solutions.

Moreover, the optimization platform will support innovative business cases, unlocking new revenue streams through services like energy arbitrage, demand response, and peak shaving. These efforts aim to enhance the scalability, practicality, and economic viability of HESS, establishing them as a key technology in the global transition toward decarbonization. By enabling resilient, flexible, and sustainable energy systems, HESSs contribute to meeting the growing demand for renewable energy integration and efficient energy management.

Future work will build upon these findings through detailed scenario analyses, evaluating HESS performance under diverse operational conditions, including varying configurations of HESSs, renewable energy penetration levels, and dynamic load profiles. These advancements will ensure the continued relevance of HESS models across industrial, commercial, and residential contexts, solidifying the SMHYLES project's contribution to advancing energy storage

technologies and addressing the urgent need for sustainable solutions in an evolving energy landscape.

REFERENCES

[1] J. I. Leon, E. Dominguez, L. Wu, A. Marquez Alcaide, M. Reyes, and J. Liu, "Hybrid Energy Storage Systems: Concepts, Advantages, and Applications," IEEE Industrial Electronics Magazine, vol. 15, no. 1, pp. 74–88, Mar. 2021, doi: 10.1109/MIE.2020.3016914.

[2] M. Arbabzadeh, R. Sioshansi, J. X. Johnson, and G. A. Keoleian, "The role of energy storage in deep decarbonization of electricity production," Nat Commun, vol. 10, no. 1, Dec. 2019, doi: 10.1038/s41467-019-11161-5.

[3] H. Liang, J. Su, and L. Deng, "A Digital Twin Technology-Based Optimization Method for Energy Storage Evaluation of New Energy Power Systems," in 2023 3rd International Conference on Energy Engineering and Power Systems, EEPS 2023, Institute of Electrical and Electronics Engineers Inc., 2023, pp. 395–399. doi: 10.1109/EEPS58791.2023.10256990.

[4] S. J. Lee and Y. Yoon, "Electricity cost optimization in energy storage systems by combining a genetic algorithm with dynamic programming," Mathematics, vol. 8, no. 9, Sep. 2020, doi: 10.3390/math8091526.

[5] European Association for Storage of Energy, "Energy Storage Applications Summary," Brussels, Jun. 2020.

[6] International Renewable Energy Agency, "Enabling technologies : innovation landscape," International Renewable Energy Agency, 2019.

[7] P. Denholm, W. Cole, and N. Blair, "Moving Beyond 4-Hour Li-Ion Batteries: Challenges and Opportunities for Long(er)-Duration Energy Storage," 2023. [Online]. Available: www.nrel.gov/publications.

[8] T. S. Babu, K. R. Vasudevan, V. K. Ramachandaramurthy, S. B. Sani, S. Chemud, and R. M. Lajim, "A Comprehensive Review of Hybrid Energy Storage Systems: Converter Topologies, Control Strategies and Future Prospects," IEEE Access, vol. 8, pp. 148702–148721, 2020, doi: 10.1109/ACCESS.2020.3015919.

[9] F. Tao, M. Zhang, Y. Liu, and A. Y. C. Nee, Digital Twin Driven Smart Manufacturing. Elsevier, 2019.

[10] T. H. J. Uhlemann, C. Schock, C. Lehmann, S. Freiberger, and R. Steinhilper, "The Digital Twin: Demonstrating the Potential of Real Time Data Acquisition in Production Systems," in Procedia Manufacturing, Elsevier B.V., Jan. 2017, pp. 113–120. doi: 10.1016/j.promfg.2017.04.043.

[11] S. K. Khaitan and J. D. McCalley, “Design techniques and applications of cyberphysical systems: A survey,” IEEE Syst J, vol. 9, no. 2, pp. 350–365, Jun. 2015, doi: 10.1109/JSYST.2014.2322503.

[12] Q. Qi, D. Zhao, T. W. Liao, and F. Tao, “Modeling of cyber-physical systems and digital twin based on edge computing, fog computing and cloud computing towards smart manufacturing,” in ASME 2018 13th International Manufacturing Science and Engineering Conference, MSEC 2018, American Society of Mechanical Engineers (ASME), 2018. doi: 10.1115/MSEC2018-6435.

[13] W. Yu, P. Patros, B. Young, E. Klinac, and T. Gordon Wamsley, “Energy digital twin technology for industrial energy management Classification, challenges and future,” Elsevier, vol. 161, 2022.

[14] S. Attaran, M. Attaran, and B. G. Celik, “Digital Twins and Industrial Internet of Things: Uncovering operational intelligence in industry 4.0,” Decision Analytics Journal, vol. 10, Mar. 2024, doi: 10.1016/j.dajour.2024.100398.

[15] M. Skyllas-Kazacos, M. H. Chakrabarti, S. A. Hajimolana, F. S. Mjalli, and M. Saleem, “Progress in Flow Battery Research and Development,” J Electrochem Soc, vol. 158, no. 8, p. R55, 2011, doi: 10.1149/1.3599565.

[16] A. Trovò, “Battery management system for industrial-scale vanadium redox flow batteries: Features and operation,” J Power Sources, vol. 465, Jul. 2020, doi: 10.1016/j.jpowsour.2020.228229.

[17] A. Trovò, F. Picano, and M. Guarnieri, “Comparison of energy losses in a 9 kW vanadium redox flow battery,” J Power Sources, vol. 440, Nov. 2019, doi: 10.1016/j.jpowsour.2019.227144.

[18] X. Xu et al., “Challenges and opportunities toward long-life lithium-ion batteries,” J Power Sources, vol. 603, May 2024, doi: 10.1016/j.jpowsour.2024.234445.

[19] A. Trovò and R. Turri, “Industrializing Vanadium Redox Flow Battery,” 2019.

[20] A. Trovò, G. Marini, W. Zamboni, and S. D. Sessa, “Redox Flow Batteries: A Glance at Safety and Regulation Issues,” Electronics (Switzerland), vol. 12, no. 8, Apr. 2023, doi: 10.3390/electronics12081844.

[21] MIT, The Future of Energy Storage An Interdisciplinary MIT Study.

[22] R. Di Rienzo, G. Simonte, I. Biagioni, F. Baronti, R. Roncella, and R. Saletti, “Experimental Investigation of an Electrical Model for Sodium-Nickel Chloride Batteries”, doi: 10.3390/en22050513.

[23] S. Bracco, F. Delfino, A. Trucco, and S. Zin, “Electrical storage systems based on Sodium/Nickel chloride batteries: A mathematical model for the cell electrical parameter evaluation validated on a real smart microgrid application,” J Power Sources, vol. 399, pp. 372–382, Sep. 2018, doi: 10.1016/j.jpowsour.2018.07.115.

[24] X. Lu, G. Xia, J. P. Lemmon, and Z. Yang, “Advanced materials for sodium-beta alumina batteries: Status, challenges and perspectives,” May 01, 2010. doi: 10.1016/j.jpowsour.2009.11.120.

[25] R. Benato et al., “Sodium nickel chloride battery technology for large-scale stationary storage in the high voltage network,” J Power Sources, vol. 293, pp. 127–136, Oct. 2015, doi: 10.1016/j.jpowsour.2015.05.037.

[26] E. C. Kluiters, D. Schmal, W. R. Ter Veen, and J. C. M. Posthumus, “Testing of a sodiumrnickel chloride ZEBRA battery for electric propulsion of ships and vehicles,” 1999.

[27] H. Bakhshi Yamchi, H. Shahsavari, N. Taghizadegan Kalantari, A. Safari, and M. Farrokhifar, “A cost-efficient application of different battery energy storage technologies in microgrids considering load uncertainty,” J Energy Storage, vol. 22, pp. 17–26, Apr. 2019, doi: 10.1016/j.est.2019.01.023.

[28] M. Aneke and M. Wang, “Energy storage technologies and real life applications – A state of the art review,” Oct. 01, 2016, Elsevier Ltd. doi: 10.1016/j.apenergy.2016.06.097.

[29] Sonick power, “Sonick power - Our Solution.”

[30] J. L. Sudworth, “The sodium/nickel chloride (ZEBRA) battery.”

[31] R. T. Yadlapalli, R. K. R. Alla, R. Kandipati, and A. Kotapati, “Super capacitors for energy storage: Progress, applications and challenges,” May 01, 2022, Elsevier Ltd. doi: 10.1016/j.est.2022.104194.

[32] E. Goikolea and R. Mysyk, “Emerging Nanotechnologies in Rechargeable Energy Storage Systems,” 2017. doi: 10.1016/B978-0-323-42977-1/00004-2.

[33] A. González, E. Goikolea, J. A. Barrena, and R. Mysyk, “Review on supercapacitors: Technologies and materials,” May 01, 2016, Elsevier Ltd. doi: 10.1016/j.rser.2015.12.249.

[34] A. Berrueta, A. Ursua, I. S. Martin, A. Eftekhari, and P. Sanchis, “Supercapacitors: Electrical Characteristics, Modeling, Applications, and Future Trends,” IEEE Access, vol. 7, pp. 50869–50896, 2019, doi: 10.1109/ACCESS.2019.2908558.

[35] K. E. Rodby, T. J. Carney, Y. Ashraf Gandomi, J. L. Barton, R. M. Darling, and F. R. Brushett, “Assessing the levelized cost of vanadium redox flow batteries with capacity fade and rebalancing,” J Power Sources, vol. 460, Jun. 2020, doi: 10.1016/j.jpowsour.2020.227958.

[36] M. S. Yesilyurt and H. A. Yavasoglu, “An All-Vanadium Redox Flow Battery: A Comprehensive Equivalent Circuit Model,” Energies (Basel), vol. 16, no. 4, Feb. 2023, doi: 10.3390/en16042040.

[37] C. Schubert et al., “Hybrid Energy Storage Systems Based on Redox-Flow Batteries: Recent Developments, Challenges, and Future Perspectives,” Apr. 01, 2023, Multidisciplinary Digital Publishing Institute (MDPI). doi: 10.3390/batteries9040211.

[38] A. I. Cahyadi, O. Wahyungoro, and R. Dewangga, “Comparison of Simple Battery Model and Thevenin Battery Model for SOC Estimation Based on OCV Method,” in 2019 International Conference on Information and Communications Technology (ICOIACT), 2019.

[39] M. R. Mohamed, H. Ahmad, M. N. A. Seman, S. Razali, and M. S. Najib, “Electrical circuit model of a vanadium redox flow battery using extended Kalman filter,” J Power Sources, vol. 239, pp. 284–293, 2013, doi: 10.1016/j.jpowsour.2013.03.127.

[40] T. Puleston, A. Clemente, R. Costa-Castelló, and M. Serra, “Modelling and Estimation of Vanadium Redox Flow Batteries: A Review,” Sep. 01, 2022, MDPI. doi: 10.3390/batteries8090121.

[41] S. Roe, C. Menictas, and M. Skyllas-Kazacos, “A High Energy Density Vanadium Redox Flow Battery with 3 M Vanadium Electrolyte,” J Electrochem Soc, vol. 163, no. 1, pp. A5023–A5028, 2016, doi: 10.1149/2.0041601jes.

[42] J. Noack, L. Wietschel, N. Roznyatovskaya, K. Pinkwart, and J. Tübke, “Techno-economic modeling and analysis of redox flow battery systems,” Energies (Basel), vol. 9, no. 8, 2016, doi: 10.3390/en9080627.

[43] M. Guarnieri, P. Mattavelli, G. Petrone, and G. Spagnuolo, “Vanadium redox flow batteries: Potentials and challenges of an emerging storage technology,” IEEE Industrial Electronics Magazine, vol. 10, no. 4, pp. 20–31, Dec. 2016, doi: 10.1109/MIE.2016.2611760.

[44] P. Leung, X. Li, C. Ponce De León, L. Berlouis, C. T. J. Low, and F. C. Walsh, “Progress in redox flow batteries, remaining challenges and their applications in energy storage,” RSC Adv, vol. 2, no. 27, pp. 10125–10156, Nov. 2012, doi: 10.1039/c2ra21342g.

[45] A. H. Fathima and K. Palanismay, “Modeling and operation of a Vanadium Redox Flow Battery for a PV,” in 1st International Conference on Power Engineering, Computing and COntrol, 2017.

[46] G. Merei, S. Adler, D. Magnor, M. Leuthold, and D. U. Sauer, “Multi-Physics Model for a Vanadium RFB,” Elsevier Science Direct, 2017.

[47] A. G. Olabi et al., “Redox Flow Batteries: Recent Development in Main Components, Emerging Technologies, Diagnostic Techniques, Large-Scale Applications, and Challenges and

Barriers," Aug. 01, 2023, Multidisciplinary Digital Publishing Institute (MDPI). doi: 10.3390/batteries9080409.

[48] X. Z. Yuan et al., "A review of all-vanadium redox flow battery durability: Degradation mechanisms and mitigation strategies," Oct. 25, 2019, John Wiley and Sons Ltd. doi: 10.1002/er.4607.

[49] C. Ding, H. Zhang, X. Li, T. Liu, and F. Xing, "Vanadium flow battery for energy storage: Prospects and challenges," Apr. 18, 2013. doi: 10.1021/jz4001032.

[50] I. Derr, M. Bruns, J. Langner, A. Fetyan, J. Melke, and C. Roth, "Degradation of all-vanadium redox flow batteries (VRFB) investigated by electrochemical impedance and X-ray photoelectron spectroscopy: Part 2 electrochemical degradation," J Power Sources, vol. 325, pp. 351–359, Sep. 2016, doi: 10.1016/j.jpowsour.2016.06.040.

[51] K. J. Kim, M. S. Park, Y. J. Kim, J. H. Kim, S. X. Dou, and M. Skyllas-Kazacos, "A technology review of electrodes and reaction mechanisms in vanadium redox flow batteries," J Mater Chem A Mater, vol. 3, no. 33, pp. 16913–16933, Jun. 2015, doi: 10.1039/c5ta02613j.

[52] P. Alotto, M. Guarnieri, and F. Moro, "Redox flow batteries for the storage of renewable energy: A review," 2014, Elsevier Ltd. doi: 10.1016/j.rser.2013.08.001.

[53] I. Derr et al., "Electroless chemical aging of carbon felt electrodes for the all-vanadium redox flow battery (VRFB) investigated by Electrochemical Impedance and X-ray Photoelectron Spectroscopy," Electrochim Acta, vol. 246, pp. 783–793, Aug. 2017, doi: 10.1016/j.electacta.2017.06.050.

[54] T. Sukkar and M. Skyllas-Kazacos, "Membrane stability studies for vanadium redox cell applications," 2003.

[55] Energy Storage Solutions, "Vanadium Redox Flow Battery 250KW (1,000KWh) by E22 Energy Storage Solutions."

[56] N. Shamim, E. C. Thomsen, V. V. Viswanathan, D. M. Reed, V. L. Sprenkle, and G. Li, "Evaluating zebra battery module under the peak-shaving duty cycles," Materials, vol. 14, no. 9, 2021, doi: 10.3390/ma14092280.

[57] S. Dambone Sessa, G. Crugnola, M. Todeschini, S. Zin, and R. Benato, "Sodium nickel chloride battery steady-state regime model for stationary electrical energy storage," J Energy Storage, vol. 6, pp. 105–115, May 2016, doi: 10.1016/j.est.2016.03.005.

[58] M. Vona, "ESS Presentaton ST253 FIAMM ESS/ FIAMM Group," 2015, FIAMM.

[59] R. Christin, "Multiphysics modeling of sodium nickel chloride cells," HALOpenScience, 2015. [Online]. Available: https://theses.hal.science/tel-01916189

[60] N. Büttner et al., "Electrochemical Modelling of Na-MCl2 Battery Cells Based on an Expanded Approximation Method," Batteries, vol. 9, no. 4, Apr. 2023, doi: 10.3390/batteries9040200.

[61] G. T. Nguyen, H. S. Hwang, J. Lee, D. A. Cha, and I. Park, "N‐octadecane/fumed silica phase change composite as building envelope for high energy efficiency," Nanomaterials, vol. 11, no. 3, pp. 1–15, Mar. 2021, doi: 10.3390/nano11030566.

[62] FZSonick, "POWERED by SALT - Sodium Metal Chloride Battery System Technical Overview."

[63] C. H. Dustmann, "Advances in ZEBRA batteries," J Power Sources, vol. 127, no. 1–2, pp. 85–92, Mar. 2004, doi: 10.1016/J.JPOWSOUR.2003.09.039.

[64] S. Sharma and P. Chand, "Supercapacitor and electrochemical techniques: A brief review," Jan. 01, 2023, Elsevier B.V. doi: 10.1016/j.rechem.2023.100885.

[65] M. Ceraolo, G. Lutzemberger, and D. Poli, "State-Of-Charge evaluation of supercapacitors."

[66] E. Pameté et al., "The Many Deaths of Supercapacitors: Degradation, Aging, and Performance Fading," Aug. 04, 2023, John Wiley and Sons Inc. doi: 10.1002/aenm.202301008.

[67] T. Zhou and W. Sun, "Optimization of battery-supercapacitor hybrid energy storage station in Wind/solar generation system," IEEE Trans Sustain Energy, vol. 5, no. 2, pp. 408–415, Apr. 2014, doi: 10.1109/TSTE.2013.2288804.

[68] A. Castillejo-Cuberos, J. M. Cardemil, and R. Escobar, "Techno-economic assessment of photovoltaic plants considering high temporal resolution and non-linear dynamics of battery storage," Appl Energy, vol. 334, Mar. 2023, doi: 10.1016/j.apenergy.2023.120712.

[69] J. c. Henandez, F. Gomez-Gonzalez, F. Sanchez-Suitl, and F. Jurado, "Optimization of battery/supercapacitor based photovoltaic household-prosumers providing self-consumption and frequency containment reserve as influenced by temporal data granularity," Elseiver, 2021.

[70] C. Xu et al., "Economic Analysis of Li-Ion Battery–Supercapacitor Hybrid Energy Storage System Considering Multitype Frequency Response Benefits in Power Systems," Energies (Basel), vol. 16, no. 18, Sep. 2023, doi: 10.3390/en16186621.

[71] M. E. Şahin, F. Blaabjerg, and A. Sangwongwanich, "A Comprehensive Review on Supercapacitor Applications and Developments," Feb. 01, 2022, MDPI. doi: 10.3390/en15030674.

[72] W. Jing, C. H. Lai, W. S. H. Wong, and M. L. D. Wong, "A comprehensive study of battery-supercapacitor hybrid energy storage system for standalone PV power system in rural electrification," Appl Energy, vol. 224, pp. 340–356, Aug. 2018, doi: 10.1016/j.apenergy.2018.04.106.

[73] J. Zhang, M. Gu, and X. Chen, "Supercapacitors for renewable energy applications: A review," Micro and Nano Engineering, vol. 21, Dec. 2023, doi: 10.1016/j.mne.2023.100229.

[74] S. Korjani, M. Mureddu, A. Facchini, and A. Damiano, "Aging cost optimization for planning and management of energy storage systems," Energies (Basel), vol. 10, no. 11, Nov. 2017, doi: 10.3390/en10111916.

[75] S. Korjani, A. Facchini, M. Mureddu, A. Rubino, and A. Damiano, "Battery management for energy communities—Economic evaluation of an artificial intelligence-led system," J Clean Prod, vol. 314, Sep. 2021, doi: 10.1016/j.jclepro.2021.128017.

[76] S. Korjani, A. Serpi, and A. Damiano, "A Genetic Algorithm Approach for Sizing Integrated PV-BESS Systems for Prosumers."

[77] M. Buchajczyk, S. Korjani, M. Duranti, and E. Macchi, Techno-Economic Analysis and Sizing of RFB and Supercapacitor-Based HESS for an EV Charging Station. 2024. doi: 10.23919/AEIT63317.2024.10736734.

[78] M. H. Rasool, O. Taylan, U. Perwez, and C. Batunlu, "Comparative assessment of multi-objective optimization of hybrid energy storage system considering grid balancing," Renew Energy, vol. 216, Nov. 2023, doi: 10.1016/j.renene.2023.119107.

[79] L. Barelli, G. Bidini, D. A. Ciupageanu, A. Micangeli, P. A. Ottaviano, and D. Pelosi, "Real time power management strategy for hybrid energy storage systems coupled with variable energy sources in power smoothing applications," Energy Reports, vol. 7, pp. 2872–2882, Nov. 2021, doi: 10.1016/j.egyr.2021.05.018.

[80] https://www.egauge.net/eguard/, "eGuard Systems."

[81] X. Zhang, C. (Chris) Qin, E. Loth, Y. Xu, X. Zhou, and H. Chen, "Arbitrage analysis for different energy storage technologies and strategies," Energy Reports, vol. 7, pp. 8198–8206, Nov. 2021, doi: 10.1016/j.egyr.2021.09.009.

[82] PG & E Tariffs, "https://www.pge.com/tariffs/assets/."

Disclaimer:

Co-Funded by the European Union. Views and opinions expressed are however those of the author(s) only and do not necessarily reflect those of the European Union nor CINEA. Neither the European Union nor the granting authority can be held responsible for them.

SMHYLES
SAFE, SUSTAINABLE AND MODULAR HYBRID SYSTEMS FOR LONG-DURATION ENERGY STORAGE AND GRID SERVICES

COORDINATION
Edoardo Gino Macchi
Head of Battery and Electrification Technologies Unit – BET
Centre for Sustainable Energy – SE
Fondazione Bruno Kessler - FBK
Phone: +39 0461 314 887
E-mail: emacchi@fbk.eu